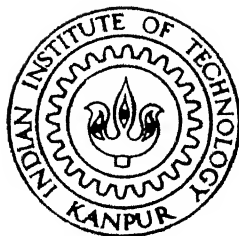


77 10 60

Modelled ✓

# MODELLING OF TRANSPORT PHENOMENA IN STEELMAKING

by  
**CHAITANYA BHANU**



ME  
97  
A  
HA  
MOD

Department of Materials and Metallurgical Engineering

**INDIAN INSTITUTE OF TECHNOLOGY KANPUR**

January, 1997

# MODELLING OF TRANSPORT PHENOMENA IN STEELMAKING

*A thesis Submitted*  
*in Partial Fulfilment of the Requirements*  
*for the Degree of*  
**MASTER OF TECHNOLOGY**

*by*  
**CHAITANYA BHANU**

*to the*  
**DEPARTMENT OF MATERIALS AND METALLURGICAL ENGINEERING**  
**INDIAN INSTITUTE OF TECHNOLOGY, KANPUR**  
JANUARY, 1997

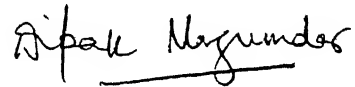
10 MAR 1997  
CENTRAL LIBRARY  
I. I. T., KANPUR  
Inv. No. A.123191

MME-1997-M-BHA-MOD

## CERTIFICATE

This is to certify that the present work ' *MODELLING OF TRANSPORT PHENOMENA IN STEELMAKING* ' has been carried out by Mr. Chaitanya Bhanu under my supervision and that this has not been submitted elsewhere for a degree.

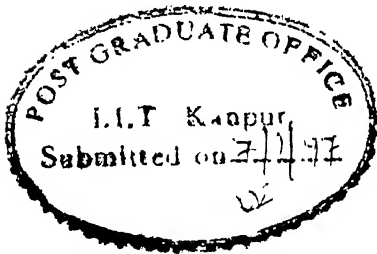
January 1997



( Prof. Dipak Mazumdar)

Department of Materials and Metallurgical Engineering

Indian Institute of Technology, Kanpur.



**Dr. Dipak Mazumdar**  
**Professor**  
**Department of Materials**  
**& Metallurgical Engineering**  
**I.I.T. Kanpur-208 016**



## **ACKNOWLEDGEMENT**

The author wishes to express his sincere appreciation and gratitude to Professor Dipak Mazumdar for his able guidance, valuable suggestions and remarkable patience during the course of this study.

The author would also like to thank his employer Tata Steel, Jamshedpur for providing study leave, for his period of stay at I.I.T., Kanpur. The financial support received from R.D.C.I.S., Ranchi is gratefully acknowledged.

The author sincerely acknowledges the help of Mr. A.K.Saha, Ph.D. scholar in the Mechanical Engineering Department with the graphics work. He would also like to thank his friends and well wishers, for making his stay at Kanpur a memorable one.

Finally, he would like to thank his parents for their unstinting support and encouragement.

# LIST OF CONTENTS

<b>Abstract</b>	i.
<b>List of Symbols</b>	iii.
<b>List of Figures</b>	vii.
<b>List of Tables</b>	x.

Page No.

## CHAPTER-1

<b>Introduction</b>	<b>1</b>
1.1 Introduction to the Thesis	1
1.2 Scope of the Present Work	4
1.3 Layout of the Thesis	6

## CHAPTER-2

<b>Modelling of Melting Rates in Axisymmetrical Gas Stirred Systems</b>	<b>7</b>
2.1 Introduction	7
2.2 Previous work on Melting of Solids in Gas Stirred Baths	8
2.3 Mathematical Modelling of Fluid Flow in Axi-Symmetric Gas Injection systems	11
2.3.1 Modelling assumptions	
2.4 Description of Steady State, Two Phase, Two Dimensional Turbulent Flow Model	12
2.4.1 The liquid phase flow equations	
2.4.2 The liquid phase turbulence model	
2.4.3 Equation of motion of the gas phase	
2.4.4 Estimation of the gas voidages	
2.4.5 Estimation of turbulence production due to bubbles and interphase friction forces	

2.4.6 The boundary conditions	
2.4.7 The numerical solution procedure	
<b>2.5 The Heat Transfer Model</b>	<b>21</b>
<b>2.6 Results and Discussion</b>	<b>21</b>
<b>2.7 An alternative Macroscopic Formulation</b>	<b>30</b>

## **CHAPTER-3**

<b>Development of A Steady State, Three Dimensional Turbulent Flow Calculation Procedure</b>	<b>38</b>
<b>3.1 Introduction</b>	<b>38</b>
<b>3.2 Governing Equations</b>	<b>39</b>
3.2.1 The liquid phase flow equations	
3.2.2 The turbulence model	
3.2.3 The boundary conditions	
<b>3.3 The General Differential Equation</b>	<b>46</b>
<b>3.4 The Grid Arrangement</b>	<b>47</b>
<b>3.5 The Numerical Solution Procedure</b>	<b>47</b>
3.5.1 Numerical Solution	
3.5.2 The Computer Program	
<b>3.6 Results and Discussion</b>	<b>54</b>
3.6.1 Laminar flow in an enclosed cubic cavity	
3.6.2 Entrance length prediction for laminar flow	
3.6.3 Turbulent flow in an enclosed cubic cavity	

## **CHAPTER-4**

<b>Modelling of Flow Phenomena in Rectangular Shaped Tundishes</b>	<b>71</b>
<b>4.1 Introduction</b>	<b>71</b>
<b>4.2 Characteristics of Metallurgical Tundish System</b>	<b>73</b>
<b>4.3 Mathematical Modelling of Tundish Hydrodynamics</b>	<b>75</b>
4.3.1 Modelling assumptions	
4.3.2 Governing equations and boundary conditions	

4.3.3 Governing equation of tracer dispersion	
4.4 Results and Discussion	80
4.4.1 Fluid flow behaviour	
4.4.2 Residence time distribution characteristics	
 <b>CHAPTER-5</b>	
<b>Concluding Remarks</b>	<b>95</b>
 <b>CHAPTER-6</b>	
<b>Recommendations for Future Work</b>	<b>96</b>
 <b>References</b>	<b>97</b>

## ABSTRACT

Name of Student : Chaitanya Bhanu

Roll No.: 9510603


Degree for which submitted : M.Tech.

Dept. : MME

Name of the thesis supervisor

1. Dr. Dipak Mazumdar , Professor.

Month and year of submission Jan 1997

Text of Abstract begins here 

Mathematical modelling has emerged as a key process analysis tool in the area of Metals and Materials processing operations. Considerable advances have been made through mathematical modelling in terms of improved process efficiency and better product quality. Most of the models applied have been mechanistic in nature and are based on the conservation of heat, mass and momentum. Transport of heat mass and momentum in metal processing operations are characteristically multidimensional ( most often three dimensional ) and multi-phase ( slag, metal and gas ) in nature. Consequently, for effective simulation, three dimensional transport models (steady or transient) are required . The present work primarily concerns with the development of a steady state, two phase, three dimensional, turbulent flow calculation procedure from an existing two phase, two dimensional turbulent flow model.

Thus, as a first step, the adequacy of an existing two dimensional turbulent flow model has been examined. This has been done by investigating melting phenomena in axisymmetrical gas stirred vessels for both aqueous and high temperature systems. Two dimensional predictions have been assessed against experimental measurements reported in literature and excellent agreement between the two demonstrated. Subsequent to this, the two dimensional calculation procedure has been upgraded to a steady, three dimensional configuration using the control volume based finite difference technique. The results from the three dimensional model were evaluated against standard benchmark solutions ( e.g., flow in a cubic cavity, entrance length against Reynolds number in ducts etc.) and physically realistic solutions were obtained for a wide range of conditions that are consistent with the observations reported in the literature.

Finally, the three dimensional turbulent flow model was used to predict the flow behaviour and *RTD* (residence time distribution) in a simple rectangular shaped tundish with no flow control devices. Predicted flows and *RTD* were qualitatively assessed against predictions reported in the literature and it was concluded that present model is capable of realistically simulating the hydro-dynamics of metallurgical tundish systems.

## LIST OF SYMBOLS

$A_P, A_E, A_W, A_N, A_S, A_T, A_B$	: coefficients of discretization equation representing the effect of convection and diffusion
$A_{nb}$	: summation of all neighbour point coefficients
$C, C_i$	: concentration of the tracer, $kg\ m^{-3}$
$C_o$	: average concentration of the tracer, $kg\ m^{-3}$
$C_1, C_2, C_\mu, \sigma_k, \sigma_\epsilon$	: constants of the k- $\epsilon$ model
$C_b$	: constant defined by Eq.(2.22)
$C_D$	: drag coefficient
$d_b$	: bubble diameter, $m$
$E$	: roughness parameter
$E_0$	: Eotvos number ( $= g\ \rho_l\ d_b^2 / \sigma$ )
$F_x, F_y, F_z, F_r$	: interphase drag forces in the Navier Stokes equations
$g$	: acceleration due to gravity, $m\ s^{-2}$
$G_k$	: volumetric rate of turbulence generation
$h$	: heat transfer coefficient, $kg\ s^{-3}\ K^{-1}$
$K$	: constant of proportionality
$k$	: turbulent kinetic energy, $m^2s^{-2}$
$L$	: depth of the liquid in the vessel, $m$
$N$	: number of bubbles in a train in a given control volume
$Nu$	: Nusselt number

$p$	: dynamic pressure with respect to the local hydro-static pressure, $Pa$
$Pe$	: Peclet number
$P_b$	: volumetric rate of turbulence generation due to bubbles
$Pr$	: Prandl number
$q$	: heat flux to the solid surface, $kg\ m^2\ s^{-3}$
$Q$	: gas flow rate corrected to mean height and pressure of the liquid, $m^3\ s^{-1}$
$r$	: radius of the bubble plume, $m$
$R$	: radius of the vessel, $m$
$Re$	: Reynolds number
$S$	: the source term in the discretization equation
$S_p$	: the slope of the linearized source term
$S_c$	: constant part of the linearized source term
$S_u$	: source term in the equation of motion in $x$ direction
$S_v$	: source term in the equation of motion in $y$ direction
$S_w$	: source term in the equation of motion in $z$ direction
$t$	: time, $s$
$t_{avg}$	: average residence time, $s$
$t_{min}$	: minimum breakthrough time, $s$
$t_{peak}$	: peak concentration time, $s$
$t_r$	: nominal residence time, $s$
$t_{r, m}$	: residence time of $m$ th bubble, $s$
$T_b$	: temperature of the bulk liquid, $^{\circ}K$



$T_m$	: temperature of the liquid at the sphere surface, $^{\circ}K$
$Tu$	: intensity of turbulence
$u$	: $x$ / axial component of velocity, $m s^{-1}$
$U$	: instantaneous liquid velocity component in axial direction, $m s^{-1}$
$U_b$	: resultant bubble velocity, $m s^{-1}$
$U_f$	: resultant instantaneous liquid velocity, $m s^{-1}$
$U_r$	: relative velocity vector, $m s^{-1}$
$u_{\tau}$	: friction velocity, $m s^{-1}$
$v$	: $y$ / radial component of velocity, $m s^{-1}$
$V$	: radial component of instantaneous liquid velocity, $m s^{-1}$
$V_{B,z}$	: instantaneous bubble velocity in the axial direction, $m s^{-1}$
$V_{B,r}$	: instantaneous bubble velocity in the radial direction, $m s^{-1}$
$V_d$	: dead volume, $m^3$
$V_{dp}$	: dispersed plug volume, $m^3$
$V_m$	: well mixed volume, $m^3$
$w$	: $z$ component of velocity, $m s^{-1}$
$W_B$	: work per unit time due to buoyancy, $kg m^2 s^{-3}$
$W_g$	: kinetic energy per unit time of injected gas at orifice of vessel, $kg m^2 s^{-3}$
$y^+$	: dimensionless distance normal to the wall
$\Delta H$	: latent heat of fusion, $kg m^2 s^{-2}$

$\Delta t$	: incremental time step in the trajectory, $s$
$\Delta V_{cv}$	: volume of the control volume, $m^3$
$\Delta X, \Delta Y, \Delta Z$	: length of control volume faces in three mutually perpendicular directions, $m$
$\delta X_e, \delta X_w, \delta Y_n, \delta Y_s, \delta Z_t, \delta Z_b$	: distance between the various nodes in the three mutually perpendicular coordinate axis, $m$
$\alpha_g$	: gas volume fraction
$\alpha_l$	: liquid volume fraction
$\rho_g$	: density of gas, $kg\ m^{-3}$
$\rho_l$	: density of liquid, $kg\ m^{-3}$
$\rho_s$	: density of the solid, $kg\ m^{-3}$
$\mu_l, \mu_0$	: liquid / bulk medium viscosity, $kg\ m^{-1}s^{-1}$
$\mu_T$	: turbulent viscosity, $kg\ m^{-1}s^{-1}$
$\mu_e$	: effective viscosity, $kg\ m^{-1}s^{-1}$
$\epsilon$	: rate of turbulence kinetic energy dissipation, $m^2s^{-3}$
$\phi$	: general dependent variable of the discretization equation
$\phi_P, \phi_E, \phi_W, \phi_N, \phi_S, \phi_T, \phi_B$	: values of $\phi$ at the various nodes in the general discretization equation
$\phi_{nb}$	: summation of neighbour point $\phi'$ s
$\kappa$	: van Karmen constant
$\tau_w$	: shear stress close to the wall, $kg\ m^{-1}s^{-2}$
$\Gamma$	: diffusion coefficient, $kg\ m^{-1}s^{-1}$

## LIST OF FIGURES

- Fig.(1.1)* : The general methodology of mathematical model development [2].
- Fig.(2.1)* : Schematic of experimental setup of Taniguchi and co-workers [14,15].
- Fig.(2.2)* : Schematic of a section of Eulerian grid network intercepted by a bubble trajectory.
- Fig.(2.3)* : Schematic of the vessel geometry and the corresponding boundary conditions applied towards numerical simulation of axi-symmetric gas stirred ladle system.
- Fig.(2.4)* : Flow diagram of the two dimensional, two phase turbulent flow model [18].
- Fig.(2.5)* : A log-log plot between the experimental Nusselt number [14,15],  $(Nu-2)/\{Pr^{0.4} (\mu_b / \mu_o)^{0.25}\}$  and the present estimates of the Reynolds number,  $Re_D$ , vis a vis the line for Eq.(2.24). (Deduced through numerical simulation ).
- Fig.(2.6)* : Sensitivity of the predicted vertical velocity component to the diameter of monosize bubbles ( $d_b$ ) assumed to be forming at the lance tuyure tip.
- Fig.(2.7)* : Sensitivity of the predicted vertical velocity component to the value of drag coefficient ( $C_D$ ).
- Fig.(2.8)* : Sensitivity of the predicted vertical velocity component to the value of coefficient of turbulence generation by bubbles ( $C_b$ ).
- Fig.(2.9)* : A log-log plot between the experimental Nusselt number [14,15],  $(Nu-2)/\{Pr^{0.4} (\mu_b / \mu_o)^{0.25}\}$  and the present estimates of the Reynolds number,  $Re_D$ , vis a vis the line for Eq.(2.24). ( deduced through the macroscopic modelling Eq.(2.28).
- Fig.(2.10)* : A log-log plot between the experimental Nusselt number [14,15],  $(Nu-2)/ Pr^{0.33}$  and the present estimates of the Reynolds number,  $Re_D$ , vis a vis the line for Eq.(2.30).( deduced through the macroscopic modelling Eq.(2.28).

- Fig.(3.1)* : Schematic representation of procedure for the near wall treatment of flow variable and turbulence parameter in the turbulent flow model.
- Fig.(3.2)* : A typical three dimensional, scalar control volume and various nomenclature used in the cartesian co-ordinate system.
- Fig.(3.3)* : Scalar and staggered control volumes in three dimensional cartesian co-ordinate system.
- Fig.(3.4)* : Flow chart for the three dimensional, turbulent flow calculation procedure.
- Fig.(3.5.a)* : Schematic of the cubic cavity with one of the walls moving.( *Problem-1*)
- Fig.(3.5.b)* : Schematic of the cubic cavity with two parallel walls moving.( *Problem-2*)
- Fig.(3.6)* : The predicted flow pattern in the central  $XY$  plane (at  $z=0.25\ m$ ) with one of the cavity walls moving.( *Problem-1*)
- Fig.(3.7.a)* : The predicted flow pattern in the central  $XY$  plane (at  $z=0.25\ m$ ) with two parallel cavity walls moving.( *Problem-2*)
- Fig.(3.7.b)* : The predicted flow pattern in the  $XY$  plane (at  $z=0.05\ m$ ) with two parallel cavity walls moving. ( *Problem-2*)
- Fig.(3.7.c)* : The predicted flow pattern in the  $XY$  plane (at  $z=0.45\ m$ ) with two parallel cavity walls moving. ( *Problem-2*)
- Fig.(3.8.a)* : Schematic of the developing velocity profiles and pressure changes in the entrance of a duct flow.
- Fig.(3.8.b)* : Schematic of a duct with a square cross-section and the relevant co-ordinate axis to the problem.
- Fig.(3.9)* : The procedure adopted for modelling the inflow and outflow boundary condition for the prediction of entrance lengths.
- Fig.(3.10)* : Predicted entrance lengths (  $L_e / D$  ) as a function of the inlet Reynolds number.
- Fig.(3.11)* : Predicted variation of horizontal velocity,  $u$  along the vertical central axis (  $x=z=0.25\ m$  )of cubic cavity, for a region close to the moving wall for laminar and turbulent flows. ( *Problem-1*)
- Fig.(3.12)* : Velocity profiles in laminar and turbulent flows near a stationary wall [35].(bulk liquid moving with a velocity of  $1\ m/s$ )

*Fig.(4.1)* : Schematic representation of the continuous casting process.

*Fig.(4.2)* : Schematic of the single strand model tundish [17] simulated in the present study.

*Fig.(4.3.a)* : The predicted flow pattern in the central vertical  $XY$  plane (at  $z = 0.15\text{ m}$ ).

*Fig.(4.3.b)* : The predicted flow pattern in a vertical  $XY$  plane close to the wall ( at  $z = 0.03\text{ m}$  ).

*Fig.(4.4.a)* : The predicted flow pattern in a horizontal  $XZ$  plane close to the base of the tundish (at  $y = 0.012\text{ m}$ ).

*Fig.(4.4.b)* : The predicted flow pattern in a horizontal  $XZ$  plane (at  $y = 0.11\text{ m}$ ).

*Fig.(4.4.c)* : The predicted flow pattern in a horizontal  $XZ$  plane close to the free surface. (at  $y = 0.24\text{ m}$ ).

*Fig.(4.5)* : Predicted flow field in longitudinal, vertical planes with no flow control devices in a tundish with inclined wall [39].

*Fig.(4.6)* : Predicted  $RTD$  curves for monitoring location at  $1\text{ mm}$  and  $3\text{ mm}$  above the nozzle exit.

*Fig.(4.7.a)* : Sensitivity of the  $RTD$  curves to the step height,  $\Delta t$  assumed in the numerical procedure.

*Fig.(4.7.b)* : The affect of numerical value of effective viscosity on the prediction of  $RTD$  characteristics in the tundish system.

## LIST OF TABLES

*Table-2.1* : Values of the constant used in the  $k-\epsilon$  model of turbulence.

*Table-2.3* : Characteristic of the experimental conditions used by Taniguchi et.al. [14,15] and the present estimates of the liquid rise velocity and object Reynolds number in aqueous and high temperature systems.

*Table-2.3* : Sensitivity of the predicted axial velocity to the various grid configurations applied.

*Table-2.4* : Variations in the estimates of Nusselt number as a function of the bubble diameter ( $d_b$ ), drag coefficient ( $C_D$ ) and coefficient of turbulence generation ( $C_b$ ).

*Table-3.1* : Popularly used software packages to study transport phenomena [2].

*Table-3.2* : Definition of  $I$ ,  $\phi$  and  $S$  of Eq.(3.14).

*Table-4.1* : Characteristic parameters of the single strand model tundish [17].

*Table-4.2* : Comparative results of RTD characteristics obtained via physical modelling [17] and mathematical modelling.

# CHAPTER - 1

## INTRODUCTION

### 1.1 Introduction to the Thesis

Modelling has played a key role in developing a holistic approach towards the understanding of metals and materials processing operations. Most of the metallurgical processes are characterised by high temperature, opacity of melts and large reactor size. These as a consequence, make the industrial scale metal processing units less than convenient case studies. Consequently, it has been customary to investigate the process dynamics of steelmaking with the aid of physical and mathematical models.

Traditionally, physical modelling was the preferred tool [1] in metallurgy but of late, mathematical modelling has become more popular because of availability of several software packages, cheaper computational hardware, growing experience with the tackling of a broad range of computational problems and better understanding of the underlying fundamental concepts. With the development of new materials i.e., ceramics, composites etc. and a more challenging marketplace, the focus of a process metallurgist has undergone substantial reorientation and has shifted to cost control and better product quality. These warrant better process control and process optimisation. Towards this, mathematical modelling, over the last few years has played a key role, as both process control and process optimisation require the representation and understanding of the process / operation in quantitative form.

Apart from lower costs, mathematical modelling has other inherent advantages over conventional forms of investigation viz. pilot plant scale experimentation and physical modelling. They are as follows:

- i. *Speed* : With the help of a mathematical model a investigator can study various configurations with ease, at a remarkable speed .
- ii. *Information*: The data derived from mathematical model is detailed and complete. The values of all possible variables in the domain of interest can be calculated and this information can be put to much more effective use. Mathematical modelling scores over other forms of investigation viz. physical modelling and pilot scale experimentation on this aspect.
- iii. *Simulation flexibility*: With the help of a mathematical model, small scale or cold models can be studied. Further, various theoretical possibilities such as, constant density and infinite reaction rate options can also be evaluated which at times help the researcher in developing a better understanding of the subject.

The general methodology of a mathematical model development is shown schematically [2] in *Fig.(1.1)*. This involves identifying the problem, carrying out simple calculations and then drawing a plan for detailed experimental and computational work. It needs to be stressed here that mathematical modelling together with physical modelling and pilot plant investigation needs to be carried out in a complementary fashion. As shown in *Fig.(1.1)* several iterations between modelling and experimental work may be required to develop a reliable mathematical model.

Mathematical modelling, from a humble beginning has today developed into a very powerful tool capable of influencing our daily lives. Some of the notable successes of mathematical modelling have been in the accurate prediction of the election results based on extremely small samples, in weather forecasting and in the area of cold nuclear explosions. In the area of extractive metallurgy too, mathematical modelling has produced impressive results particularly in the last two decades. Some of the successful modelling examples are illustrated below :

- i. Aluminium extraction involves electrolytic deposition of alumina, dissolved in a molten salt using a graphite anode and a graphite cathode. A Hall-cell operation



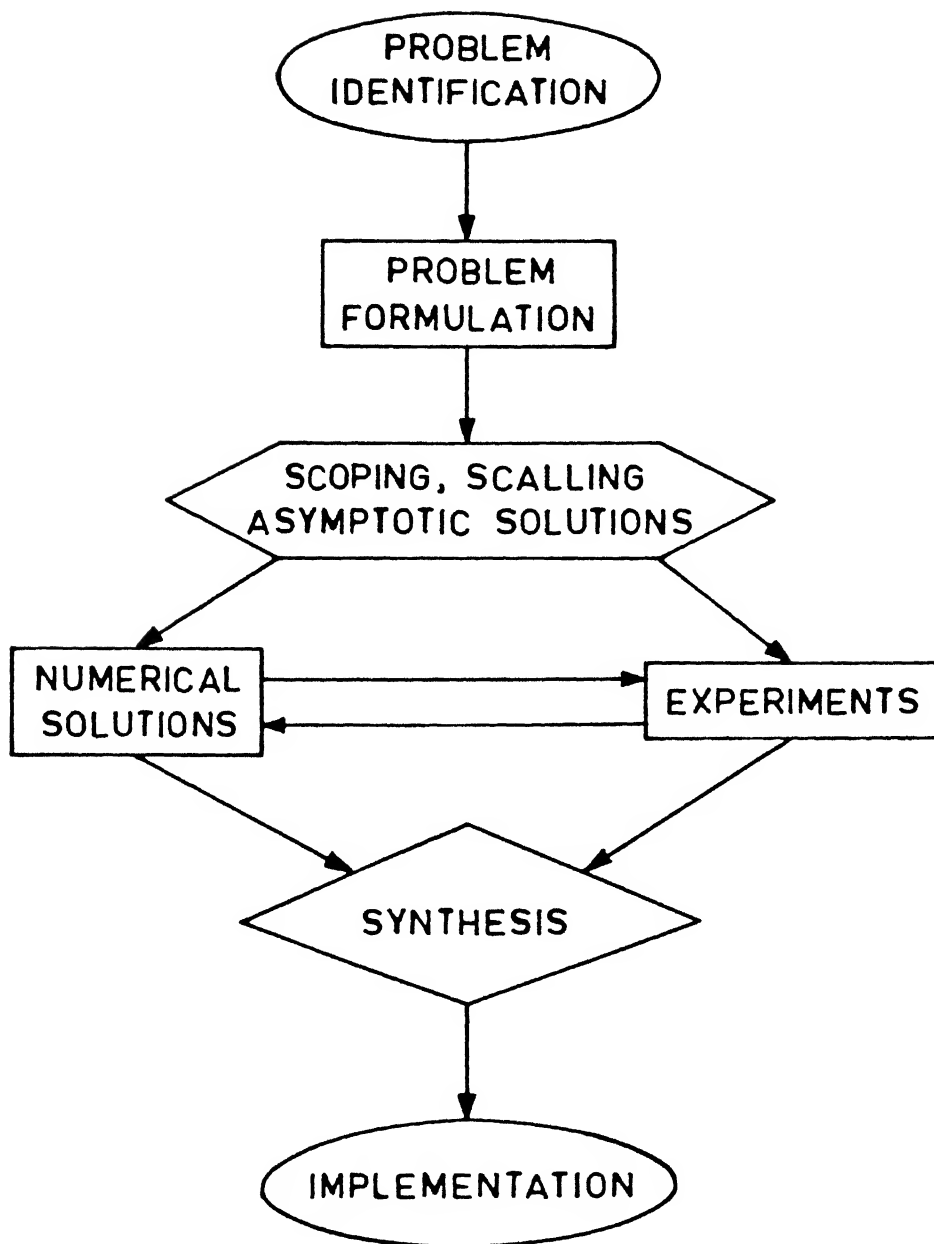


Fig.(1.1) : The general methodology of mathematical model development [2].

involves complex transport processes. The flow is unsteady and three dimensional and involves mass transfer in a multiphase ( metal, bath and gas ) system. Optimisation models [3,4] developed have not only helped in the evolution of better cell design but also in the better understanding of the process which has resulted in vast improvements in the area of cell productivity and current efficiency [5].

- ii. Continuous casting of steel is fast replacing the traditional ingot casting route as it is economically more attractive and also simplifies the process route by doing away with the maintenance intensive, primary rolling mills. However, the process of continuous casting involves solidification of the liquified metal in an oscillating mould which requires optimum process control. In the initial years, lack of proper understanding resulted in very high breakdowns and poor quality . Mathematical modelling of continuous casting helped in developing a better understanding of solidification in the mould and in designing of superior cooling systems for heat extraction from the mould [6,7]. This has resulted in controlling breakouts and in improving the quality of the continuous cast product.
- iii. Flash smelting of sulphide copper ores has inherent advantages of providing very high surface to volume ratio of the fine ore particles resulting in very high reaction rates. This has helped it in replacing the classical unwieldy reverberatory furnaces which provided very low surface area per unit volume and consequently, significantly lower processing rates. However, flash smelting is a very complex process involving a reacting two-phase, gas -solid mixture with several components. Mathematical modelling of this complex system helped in getting accurate information regarding temperature and concentration profiles [8,9] and of local reaction rates which helped in the design of larger and efficient flash smelters.

## **1.2 Scope of the Present Work**

The brief introduction to the thesis indicates that mathematical modelling in recent years

has emerged as a major process analysis tool for various metal processing operations. Despite numerous modelling exercises taken up over the years [2-9], there remains considerable scope in broadening the applicability of the mathematical (better called 'Process') models and their performance. A survey of the relevant literature indicates that mathematical modelling in the arena of metals processing has been most exhaustive in 2-D or axis-symmetrical systems. Transient two phase, 3-D calculations have been few and far between. Since, most metal processing operations do not involve *symmetry*, consequently the need for a three dimensional transport model can be readily visualized (analysis of asymmetric gas injection, dual plug bubbling, flow in a tundish etc. necessitates a three dimensional turbulent flow calculation procedure). Similarly, although flow computations in two dimensional systems have been relatively more abundant, the associated rates of various heat and mass transfer processes (melting, dissolution etc.) in such systems have not been adequately, theoretically investigated. A typical problem in this arena is the melting of solid additions in two dimensional, two phase, turbulent flow systems (axisymmetrical gas stirred ladles). Thus, despite melting in axisymmetrical gas bubble driven systems been a relatively well studied phenomena, from experimental point of view, not much mathematical modelling has been carried out [10,11,12]. In particular, the usefulness of mathematical models to investigate melting phenomena in axisymmetrical systems remains yet to be confirmed, particularly with reference to experimental data in high temperature systems.

In this thesis a 2-D, steady state, two phase, turbulent flow model was used to predict the distribution of flow variables and turbulence parameters in axisymmetric gas stirred vessels for both aqueous and high temperature systems. The hydrodynamic predictions were subsequently, coupled with a previously reported heat transfer correlation [13] to predict melting rates of spherical shaped additions in the gas stirred systems. The predictions from the model were compared with the experimental observations reported in literature on both aqueous and high temperature systems [14,15]. Alternative to this, a simple, yet effective, macroscopic procedure based on the 'Plume Model' [16] has been suggested to predict the melting rates of solids in gas stirred systems. Furthermore, two different but popularly used heat transfer correlations were tested to predict melting rates in order to assess their relative merits and

demerits.

In the second phase of the present work, the two dimensional code was modified for modelling a 3-D, steady state, two phase, turbulent flow situation (incorporating the two equation  $k-\epsilon$  model of turbulence) in cartesian co-ordinate system. The three dimensional code developed was extensively tested against available benchmark solutions. Subsequent to these, appropriate boundary conditions were incorporated and the 3-D calculation procedure was applied to predict melt flow in a simple rectangular shaped tundish with no flow control devices [17].

### 1.3 Layout of the Thesis

The main body of the thesis consists of six chapters. *Chapter-2* deals with modelling of melting phenomena in axisymmetric gas bubble driven systems. In this chapter, the broad outline of the steady, two phase turbulent model that was used as a starting point for the present investigation has also been elaborated upon. In *Chapter-3* the development of a three dimensional, steady state, two phase turbulence model starting from its 2-D counterpart has been presented. This included the governing equations, salient features of the formulation and model validation against benchmark solutions. Finally, in *Chapter-4*, the modelling of melt flow in metallurgical tundish systems are presented. *Chapter-5* summarises the general conclusions derived from the present work and the thesis concludes with the recommendation for future work in *Chapter-6*.

## CHAPTER - 2

# MODELLING OF MELTING RATES IN AXISYMMETRICAL GAS STIRRED SYSTEMS

As mentioned in the introduction ( *Chapter-1* ), an existing steady state, two phase, two dimensional turbulent flow model [18] was used as a starting point towards developing a three dimensional calculation procedure. In this chapter, the two dimensional turbulent flow model [18] is applied to investigate melting of solids in aqueous and high temperature axisymmetrical gas stirred systems. Once prediction from the existing *CFD* package is validated against experimental observations, reliability of the procedure [18] can be ascertained and hence, modification can be attempted with confidence.

### 2.1 Introduction

Melting is integral to many pyro-metallurgical operations carried out in both ferrous and non-ferrous industries. Large tonnage of scrap, ferro-alloys and de-oxidiser elements are added during the production of common metals and alloys. Melting of these additions consumes appreciable energy and hence, affects the process economics significantly. Consequently, there is considerable interest in identifying and understanding the phenomena at work during melting and subsequent dissolution of solid additives.

Melting is the result of heat transfer by free and / or forced convection from the bulk liquid to the surface of the solid. The flux of heat to the solid surface is expressed as :

$$q = h ( T_b - T_m ) \quad (2.1)$$

The corresponding rate of melting (say for a spherical shaped addition) can be readily derived from an appropriate heat balance and represented according to :

$$-\frac{dR}{dt} = \frac{h}{\rho_s \Delta H} (T_b - T_m) \quad (2.2)$$

Since  $T_b$  and  $T_m$  are typically constant for a given system, consequently, as seen from *Eqs*(2.1) and (2.2), the rate of melting, apart from the thermophysical properties, depends solely on the value of heat transfer coefficient,  $h$ . The heat transfer coefficient, inturn, depends on the flow conditions, thermo-physical properties of the bulk phase etc., and must be known *a-priori* so as to estimate the melting rates effectively via *Eq*.(2.2). Consequently, detailed information on fluid flow is required for the analysis and interpretation of melting phenomena.

Since rates of various transport processes can be greatly influenced by manoeuvring the flow conditions within a reactor vessel, consequently, submerged gas injection today has become dereguer to metal refining operations carried out in ladles, furnaces and transfer vessels. The gas rising as the two phase plume to the free surface induces a turbulent recirculatory motion of fluid and thereby, as is well known, exacerbates melting and / or dissolution of solid additives. In the subsequent section, the detailed calculation [18] procedure is first outlined and it is subsequently demonstrated how melting rates of solid additives can be predicted from the first principles.

## 2.2 Previous Work on Melting of Solids in Gas Stirred Baths

The subject of melting and dissolution of solid additions in gas stirred vessels has received considerable attention over the years. Many studies have been carried out in stagnant melts while relatively few studies have been made in stirred vessels. Thus, numerous studies on the melting of solids in metallurgical melts have been reported in the literature [10-12,14,15,19,20]. Here, however, studies pertaining to gas stirred bath have been considered and reviewed very briefly.

In general, two different approaches have been adopted by the researchers to theoretically deduce the relevant flow velocities and hence, the melting rates (e.g.,  $Nu = f(Re, Pr)$ ). These for example included,

- i. a simple macroscopic energy balance [10,14] and,
- ii. the numerical solution of the turbulent Navier-Stokes equations [14,11,12,20].

Szekely and co-workers [10] were among the first to investigate melting of ice cylinders in an aqueous model of gas stirred ladle system. On the basis of numerical solution of the turbulent Navier-Stokes equations and experimental observations, the following correlation was proposed:

$$Nu = 0.8 (Re Tu)^{0.8} (Pr)^{0.73} \quad (2.3)$$

Subsequently, Taniguchi and co-workers [14,15] carried out melting experiments in the plume region of aqueous and high temperature gas stirred baths. These authors [14,15] demonstrated that a modified form of Ranz-marshall correlation viz.,

$$Nu - 2 = (0.4 Re_D^{0.5} + 0.06 Re_D^{0.66}) Pr^{0.4} \left( \frac{\mu_b}{\mu_o} \right)^{0.25} \quad (2.4)$$

predicts melting rates fairly realistically and provides estimates that agree well with the experimental measurements. To this end however, Taniguchi et.al. [14,15] adopted a simple energy balance approach and proposed an expression, for estimating the characteristic velocity of the system (viz. the rise velocity of the two phase plume).

$$\frac{1}{2}(\pi r^2 \rho_l v) v^2 = W_B + 0.06 W_g \quad (2.5)$$

On the basis of such , Reynolds numbers ,  $Re_D$  , (Eq.(2.4)) and subsequently the Nusselt numbers were estimated. Predicted results were validated using experimental observations derived from high temperature and aqueous systems ( see Fig.(2.1)) None the less, as mentioned in detail towards the end of this chapter, the formulation of Taniguchi et.al. [14,15]

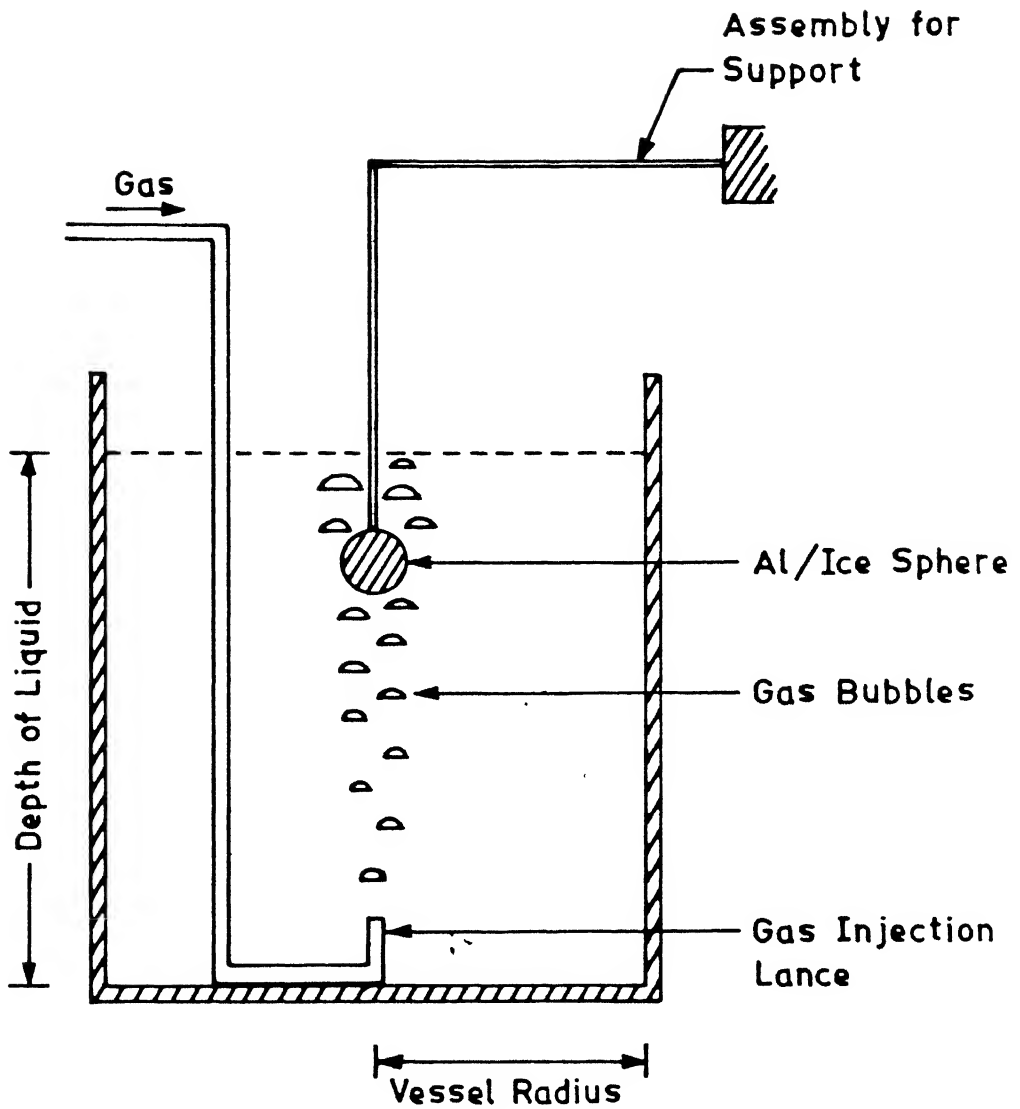


*Fig.(2.1) : Schematic of experimental setup of Taniguchi and co-workers [14,15].*



suffers from serious drawbacks. Consequently, an attempt has been made to simulate the experimental observations of Taniguchi et.al. [14,15] from a fundamental standpoint with the aid of a steady, two phase, two dimensional calculation procedure [18].

### **2.3 Mathematical Modelling of Fluid Flow in Axi-Symmetric Gas Injection Systems**

As mentioned already, melting rates in turbulent recirculatory flow system can be estimated provided the detailed information on flow fields in the system is known *a-priori*. Consequently, it is worthwhile to examine the flow calculation procedure [18] in some detail before attempts are made to predict melting rates.

There are two different computational procedures typically been adopted to mathematically describe the hydrodynamics of two phase buoyancy driven systems and these include:

- i. models derived on the Eulerian frame of reference which are further classified into two groups viz.,
  - a. the quasi single phase models and,
  - b. the two phase models
- ii. models derived on the Lagrangian-Eulerian frame of reference.

Traditionally, the relatively simple quasi-single phase calculation procedure has been more popular. However, two phase calculation procedures are relatively more rigorous and generalised. In the present study, as mentioned already a steady state, two phase, combined Lagrangian-Eulerian approach has been adopted to model the flow phenomena in the axisymmetrical gas stirred system. As against a Eulerian two phase calculation procedure, the present method is computationally less demanding [18] . In this, the motion of the gas phase is computed numerically in a Lagrangian frame in the form of steady stream of bubbles, while

the liquid motion together with the associated level of fluid turbulence were calculated by the routinely applied Eulerian scheme.

### 2.3.1 Modelling assumptions

To mathematically model submerged gas injection operations in axisymmetric vessels using a combined Lagrangian-Eulerian approach, following idealisations and approximations were made:

- i. The presence of any overlying second phase was ignored and the melt-air surface was assumed to be flat.
- ii. The melt was assumed to be isothermal.
- iii. Following axial symmetry in the present geometry of gas injection, variations of flow properties along the angular direction were ignored.
- iv. Discrete mono-size bubbles were assumed to be form at the lance tuyere tip. Thus the size of the bubbles formed at the tip was known *a-priori*. From the principle of volume continuity the corresponding bubble frequency was calculated.
- v. Bubble-bubble interactions were assumed to be negligible and hence, drag coefficient correlation, applicable to the single bubble-fluid system was applied for the appropriate range of Eotvos and Reynolds numbers.
- vi. Bubble within the upwelling plume contribute to the generation of turbulence and this inturn affects the bubble motion.
- vii. The flow is essentially Newtonian and incompressible and finally,
- viii. The flow is steady, turbulent and recirculatory.

## 2.4 Description of the Steady State, Two Phase, Two Dimensional Turbulent Flow Model

A brief outline of the combined Eulerian-Lagrangian two phase, two dimensional turbulent flow model developed earlier by Mazumdar and Guthrie [18] is presented below. The

governing equations together with their associated boundary conditions applicable to axisymmetrical gas stirred systems are summarised below in terms of the polar coordinate system.

#### 2.4.1 The liquid phase flow equations

The governing equations in terms of the cylindrical polar co-ordinate system (  $r$ ,  $\theta$ ,  $z$  ) chosen, can be represented as:

*Equation of continuity:*

$$\frac{\partial}{\partial z} (\rho_l \alpha_l u) + \frac{\partial}{\partial r} (\rho_l \alpha_l r v) = 0 \quad (2.6)$$

*Equation of motion in the axial direction :*

$$\frac{\partial}{\partial z} (\rho_l \alpha_l uu) + \frac{1}{r} \frac{\partial}{\partial r} (\rho_l \alpha_l r uv) = -\alpha_l \frac{\partial p}{\partial z} + 2 \frac{\partial}{\partial z} (\alpha_l \mu_e \frac{\partial u}{\partial z}) + \frac{1}{r} \frac{\partial}{\partial r} (r \mu_e \alpha_l \frac{\partial u}{\partial r}) + \frac{1}{r} \frac{\partial}{\partial r} (r \mu_e \alpha_l \frac{\partial v}{\partial z}) + F_z \quad (2.7)$$

*Equation of motion in the radial direction:*

$$\frac{\partial}{\partial z} (\rho_l \alpha_l uv) + \frac{1}{r} \frac{\partial}{\partial r} (\rho_l \alpha_l r vv) = -\alpha_l \frac{\partial p}{\partial r} + \frac{\partial}{\partial z} (\alpha_l \mu_e \frac{\partial v}{\partial z}) + \frac{2}{r} \frac{\partial}{\partial r} (r \mu_e \alpha_l \frac{\partial v}{\partial r}) + \frac{\partial}{\partial z} (r \mu_e \alpha_l \frac{\partial u}{\partial r}) + \frac{2v \mu_e \alpha_l}{r^2} + F_r \quad (2.8)$$

#### 2.4.2 The liquid phase turbulence model

In the present study, a modified form of standard coefficient  $k$ - $\epsilon$  model of Launder and Spalding [21] was used. The governing equations for turbulence kinetic energy ,  $k$  and its dissipation rate ,  $\epsilon$  , can be represented in the cylindrical polar co-ordinates (  $r$ ,  $\theta$ ,  $z$  ) as:

Equation of turbulence kinetic energy,  $k$  :

$$\frac{\partial}{\partial z}(\rho_l \alpha_l \mu k) + \frac{1}{r} \frac{\partial}{\partial r}(\rho_l \alpha_l r v k) = \frac{1}{r} \frac{\partial}{\partial r}(r \alpha_l \frac{\mu_T}{\sigma_k} \frac{\partial k}{\partial r}) + \frac{\partial}{\partial z}(\alpha_l \frac{\mu_T}{\sigma_k} \frac{\partial k}{\partial r}) + \alpha_l (G_k \rho_l \epsilon + P_b) \quad (2.9)$$

Equation of dissipation rate of turbulent kinetic energy,  $\epsilon$  :

$$\frac{\partial}{\partial z}(\rho_l \alpha_l \mu \epsilon) + \frac{1}{r} \frac{\partial}{\partial r}(\rho_l \alpha_l r v \epsilon) = \frac{1}{r} \frac{\partial}{\partial r}(r \alpha_l \frac{\mu_T}{\sigma_\epsilon} \frac{\partial \epsilon}{\partial r}) + \frac{\partial}{\partial z}(\alpha_l \frac{\mu_T}{\sigma_\epsilon} \frac{\partial \epsilon}{\partial r}) + \alpha_l (\frac{C_1 G_k \epsilon}{k} - C_2 \rho_l \frac{\epsilon^2}{k} + P_b \frac{\epsilon}{k}) \quad (2.10)$$

In Eqs(2.9) and (2.10),  $G_k$  is the volumetric rate of turbulence production, and is defined as:

$$G_k = \mu_T [2[(\frac{\partial u}{\partial z})^2 + (\frac{\partial v}{\partial r})^2 + (\frac{v}{r})^2] + (\frac{\partial u}{\partial r} + \frac{\partial v}{\partial z})^2] \quad (2.11)$$

The eddy viscosity,  $\mu_e$ , appearing in Eqs(2.7) and (2.8) is defined as :  $\mu_e = \mu_T + \mu_l$ , in which,

$$\mu_T = \frac{C_\mu \rho_l k^2}{\epsilon} \quad (2.12)$$

The five empirical constants of the  $k$ - $\epsilon$  model viz.,  $C_1$ ,  $C_2$ ,  $C_\mu$ ,  $\sigma_k$  and  $\sigma_\epsilon$  were assigned to their standard values [21] . These are summarised in Table-2.1.

Table-2.1 : Values of constant used in a k- $\epsilon$  model.

$C_1$	$C_2$	$\sigma_k$	$\sigma_\epsilon$	$C_\mu$
1.43	1.92	1.00	1.30	0.09

### 2.4.3 Equation of motion of the gas phase

As mentioned already, the motion of the gas phase has been carried out via a Lagrangian approach, in which the trajectories of the individual bubbles are stochastically determined in space by solving two differential equations in time. The appropriate form of

Newton's second law of motion that describes the bubble motion, can be represented along the two co-ordinate axis ,  $r$  and  $z$ , according to:

*Axial direction,  $z$  :*

$$(1 + 0.5 \frac{\rho_l}{\rho_g}) \frac{dV_{B,z}}{dt} = - \frac{3\mu_l}{4d_b^2 \rho_g} C_D Re (V_{B,z} - U) + \frac{\rho_l}{\rho_g} [U \frac{\partial u}{\partial z} + V \frac{\partial u}{\partial r}] + (1 - \frac{\rho_l}{\rho_g}) g \quad (2.13)$$

*Horizontal / Radial direction,  $r$ :*

$$(1 + 0.5 \frac{\rho_l}{\rho_g}) \frac{dV_{B,r}}{dt} = - \frac{3\mu_l}{4d_b^2 \rho_g} C_D Re (V_{B,r} - V) + \frac{\rho_l}{\rho_g} [U \frac{\partial v}{\partial z} + V \frac{\partial v}{\partial r}] \quad (2.14)$$

The two corresponding kinematic relationships, which define the trajectories of bubbles within the two dimensional flow domain are:

$$\frac{dz}{dt} = V_{B,z} \quad (2.15)$$

and ,

$$\frac{dr}{dt} = V_{B,r} \quad (2.16)$$

The instantaneous drag coefficient,  $C_D$ , in the *Eqs*(2.13) and (2.14) was evaluated using an experimentally determined correlation [22] for oblate spheroid / spherical capped bubbles:

$$C_D = \frac{0.622}{[\frac{1}{E_o} + 0.235]} \quad ; \quad (500 < Re < 5000) \quad (2.17)$$

Furthermore,  $Re$  in *Eqs*(2.13) and (2.14) is the Reynolds number, and is estimated on the basis of absolute magnitude of the relative velocity vector,  $U_r$ , i.e.

$$Re = \rho_l d_b \left[ \frac{U_b - U_r}{\mu_l} \right] \quad (2.18)$$

Similarly in Eqs(2.13) and (2.14),  $U$  and  $V$  are the instantaneous components of fluid motion, and were estimated by summing up the relevant mean velocity components ( $u$  and  $v$ ) with the corresponding fluctuating velocity components assuming turbulent fluctuations are essentially isotropic and obey a Gaussian probability distribution function. On the basis of such,

$$U = u + \Psi \left( \frac{2k}{3} \right)^{\frac{1}{2}} \quad (2.19)$$

where  $\Psi$  is a normally distributed random variable and varies between -1 and 1. Thus during the rise of the bubble through the liquid, the velocity fluctuations were estimated stochastically and were assumed to remain constant for a time period, equivalent to the eddy life time,  $\tau$ . The life time of an eddy, during which a characteristic velocity fluctuation was assumed to persist, is estimated from the turbulence theory according to [23]:

$$\tau = 0.195 \frac{k}{\epsilon} \quad (2.20)$$

#### 2.4.4 Estimation of gas voidages

Figure (2.2) illustrates a typical section of the grid network and a bubble trajectory intercepting the Eulerian grid system. For a scalar control volume the corresponding gas voidages can be readily estimated from the principle of volume continuity, according to :

$$\alpha_g = \frac{\text{volume of gas}}{\text{volume of control volume}} = \frac{Q_g(N+1)\Delta t}{2\Delta V_{cv}} \quad (2.21)$$

These are summarised elsewhere in detail [18] and consequently, not reproduced here. Once  $\alpha_g$  values have been determined for each of the control volumes, corresponding liquid volume fraction,  $\alpha_l$ , can be easily determined, from  $\alpha_g + \alpha_l = 1.0$ .

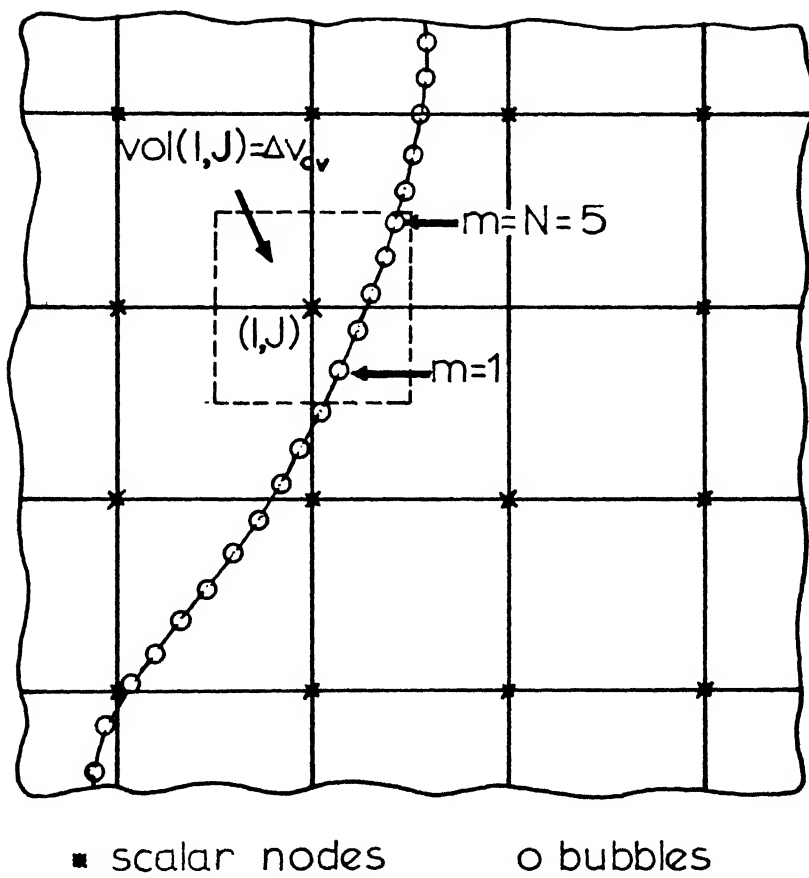


*Fig.(2.2)* : Schematic of a section of Eulerian grid network intercepted by a bubble trajectory.

### 2.4.5 Estimation of turbulence production ( $P_b$ ) due to bubbles and interphase friction forces ( $F_z$ ) and ( $F_r$ )

Bubbles in a two phase region contribute significantly to the total turbulence generation [24]. The additional turbulence produced by the bubbles can be considered to be equivalent to the shear work performed on the liquid by the bubbles and therefore, the corresponding volumetric flow rate of turbulence generation,  $P_b$ , can be represented as :

$$P_b = C_b \frac{Q_t}{N\Delta V_{cv}} \sum \int \frac{3\mu_l C_D Re}{4d_b^2} (V_B - U_f)^2 dt \quad (2.22)$$

where,  $V_B$  is the resultant bubble velocity and  $U_f$  is the resultant fluid velocity.  $C_b$  in Eq.(2.22) is a constant and takes a value between 0 and 1. The value of  $C_b$  depends on the physical characteristic of the two phase plume ( e.g., bubble population, bubble size etc.). The constant  $C_b$  is normally determined by trial and error.

The momentum exchange terms  $F_z$  and  $F_r$  can be evaluated assuming that drag forces experienced by bubbles act with equal magnitude but opposite directions in the liquid phase. The expressions for  $F_z$  and  $F_r$  can be represented in the compact tensorial notation as :

$$F_i = \frac{Q_t}{N\Delta V_{cv}} \sum \int \frac{3\mu_l C_D Re}{4d_b^2} (V_{B,i} - U_i) dt \quad (2.22)$$

### 2.4.6 The boundary conditions

The boundary conditions applied to the numerical solution of the set of governing equations for fluid flow and turbulence in axisymmetrical gas stirred systems are represented schematically in Fig.(2.3) and are as follows:

*At the axis of symmetry ( $r = 0$ ,  $0 < z < L$ )*



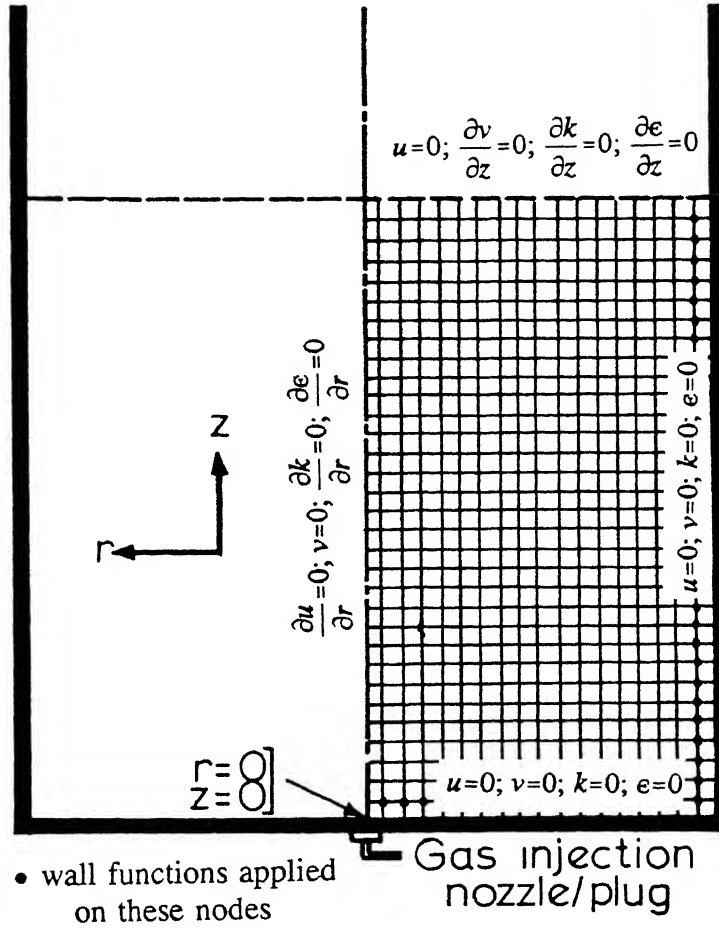


Fig.(2.3) : Schematic of the vessel geometry and the corresponding boundary conditions applied towards numerical simulation of axi-symmetric gas stirred ladle system.

$$v = 0 \quad ; \quad \frac{\partial u}{\partial r} = \frac{\partial k}{\partial r} = \frac{\partial \epsilon}{\partial r} = 0$$

*At the free surface of the liquid (  $z = L$  ,  $0 < r < R$  )*

$$u = 0 \quad ; \quad \frac{\partial u}{\partial z} = \frac{\partial k}{\partial z} = \frac{\partial \epsilon}{\partial z} = 0$$

*At the side walls (  $r = R$  ,  $0 < z < L$  ) and bottom surface (  $z = 0$  ,  $0 < r < R$  )*

$$u = v = k = \epsilon = 0$$

Close to the rigid boundaries ( viz., the walls and the bottom surface ) where the variations in the flow properties are steep, the momentum (  $u$  and  $v$  ) and the scalar field (  $k$  and  $\epsilon$  ) have consequently been modelled using the routine wall function procedure [21,32] i.e. logarithmic law of wall for the velocity component parallel to it (see *Chapter-4* for details). In addition to these the appropriate gas inlet velocity was applied as the required initial condition through *Eqs.(2.13) and (2.14)*.

#### **2.4.7 The numerical solution procedure**

The basic structure of the present combined Langrangian-Eulerian procedure has been:

- i. The total flow is equally divided between a preconsidered number of trajectories. On the basis of such, flow rate (  $Q_i$  ) per trajectory is estimated.
- ii. The equations for bubble motion are solved for each of the trajectories and then superimposed on the Eulerian grid. From these, overall distributions of  $\alpha_i$  ,  $F_-$  and  $F_r$  etc are estimated.
- iii. Estimated  $\alpha_i$  ,  $F_-$  and  $F_r$  are incorporated into the equations of the continuous phase ( viz., the liquid ) and solved iteratively by embodying the *SIMPLE* procedure of Patankar and Spalding [26].
- iv. At the end of a predetermined number of iterations of the liquid phase equations, the

trajectories of the bubbles are recalculated using the prevalent flow and turbulence fields. Based on this the distribution of  $\alpha_i$  ,  $F_z$  and  $F_r$  etc. were updated. The above steps are repeated till the converged solution is not obtained.

The flow circuit of the computer program applied to the present investigation has been illustrated in *Fig.(2.4)*.

## 2.5 The Heat Transfer Model

Once the flow velocities and turbulence parameters are predicted as a function of operating conditions, one of the many empirical expressions available in literature can be applied to quantify heat transfer between a submerged solid sphere and a continuous phase. For the system configuration considered in this work ( see *Fig.(2.1)* ) , the relationship proposed by Whitaker [13] was adopted.

$$Nu-2 = ( 0.4 Re_D^{0.5} + 0.06 Re_D^{0.66} ) Pr^{0.4} \left( \frac{\mu_b}{\mu_o} \right)^{0.25} \quad (2.24)$$

In *Eq.(2.24)*,  $Re_D$  , is the object Reynolds number that embodies the initial diameter of the solid sphere and the characteristic velocity prevalent in the neighbourhood of the solid sphere. It is instructive to note here that *Eq.(2.24)* was originally developed for heat transfer between a heated metal sphere and a bulk single phase fluid ( air ). As discussed elsewhere [13-15] , the above correlation was found to be applicable to turbulent, two phase flow systems as well.

## 2.6 Results and Discussion

To assess the predictive capability of the model developed in the present study ,the experimental study reported earlier by Taniguchi et.al. [14,15] was applied as the reference. Thus, for the given vessel geometry (see *Fig.(2.1)*) and gas flow rates, the flow distributions

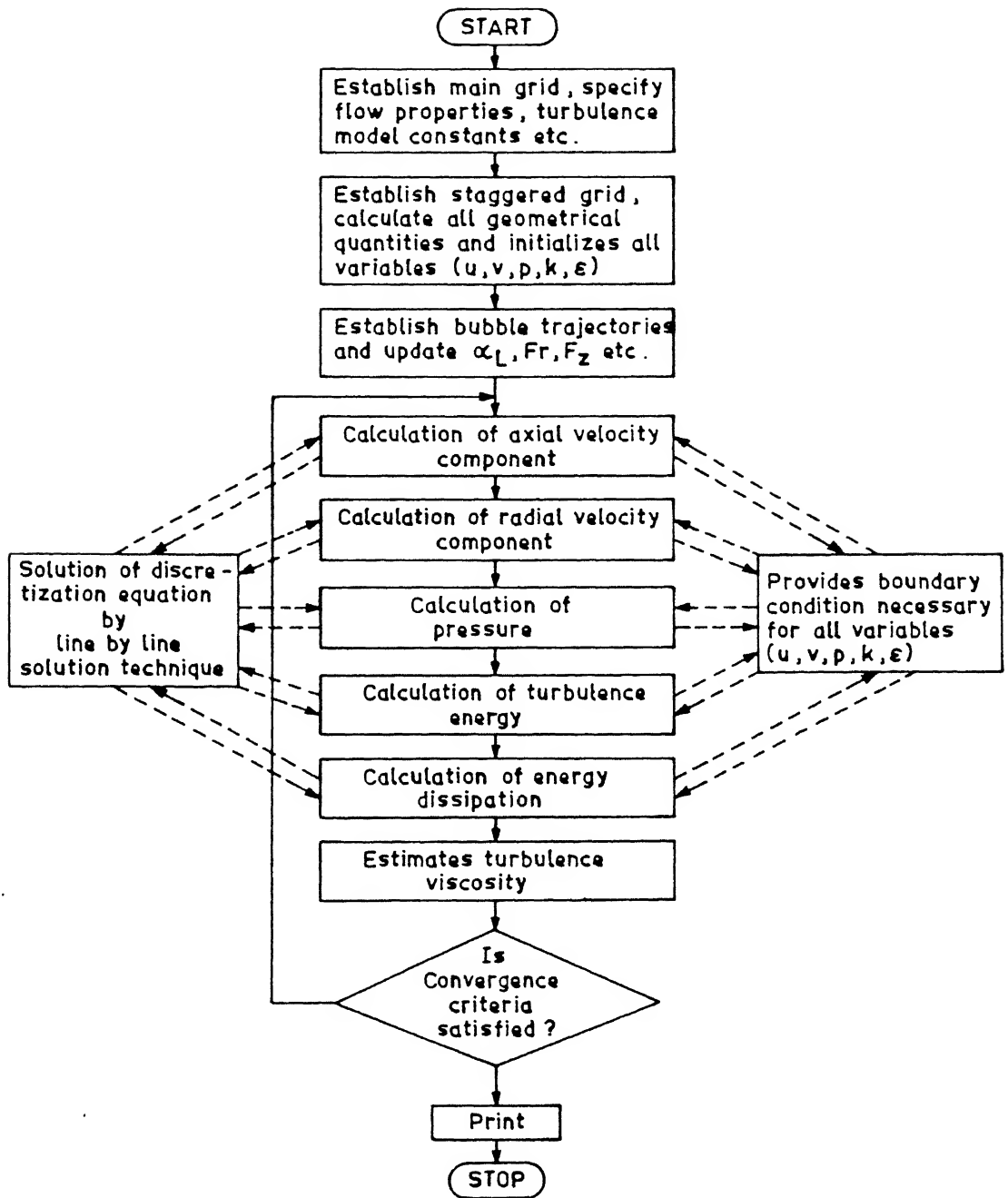


Fig.(2.4) : Flow diagram of the two dimensional, two phase turbulent flow model [18].

were estimated first through the numerical solution of *Eqs.*(2.6) through (2.23). Subsequent to this the Reynold numbers,  $Re_D$ , were calculated ( *Table-2.2*) via. the following expression, embodying the predicted velocity prevalent in the vicinity of the solid spheres viz.,

$$Re_D = \frac{D \sqrt{u^2 + v^2} \rho_l}{\mu_l} \tag{2.25}$$

Incorporating such estimates and the relevant thermo-physical properties ( *Table-2.2*) in *Eq.*(2.24), Nusselt numbers were estimated. In *Fig.*(2.5) a log-log plot between the experimental Nusselt number [14,15] and the present estimates of the Reynolds number (see *Table-2.2*) is shown together with the theoretical line for *Eq.*(2.24). There the dependency of the experimental Nusselt number on the numerically predicted Reynolds number appears to have been simulated reasonably well by the present mathematical model.

Table-2.2: Characteristic of the experimental work of Taniguchi et.al. and the present estimates of the liquid rise velocity and  $Re_D$  in the aqueous and high temperature systems :

(a) Aqueous Model

Experimental set up	Temp, $T_b$ , (K)	$V \times 10^6$ , (Nm <sup>3</sup> /s)	$Q \times 10^6$ , (m <sup>3</sup> /s )	Mean Liquid rise velocity in the vicinity of the sphere, (m/s)		Estimated $Re_D$	
				Numerical Prediction	<i>Eq.</i> (2.28)	Numerical	Macro- scopic
$L = 0.36$ m							
$R = 0.075$ m	293	1.07	1.03	0.063	0.082	2259	2926
$D = 0.036$ m							
$\mu_b = 1.02 \times 10^{-3}$	293	7.38	7.11	0.155	0.157	5558	5579
$\mu_o = 1.83 \times 10^{-3}$							
$Pr = 7.158$	293	29.51	28.41	0.301	0.247	10758	8853

@ all units in S.I.system

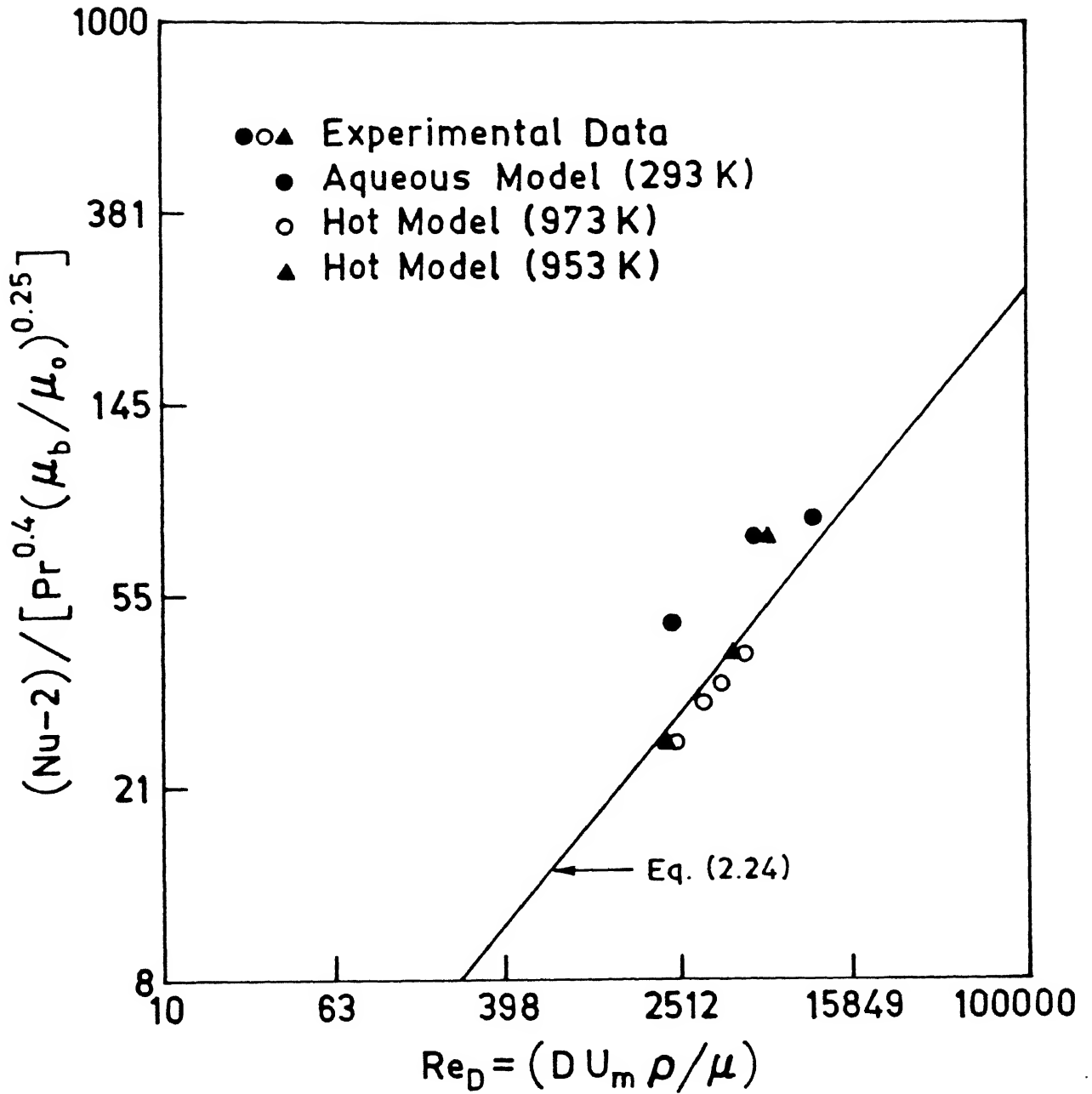


Fig.(2.5) : A log-log plot between the experimental Nusselt number [14,15],  $(Nu-2)/\{Pr^{0.4} (\mu_b / \mu_o)^{0.25}\}$  and the present estimates of the Reynolds number,  $Re_D$ , vis a vis the line for Eq.(2.24). (Deduced through numerical simulation).

(a) High temperature Model

Experimental set up	Temp , $T_b$ , (K)	$V \times 10^6$ , ( $Nm^3/s$ )	$Q \times 10^6$ , ( $m^3/s$ )	Mean Liquid rise velocity in the vicinity of the sphere ( $m/s$ )		Estimated $Re_D$	
				Numerical Prediction	Eq.(2.28)	Numerical	Macro- scopic
$L = 0.2 \text{ m}$	953	0.98	3.01	0.067	0.124	2206	4083
$R = 0.04 \text{ m}$	953	3.08	9.47	0.132	0.182	4347	5993
$D = 0.024 \text{ m}$	953	8.83	27.13	0.196	0.258	6454	8496
$\mu_{953} = 1.72 \times 10^{-3}$	973	0.98	3.08	0.069	0.125	2383	4318
$\mu_{973} = 1.64 \times 10^{-3}$	973	1.58	4.97	0.092	0.147	3178	5077
$Pr_{953} = 0.0211$	973	2.08	6.54	0.112	0.161	3869	5561
$Pr_{953} = 0.0197$	973	3.08	9.68	0.142	0.183	4912	6321

@ all units in S.I.system

Numerical results as are well known, depend on various assumptions and approximations applied to the mathematical model. In the present study the predicted results are expected to be sensitive to the precise choice of values of the bubble diameter  $d_b$ , drag coefficient  $C_D$ , the empirical constant  $C_b$ , as well as to various numerical parameters such as grid size, convergence criteria etc. To access the affect of these parameters on the computed results, extensive numerical experimentation was carried out for the aqueous system at the gas flow rate of  $29.51 \times 10^{-6} Nm^3/s$ . To this end several grid systems viz.,  $14 \times 8$ ,  $18 \times 10$ ,  $24 \times 16$  were tested to arrive at the grid independent solution. The liquid rise velocity in the vicinity of the solid sphere obtained by the three grid systems are shown in *Table-2.3*.

These clearly indicate that refining the grid beyond  $(18 \times 10)$  did not bring in any significant changes in the -predicted results. Similar trials with different convergence criteria indicated that the absolute value of sum on residuals on  $u$ ,  $v$ ,  $p$ ,  $k$  and  $\epsilon$  over the whole flow domain has to fall below  $5 \times 10^{-3}$  (S.I.units) in order to arrive at a converged solution. All the results provided in this text were derived on the basis of a  $18 \times 10$  grid system and the above

mentioned convergence criterion ( for definition see *Chapter-4*).

**Table-2.3** : Sensitivity of the predicted axial velocity to the various grid configurations applied.

( Aqueous system,  $L = 0.36\text{ m}$ ,  $R = 0.075\text{ m}$ ,  $Q = 29.51 \times 10^{-6}\text{ Nm}^3/\text{s}$  )

Grid System, ( $z \times r$ )	Mean rise vel. in the vicinity of sphere, ( $m/s$ )	Estimated $Re_D$	Estimated $Nu$	Estimated $\log Nu$
14 x 8	0.23	8616	120.4	2.08
18 x 10	0.30	10758	136.5	2.14
24 x 16	0.29	10411	134.0	2.13

Considerable uncertainties can be associated with the value of the bubble diameter which forms an integral input to the present mathematical model. In a gas stirred system a wide spectrum of bubble size can be envisaged in the plume. Consequently, a fair degree of idealisation has been involved while applying a single characteristic value of bubble diameter for such systems. Hence, the bubble diameter value was varied arbitrarily in the computational procedure within a range of  $\pm 30\%$  from the reported experimental value [14,15]. While varying the bubble diameter value for a given gas flow rate, due care was taken so that volume continuity remains satisfied. Numerically predicted axial velocity component as a function of three different bubble diameters is shown in *Fig.(2.6)* for a dimensionless height,  $z/H = 0.5$ . There, as seen, the axial velocity within the plume region appears to be sensitive to the value of the bubble diameter, while outside the two phase region, predicted axial velocity seems to remain practically unaffected by such variations. For a given flow rate, finer sized bubbles increase the surface area to volume ratio and therefore lead to a higher drag force ( $F_D \propto 1/d_b^2$



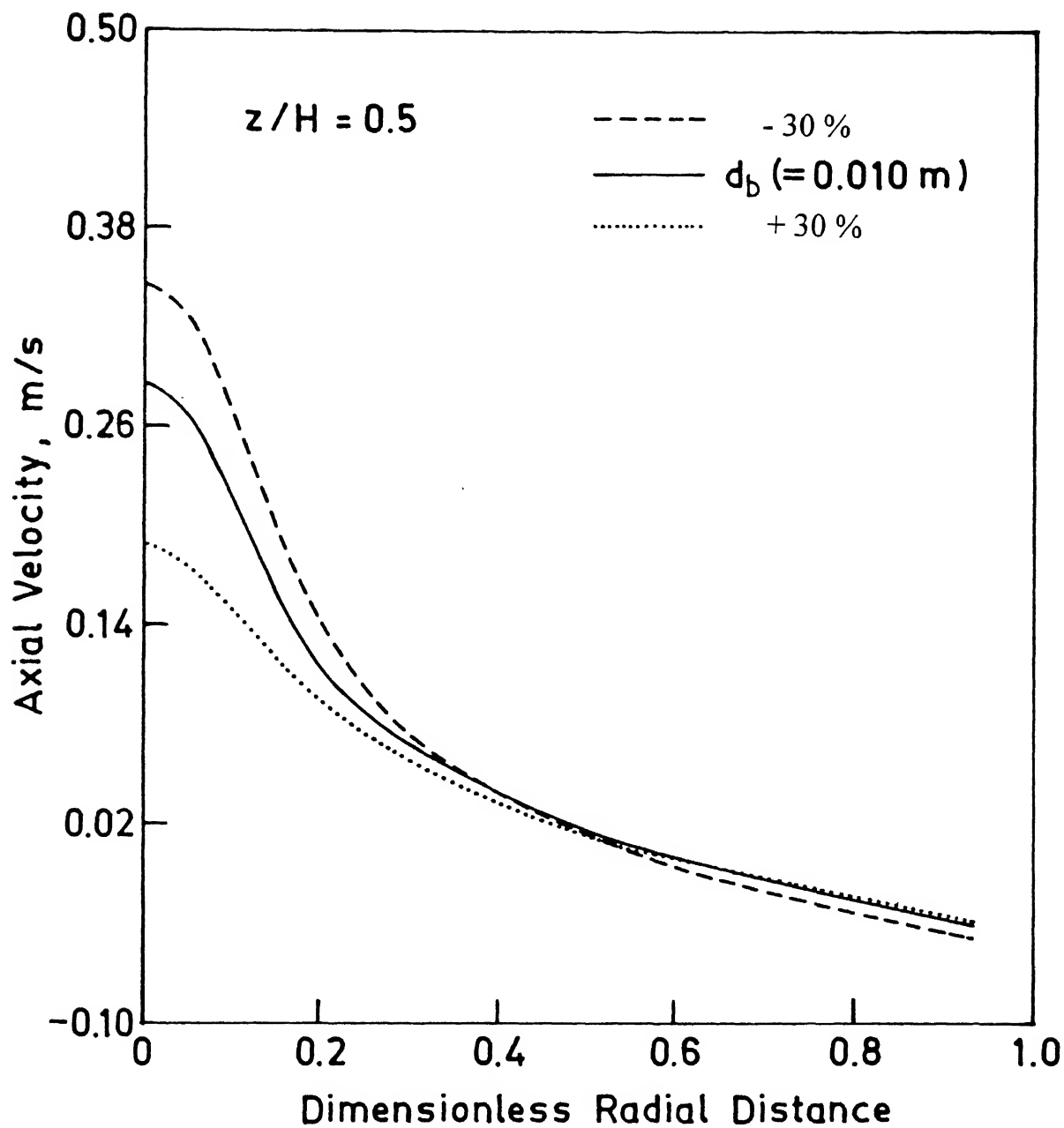


Fig.(2.6) : Sensitivity of the predicted vertical velocity component to the diameter of monosize bubbles ( $d_b$ ) assumed to be forming at the lance tuyere tip.

) which in turn leads to higher fluid rise velocity, particularly in the plume region.

Similarly, the drag coefficient ( $C_D$ ) appearing in *Eqs*(2.13) and (2.14) was also varied in the range of  $\pm 10\%$ . It is important to mention here, that drag coefficient is a function of the bubble diameter. Consequently, uncertainty in the value of the bubble diameter is also likely to introduce some uncertainty ( of course, to a smaller extent ) in the value of the estimated drag coefficient. As illustrated in *Fig*(2.7) the sensitivity of the predicted axial velocity component to different drag coefficient values was found to be minimal in the bulk ( outside the plume region ) of the liquid. However, in the plume region, the rise velocity was found to vary appreciably, almost to a factor by 2. Since a higher drag coefficient leads to a higher drag force, consequently, one can anticipate that the rise velocity of the liquid in the two phase plume region will increase with any increase in ' $C_D$ ' value.

Table-2.4: Variations in the estimates of Nusselt number as a function of the bubble diameter ( $d_b$ ), drag coefficient ( $C_D$ ) and coefficient of turbulence generation ( $C_b$ ).

Parameter	Numerical Value of the Parameter	Mean rise vel. in the vicinity of sphere, (m/s)	Estimated $Nu$ number
Bubble Diameter ( $d_b$ )	0.007 m	0.36	159.5
	0.010 m	0.30	136.5
	0.013 m	0.19	105.8
Drag Coefficient ( $C_D$ )	2.40	0.26	126.1
	2.67	0.30	136.5
	2.94	0.35	148.8
Empirical constant, $C_b$	0.0	0.30	136.5
	0.5	0.26	126.1
	0.7	0.22	114.8
	0.9	0.09	105.8

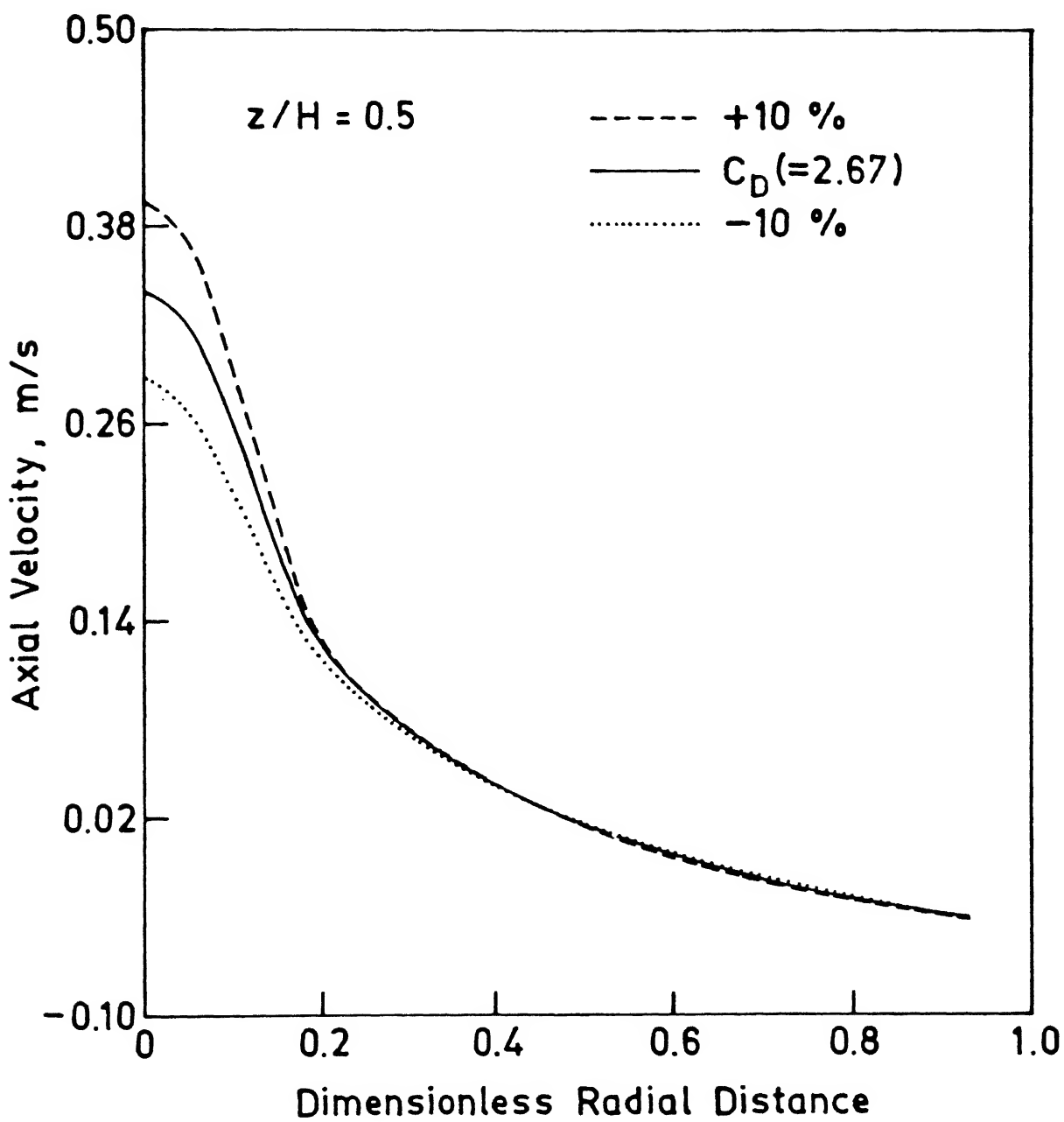


Fig.(2.7) : Sensitivity of the predicted vertical velocity component to the value of drag coefficient ( $C_D$ ).

The coefficient ' $C_b$ ' appearing in *Eq.(2.22)*, as mentioned already, is a function of the bubble population, shape and size etc. and hence, is difficult to precisely quantify in such gas stirred system. To ascertain the influence of this variable on the predicted results, four different but plausible values of ' $C_b$ ' ( 0, 0.5, 0.7 and 0.9 ) were applied to the calculation procedure. Results thus obtained have been illustrated in *Fig.(2.8)*. There, the axial velocity is seen to be dependent of some extent on the value of ' $C_b$ ' particularly in the plume region. A similar trend was found for the number of bubble trajectories. Increase in the number of bubble trajectories was found to lead to a higher liquid rise velocity within the plume. It is instructive to note here that marked variations in the velocity within the plume region do not translate by the same order in the bulk, since the plume barely occupies 1 to 2 % of the reactor volume.

The results presented so far appear to indicate that assumption on the bubble size, drag coefficient etc. embodied in the mathematical model are very likely to effect the predicted results, and hence the inferences drawn therefrom. The extent of such influence as shown on *Figs(2.6) through (2.8)*, while is expected to be only marginal in the bulk phase region, is likely to be more pronounced in the two phase region of the vessel. The present work therefore, suggests that sufficiently accurate information on the bubble diameter ( $d_b$ ), the drag coefficient ( $C_D$ ), and coefficient for turbulence generation for bubbles ( $C_b$ ) is needed, if fluid flow and the associated heat and mass transfer phenomena are to be predicted realistically via. such two phase calculation procedure. Fortunately, however as the melting rates are a weak function of velocity,  $Nu \propto u^{1/2}$  (see *Eq.(2.24)*), such uncertainties in the predicted rise velocity are likely to have relatively small influence on the predicted melting rates of solids as illustrated in *Table-2.4*.

## 2.7 An Alternative Macroscopic Formulation

In the absence of any computational facility, it is worthwhile to examine the adequacy of a simple alternative procedure for predicting melting rates in such systems. In their extensive study of the melting phenomena Taniguchi at.al. [14,15] proposed a simple energy balance

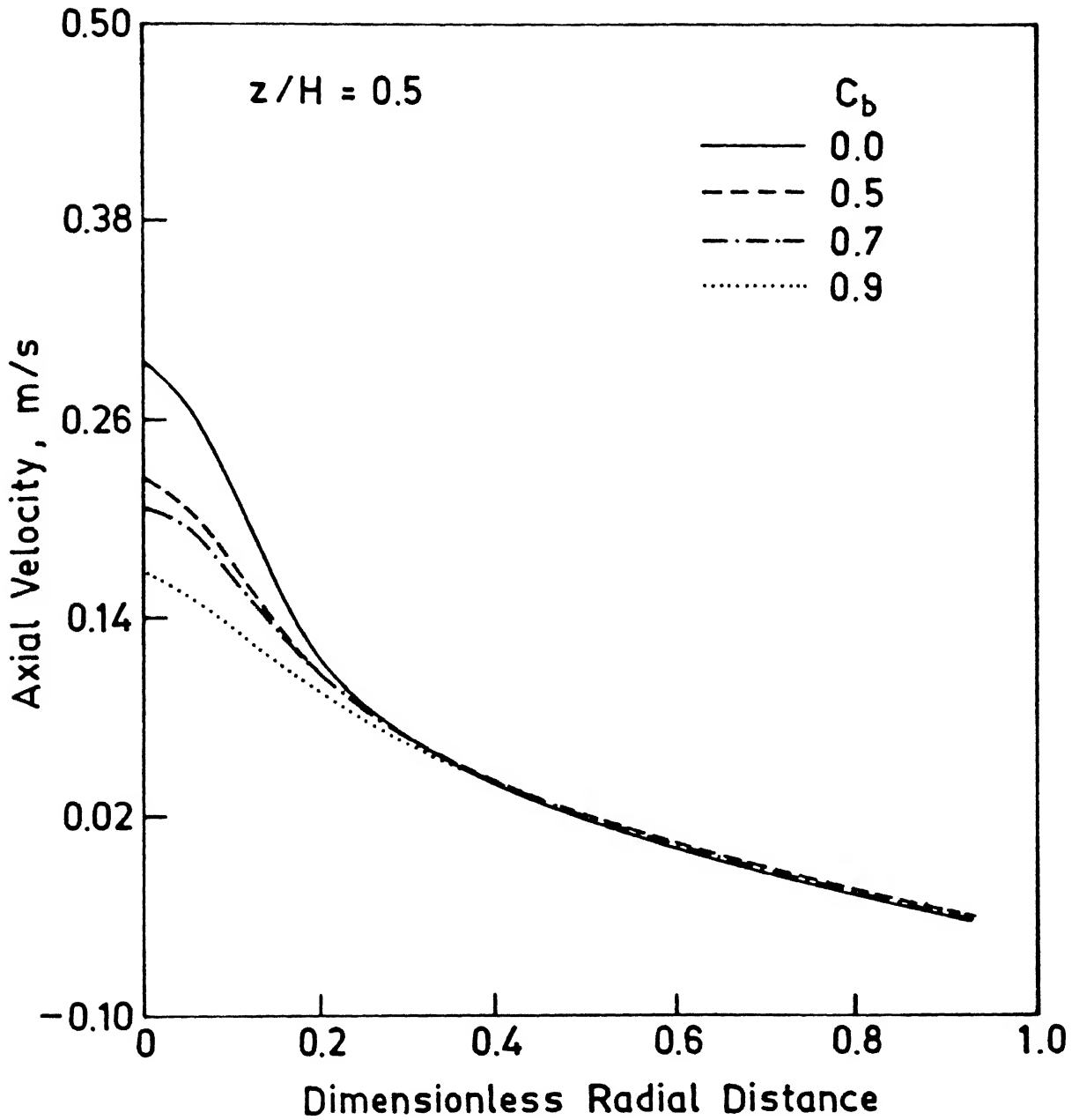


Fig.(2.8) : Sensitivity of the predicted vertical velocity component to the value of coefficient of turbulence generation by bubbles ( $C_b$ ).

relationship for estimating the liquid rise velocity in the two phase gas-liquid plume region, e.g.,

$$\frac{1}{2}(\pi r^2 \rho_l v) v^2 = W_B + 0.06 W_g \quad (2.26)$$

In *Eq.(2.26)*,  $W_B$  and  $W_g$  are respectively, the rate of buoyancy and the kinetic energy input to the system and were assumed known from the operating conditions viz., vessel radius, gas flow rate, nozzle diameter etc. Similarly  $v$  is the mean upward flow in the two phase region (see *Fig.(2.1)*) and  $r$  is the average radius of the bubble plume. The value of  $r$  was determined experimentally by Taniguchi et.al. and embodied in *Eq.(2.26)* for estimating the mean upward velocity,  $v$ , in the two phase plume region.

Numerous experimental studies reported to date on the gas stirred ladle system appear to indicate that the measurement of the gas-liquid plume parameters is somewhat uncertain owing to the dynamic nature of the bubble plume. Such two phase plume, in general exhibits long and short term wandering [27] and thus makes it difficult to measure  $r$  realistically. In industrial gas stirred reactors, reliable measurements are even more difficult owing to the opacity of melts. Assuming that the kinetic energy input is negligible *Eq.(2.26)* leads to :

$$K r^2 v^3 = \rho_l g Q L \quad (2.27.a)$$

where, the rate of buoyancy input  $W_B = \rho_l g Q L$ . Hence, for a given set of operating conditions *Eq.(2.26)* can be conveniently written as:

$$r \propto v^{1/5} \quad (2.27)$$

Consequently, any uncertainty in the measured plume radius ' $r$ ' is likely to effect the estimated flow velocity ' $v$ ' more pronouncedly. As a consequence of these, an alternative, physically more plausible formulation is called for the estimation of the mean upward flow and the associated rate of melting in the two phase plume region of the gas stirred systems.

Since the specific potential energy input rate of the experimental configuration of

Taniguchi et.al. is similar to those considered by Mazumdar and co-workers [28], consequently, the ' plume model ' derived earlier [28] for ladle metallurgy steelmaking operations can be conveniently extrapolated to their experimental study. Equating the potential energy input rate to a fraction of the rate of turbulence energy dissipation in the gas stirred systems, Mazumdar et.al. [28] demonstrated that the rise velocity of the up-welling gas-liquid plume mixture can be estimated in terms of the operating variables  $L$ ,  $R$  and  $Q$  according to,

$$U_p = 4.4 Q^{0.33} L^{0.25} R^{-0.25} \quad (2.28)$$

in which,  $L$  is the depth of the liquid,  $R$  is the vessel radius and  $Q$  is the gas flow rate corrected to the mean height and the temperature of the liquid. Details of the derivation can be found elsewhere [21], and is therefore not reproduced here. The adequacy of the ' Plume Model' has already been demonstrated independently by several researchers [29,30,31]. Consequently, it is proposed that the mean upward velocity in the two phase plume region be estimated via Eq.(2.28) in lieu of Eq.(2.26), and applied in conjunction with an appropriate heat transfer correlation for estimating the melting rates of solids in the two phase plume region. Thus  $U_p$ , the plume rise velocity estimated *a-priori* via Eq.(2.24) in terms of the key operating parameters (viz.,  $L$ ,  $R$  and  $Q$ ) can now be embodied in an appropriate heat transfer correlation to deduce the heat transfer coefficient (viz., Eq.(2.24)) in the two phase plume region of the gas stirred system.

Thus considering,  $Re_D = (\rho_l U_p D) / \mu_l$ , predictions on melting rates were made for the experimental observations of Taniguchi et.al. [14,15] were quantified on the basis of Eq.(2.24). As mentioned already, the experimental configurations and the values of relevant thermophysical properties together with the present estimates of plume velocities as a function of the gas flow rates applied have been summarised in Table-2.2. In Fig.(2.9) a log-log plot between the experimental Nusselt number [14,15],  $(Nu-2) / \{ Pr^{0.4} (\mu_b / \mu_o)^{0.25} \}$ , and the corresponding estimates of the Reynolds number,  $Re_D (= (\rho_l U_p D) / \mu_l)$  is shown together with the theoretical line for Eq.(2.24). There very reasonable agreement between estimates and the experimental measurements is readily apparent.

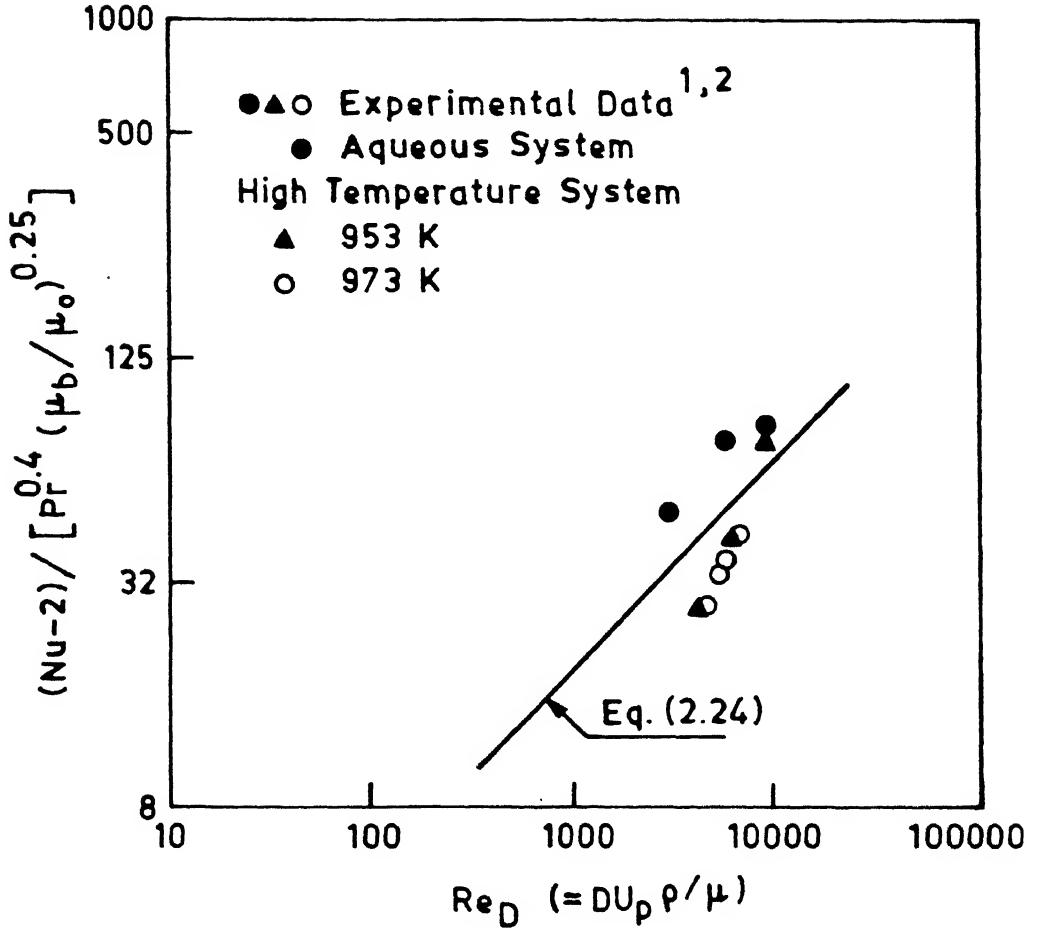


Fig.(2.9) : A log-log plot between the experimental Nusselt number [14,15],  $(Nu-2)/\{Pr^{0.4} (\mu_b/\mu_0)^{0.25}\}$  and the present estimates of the Reynolds number,  $Re_D$ , vis a vis the line for Eq.(2.24). ( deduced through the macroscopic modelling Eq.(2.28).



Alternatively to *Eq.(2.24)*, the following heat transfer correlation has also been applied to assess the adequacy of the macroscopic formulation further e.g.,

$$Nu - 2 = [ 0.06 Re_D^{(0.5 + 0.17Tu)} Pr^{0.33} ] \quad (2.29)$$

It is important to note here that in an earlier study Iguchi et.al.[20] have demonstrated that *Eq.(2.29)* holds good for gas stirred system and produces estimates of Nusselt number that were in reasonable agreement with their experimental observations as well as the ones reported in literature. In the plume region of a gas stirred system, the intensity of turbulence is known to be fairly large [24] in comparison to those in the bulk phase region. To this end, the experimental work of Sheng and Irons [24] suggests that within the plume of an aqueous gas stirred system, the intensity of turbulence can be ascribed with reasonable certainty to a characteristic value of around 0.5. Based in such information *Eq.(2.29)* can be simplified for the two phase region as:

$$Nu - 2 = 0.06 Re^{0.55} Pr^{0.33} \quad (2.30)$$

On the basis of *Eq.(2.30)* the Nusselt number and / or the heat transfer coefficients were re-estimated in terms of the operating variables. In *Fig.(2.10)*, a log-log plot between the experimental Nusselt number [14,15],  $(Nu-2)/ Pr^{0.33}$  and the estimated Reynolds number,  $Re_D (= (\rho_l U_p D) / \mu_l)$ , is shown together with the theoretical line for *Eq.(2.30)*. There, reasonable agreement between experimental measurements and present estimates is at once apparent. Results presented in *Fig.(2.10)* evidently indicate that the present formulation is indeed as effective as the differential model predictions [20] for estimating the melting rates in the two phase plume region of the gas stirred baths.

As a final point the present study also indicates that the *Eqs (2.24)* and *(2.29)* are equally effective for predicting of melting rates in the gas stirred bath. However, *Eq.(2.29)* embodies an additional dimensionless group i.e., the intensity of turbulence,  $Tu$ , in addition to the object Reynolds number,  $Re_D$ . The distribution of this parameter should be known *a-priori* so as to estimate the heat transfer coefficient via. *Eq.(2.29)* particularly, when the addition is melting

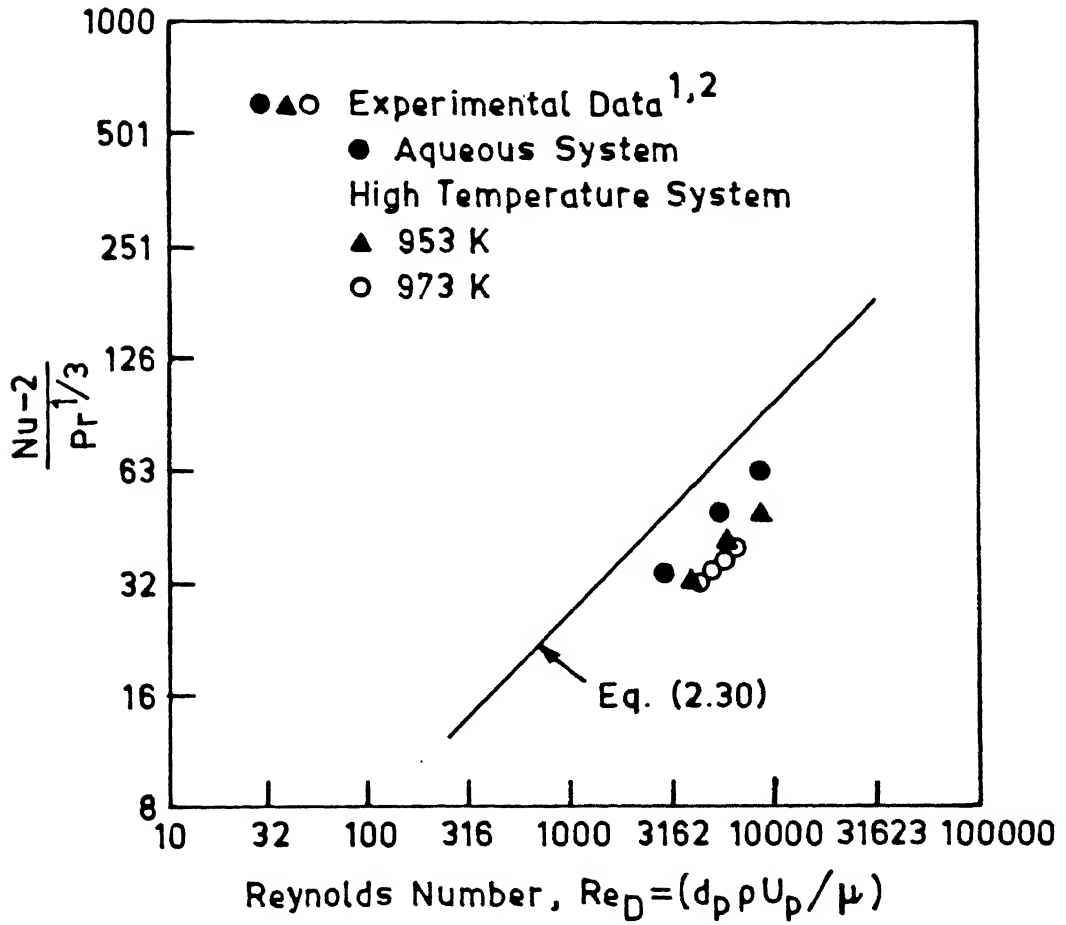


Fig.(2.10) : A log-log plot between the experimental Nusselt number [14,15],  $(Nu-2)/Pr^{0.33}$  and the present estimates of the Reynolds number,  $Re_D$ , vis a vis the line for Eq.(2.30). (deduced through the macroscopic modelling Eq.(2.28).

outside the plume in the bulk liquid. Analysis of melting under such conditions will therefore warrant detailed computation of the turbulent flow field through numerical calculation. Nevertheless, it is well known that while the flow variables ( $u$ ,  $v$  etc.) in such systems can be estimated with reasonable certainty, considerable uncertainty still remains as far as prediction of various turbulence parameters ( $\mu_e$ ,  $k$  etc.) are concerned. Evidently, therefore some uncertainty is likely to be associated with the numerical estimates of  $Tu$ , the intensity of turbulence. In view of such limitations associated with the hydrodynamic modelling of gas stirred systems, it appears that *Eq.(2.24)* is likely to provide somewhat superior and more reliable estimates of melting rates in gas bubble driven systems, than *Eq.(2.29)*.

## CHAPTER - 3

### DEVELOPMENT OF A STEADY STATE, THREE DIMENSIONAL TURBULENT FLOW CALCULATION PROCEDURE

In the previous chapter, the adequacy of the two phase computational procedure developed by Mazumdar and Guthrie [18] was examined. It was demonstrated implicitly that their model produces estimates of flow and turbulence parameters in the gas stirred system that are in reasonable agreement with the experimental observations reported in the literature. In this chapter the salient features of upgradation of the *CFD* package [18] to steady state, three dimensional, two phase, configuration is presented. It needs to be mentioned here that the 3-D calculation procedure has been developed for cartesian coordinate system, while the calculation procedure of Mazumdar and Guthrie has the capability of carrying out computations in both cartesian and polar coordinate system.

#### 3.1 Introduction

The degree of complexity required to mathematically model different metallurgical processes varies from one to another. While, operations like axisymmetric gas injection, axisymmetric pouring and drainage, can be effectively modelled using a two dimensional turbulent flow model, others, like melt flow in tundishes or in a *R-H* degasser require a three dimensional turbulent flow model for effective simulation. Needless to mention that transport processes in practically all metallurgical operations can be successfully modelled using transient, two phase, three dimensional models. To this end, several software packages are currently commercially available. Some of the popularly used software packages have been listed in *Table-3.1*.

Table-3.1: Popularly used software packages to study transport phenomena [2].

Name	Application	Technique
<i>PHOENICS</i>	fluid dynamics, Heat Transfer, Chemical Reaction	finite volume
<i>TEACH - T</i>	fluid dynamics	finite volume
<i>FLOW 3-D</i>	fluid dynamics	finite difference
<i>FLUENT</i>	fluid dynamics, Heat Transfer	finite difference
<i>NECTON</i>	fluid dynamics, Heat Transfer	finite element
<i>NISA</i>	fluid dynamics, Heat Transfer	finite difference

However, the key problem lies in the definition of the boundary conditions and the ability to interpret the results in an intelligent manner. Hence, many researchers prefer custom built models from the first principles with consideration of elementary control volumes. Indeed, this later philosophy has been applied in the present investigation to develop the steady, two phase, three dimensional computational procedure.

Thus, the present chapter deals with the development and validation of a steady state, three dimensional, two phase, turbulent flow model in cartesian coordinate system. The computer code developed has been subsequently used to study the melt flow behaviour in rectangular shaped steelmaking tundish system with no flow control devices ( *Chapter-4*).

## 3.2 Governing Equations

### 3.2.1 The liquid phase flow equations

In terms of cartesian co-ordinate system  $(x,y,z)$  , the governing flow equations ( for the liquid phase ) under turbulent flow conditions can be represented as:

*Equation of continuity :*

$$\frac{\partial}{\partial x}(\alpha_l \rho u) + \frac{\partial}{\partial y}(\alpha_l \rho v) + \frac{\partial}{\partial z}(\alpha_l \rho w) = 0 \quad (3.1)$$

*Equation of motion in x direction :*

$$\frac{\partial}{\partial x}(\alpha_l \rho uu) + \frac{\partial}{\partial y}(\alpha_l \rho uv) + \frac{\partial}{\partial z}(\alpha_l \rho uw) = -\alpha_l \frac{\partial p}{\partial x} + \frac{\partial}{\partial x}(\alpha_l \mu_e \frac{\partial u}{\partial x}) + \frac{\partial}{\partial y}(\alpha_l \mu_e \frac{\partial u}{\partial y}) + \frac{\partial}{\partial z}(\alpha_l \mu_e \frac{\partial u}{\partial z}) + S_u \quad (3.2.a)$$

*in which,*

$$S_u = \frac{\partial}{\partial x}(\alpha_l \mu_e \frac{\partial u}{\partial x}) + \frac{\partial}{\partial y}(\alpha_l \mu_e \frac{\partial v}{\partial x}) + \frac{\partial}{\partial z}(\alpha_l \mu_e \frac{\partial w}{\partial x}) + F_x \quad (3.2.b)$$

*Equation of motion in the y direction :*

$$\frac{\partial}{\partial x}(\alpha_l \rho uv) + \frac{\partial}{\partial y}(\alpha_l \rho vv) + \frac{\partial}{\partial z}(\alpha_l \rho vw) = -\alpha_l \frac{\partial p}{\partial y} + \frac{\partial}{\partial x}(\alpha_l \mu_e \frac{\partial v}{\partial x}) + \frac{\partial}{\partial y}(\alpha_l \mu_e \frac{\partial v}{\partial y}) + \frac{\partial}{\partial z}(\alpha_l \mu_e \frac{\partial v}{\partial z}) + S_v \quad (3.3.a)$$

*in which,*

$$S_v = \frac{\partial}{\partial x}(\alpha_l \mu_e \frac{\partial u}{\partial y}) + \frac{\partial}{\partial y}(\alpha_l \mu_e \frac{\partial v}{\partial y}) + \frac{\partial}{\partial z}(\alpha_l \mu_e \frac{\partial w}{\partial y}) + F_y \quad (3.3.b)$$

*Equation of motion in the z direction :*

$$\frac{\partial}{\partial x}(\alpha_l \rho uw) + \frac{\partial}{\partial y}(\alpha_l \rho vw) + \frac{\partial}{\partial z}(\alpha_l \rho ww) = -\alpha_l \frac{\partial p}{\partial z} + \frac{\partial}{\partial x}(\alpha_l \mu_e \frac{\partial w}{\partial x}) + \frac{\partial}{\partial y}(\alpha_l \mu_e \frac{\partial w}{\partial y}) + \frac{\partial}{\partial z}(\alpha_l \mu_e \frac{\partial w}{\partial z}) + S_w \quad (3.4.a)$$

*in which,*

$$S_v = \frac{\partial}{\partial x}(\alpha_l \mu_e \frac{\partial u}{\partial z}) + \frac{\partial}{\partial y}(\alpha_l \mu_e \frac{\partial v}{\partial z}) + \frac{\partial}{\partial z}(\alpha_l \mu_e \frac{\partial w}{\partial z}) + F_z \quad (3.4.b)$$

*Equations (3.2) through (3.4) are the well known Navier-Stokes equations. In these  $u, v, w$  and  $p$  (gauge with reference to local hydrostatic pressure) are respectively the time averaged velocity components and pressure.  $\alpha_l$  is the volume fraction of liquid and  $F$ 's are the various body forces acting on the fluid which may include buoyancy, drag etc. Finally,  $\mu_e$ , appearing in *Eqs.*(3.2) through (3.4) is the effective viscosity and is derived from an appropriate turbulence model.*

The values of  $\alpha_l$  in *Eqs* (3.2) through (3.4) can be obtained from the solution of bubble trajectory equations already outlined in *Chapter-2*. Assuming, that there is no bubble motion in the  $z$ -direction (the lateral direction) the bubble trajectory equations can be used in its original two dimensional form, outlined in the previous chapter. Consequently, the drag forces generated by the bubble motion will exist only in the  $x$  and  $y$  directions i.e.  $F_z$  will be equal to zero. Subtle modifications are warranted such as, the relative velocity vector between the bubbles and the liquid phase will now be required to be calculated from the three velocity components in the  $x, y$  and the  $z$  directions. Moreover, the two dimensional arrays of bubble motion need to be converted into the corresponding three dimensional arrays. Alternatively, an additional force balance equation can also be incorporated for the  $z$  coordinate axis and thus, components of body forces i.e.,  $F_x, F_y, F_z$  in the Navier Stokes equations can be calculated by solving the three ordinary differential equations governing the motion of the bubble in the three dimensional vector. All calculations reported in this and subsequent chapter were derived assuming  $\alpha_l=1.0$  (single phase calculation).

### 3.2.2 The turbulence model

In the present work the popular two equation,  $k-\epsilon$  Model of Launder and Spalding [21] has been used for the estimation of turbulence parameters. The model incorporates an

equation for the conservation of turbulent kinetic energy,  $k \{ = 1/2(u'^2 + v'^2 + w'^2) \}$  and its dissipation rate,  $\epsilon \{ = -dk/dt \}$ . The  $k$  and  $\epsilon$  transport equations in terms of cartesian co-ordinate system can be expressed as following:

*Conservation equation for the turbulence kinetic energy,  $k$ :*

$$\frac{\partial}{\partial x}(\rho_l \alpha_l uk) + \frac{\partial}{\partial y}(\rho_l \alpha_l vk) + \frac{\partial}{\partial z}(\rho_l \alpha_l wk) = \frac{\partial}{\partial x}(\alpha_l \frac{\mu_e}{\sigma_k} \frac{\partial k}{\partial x}) + \frac{\partial}{\partial y}(\alpha_l \frac{\mu_e}{\sigma_k} \frac{\partial k}{\partial y}) + \frac{\partial}{\partial z}(\alpha_l \frac{\mu_e}{\sigma_k} \frac{\partial k}{\partial z}) + S_k \quad (3.5.a)$$

*in which,*

$$S_k = \alpha_l (G_k - \rho \epsilon) \quad (3.5.b)$$

*Conservation equation for the dissipation rate of turbulence kinetic energy,  $\epsilon$ :*

$$\frac{\partial}{\partial x}(\rho_l \alpha_l u\epsilon) + \frac{\partial}{\partial y}(\rho_l \alpha_l v\epsilon) + \frac{\partial}{\partial z}(\rho_l \alpha_l w\epsilon) = \frac{\partial}{\partial x}(\alpha_l \frac{\mu_e}{\sigma_\epsilon} \frac{\partial \epsilon}{\partial x}) + \frac{\partial}{\partial y}(\alpha_l \frac{\mu_e}{\sigma_\epsilon} \frac{\partial \epsilon}{\partial y}) + \frac{\partial}{\partial z}(\alpha_l \frac{\mu_e}{\sigma_\epsilon} \frac{\partial \epsilon}{\partial z}) + S_\epsilon \quad (3.6.a)$$

*in which,*

$$S_\epsilon = \alpha_l \left[ \frac{C_1 \epsilon G_k - C_2 \rho \epsilon^2}{k} \right] \quad (3.6.b)$$

$G_k$  appearing in Eqs.(3.5) and (3.6) is the volumetric rate of turbulence generation and for a three dimensional cartesian co-ordinate system, can be expressed as:

$$G_k = 2 \mu_T \left[ \left( \frac{\partial u}{\partial x} \right)^2 + \left( \frac{\partial v}{\partial y} \right)^2 + \left( \frac{\partial w}{\partial z} \right)^2 \right] + \mu_T \left[ \left( \frac{\partial u}{\partial y} + \frac{\partial v}{\partial x} \right)^2 + \left( \frac{\partial v}{\partial z} + \frac{\partial w}{\partial y} \right)^2 + \left( \frac{\partial u}{\partial z} + \frac{\partial w}{\partial x} \right)^2 \right] \quad (3.7)$$

The eddy viscosity,  $\mu_e$ , appearing in Eqs(3.2) to (3.4) is defined as:  $\mu_e = \mu_T + \mu_l$ , in which,

$$\mu_T = \frac{C_\mu \rho k^2}{\epsilon} \quad (3.8)$$



The five empirical constants of the  $k-\epsilon$  model viz.,  $C_1$ ,  $C_2$ ,  $C_\mu$ ,  $\sigma_k$  and  $\sigma_\epsilon$  were assigned to their standard values [21]. These have been already summarised in *Table-2.1* (see *Chapter-2*). As seen from the above, flow and turbulence model equations are mutually coupled.

### 3.2.3 The boundary conditions

The boundary conditions are problem dependent and most of the metallurgical systems encountered include a free surface of liquid, symmetry axis (if there is any) and the solid vessel walls. Boundary conditions for velocity components include no slip condition at the boundary walls (zero velocity) while across the free surface, zero shear is assumed to be transmitted. Gradients of all the velocity components at the axis of symmetry are taken as zero. Similarly, the values of  $k$  and  $\epsilon$  at the walls are set at zero. Zero gradient of  $k$  and  $\epsilon$  are applied at the symmetry plane and the free surface. Besides this, known values of the dependent variables are applied at the entry / exit locations depending on the problem.

The near wall regions have two major characteristics that distinguish them from the bulk flow [21,32]:

- i. steep non-linear gradient in the flow properties, and
- ii. levels of Reynolds number are sufficiently low for local isotropy of small scale turbulence to prevail.

Hence, the basic turbulence model becomes inapplicable in these regions and alternate representation must be sought. In the present study wall function procedure [21,32] has been used. The method is based on one-dimensional fluid flow, and assumes that the velocity profile in the near wall region is given by the universal logarithmic wall law which can be represented as :

$$\frac{u}{u_\tau} = \frac{1}{\kappa} \ln(y^+ E) \quad (3.9)$$

where  $u$  is the velocity parallel to the wall and  $u_\tau (= \sqrt{(\tau_w / \rho)})$  is the friction velocity,  $\kappa$  is the van Karmen constant and  $E$  is the roughness parameter typically taken as 9 for hydraulically smooth walls.  $y^+$  is a dimensionless wall distance and is defined as :

$$y^+ = \frac{(y u_\tau \rho)}{\mu} \quad (3.10)$$

where  $y$  is the normal distance from the wall. This law has been applied to a point whose  $y^+$  value is greater than 11.63. This is schematically shown in *Fig.(3.1)* . In the  $y^+$  region specified above the Reynolds stresses are constant and the wall stresses,  $\tau_w$  can be calculated as :

$$\tau_w = \rho C_\mu^{0.5} k \quad (3.11)$$

Further, in this region the convection-diffusion of  $(\underline{u}, \underline{u})$  is negligible. This implies that the rate of production of turbulent kinetic energy  $k$  is equal to its dissipation. Such considerations lead to:

$$\frac{k}{u_\tau^2} = \frac{1}{(\sqrt{C_\mu})} \quad (3.12)$$

This relation is normally used as an boundary condition for  $k$  in the two equation  $k-\epsilon$  model. Similarly the boundary condition for  $\epsilon$  can be expressed as :

$$\epsilon = \frac{u_\tau^3}{\kappa y^+} \quad (3.13)$$

The preceding relationships are to be applied to a near wall node whose  $y^+$  is greater than 11.63.

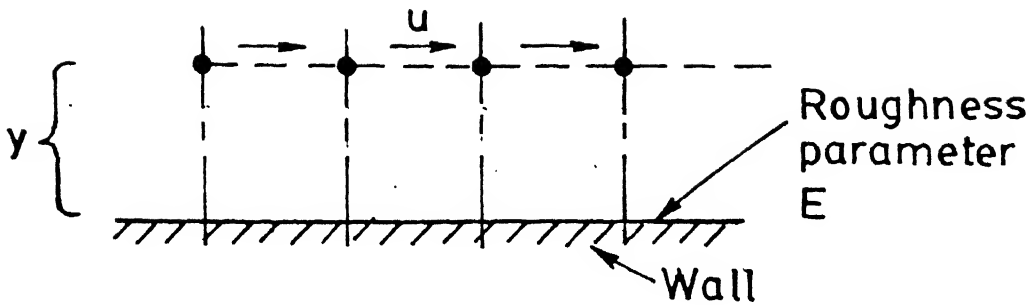


*Fig.(3.1)* : Schematic representation of procedure for the near wall treatment of flow variable and turbulence parameter in the turbulent flow model.

### 3.3 The General Differential Equation

The general structure of the relevant differential equations ( *Eqs.(3.1) to (3.6)*) describing the conservation of mass and momentum and that of the  $k$ -  $\epsilon$  Model of turbulence indicate that all the dependent variables of interest obey a generalised conservation principle. If the general variable is donated by  $\phi$ , the general differential equation can be written as:

$$\text{div} (\rho u \phi) = \text{div} (\tau \text{grad} \phi) + S_{\phi} \quad (3.14)$$

The three terms in the general differential equation, are the convection term, the diffusion term ( $\Gamma$  is the diffusion coefficient ) and the source term,  $S_{\phi}$ . The quantities  $\Gamma$  and  $S$  are specific to a particular meaning of  $\phi$ . The three terms in the general differential equation are the convection term, the diffusion term, and the source term. Depending on the general variable  $\phi$ , an appropriate meaning will have to be given to the diffusion coefficient  $\Gamma$  and the source term  $S$ . For the present set of governing equations this is summarised in *Table-3.2*.

Table-3.2: Definition of  $\Gamma$ ,  $\phi$  and  $S$  of *Eq.(3.14)*.

Conservation of	$\phi$	$\Gamma$	$S_{\phi}$
mass	1	0	0
momentum	$u$	$\mu_e$	Eq.(3.2.a)
	$v$	$\mu_e$	Eq.(3.3.a)
	$w$	$\mu_e$	Eq.(3.4.a)
turbulence kinetic energy	$k$	$\mu_e/\sigma_k$	Eq.(3.5.a)
dissipation rate of k	$\epsilon$	$\mu_e/\sigma_{\epsilon}$	Eq.(3.6.a)

Hence, the procedure of casting any particular differential equation into the general form (Eq.(3.14)) requires manipulation of the equation so that the convection and diffusion terms conform to the standard form. The coefficient of  $grad \phi$  is taken as the expression for  $\Gamma$ , and the remaining terms on the right hand side are collectively defined as the source term,  $S$ . Since, all the equations for mass and momentum transport, and turbulence related phenomena can be thought of a particular case of general equation (Eq.(3.14)) consequently, we need to concern ourselves with the numerical solution of Eq.(3.14) only..

### 3.4 The Grid Arrangement

A portion of the three dimensional grid is shown in Fig.(3.2). For the grid point  $P$ , points  $E$  and  $W$  ( east and west respectively) are its x-direction neighbours, while  $N$  and  $S$  (north and south respectively) are the y-direction neighbours and  $T$  and  $B$  (top and bottom respectively) are the neighbours in the z-direction. The whole flow domain has been divided into a number of such non-overlapping control volumes. Staggered control volumes have been considered for the velocity components  $u$ ,  $v$  and  $w$ . Fig.(3.3) represents the different staggered control volumes at which the discrete values of the variables are located. These values represent the averages over the respective control volumes. Scalar variables i.e.  $p$ ,  $k$ ,  $\mu_e$ ,  $\rho$  and  $\epsilon$  are stored at the grid nodes, while the velocities  $u$ ,  $v$  and  $w$  are stored midway between the grid nodes, between the pressure which drives them. Moreover, the velocities are located where they are needed for the calculation of the convective fluxes of scalar flow variables.

## 3.5 The Numerical Solution Procedure

### 3.5.1 Numerical solution

A control volume based finite difference procedure [26] has been adopted in the present study to solve the governing equations numerically. The solution is initiated by discretizing the domain in a large number of non-overlapping control volumes. The governing equation is integrated around all such control volumes to yield a system of algebraic

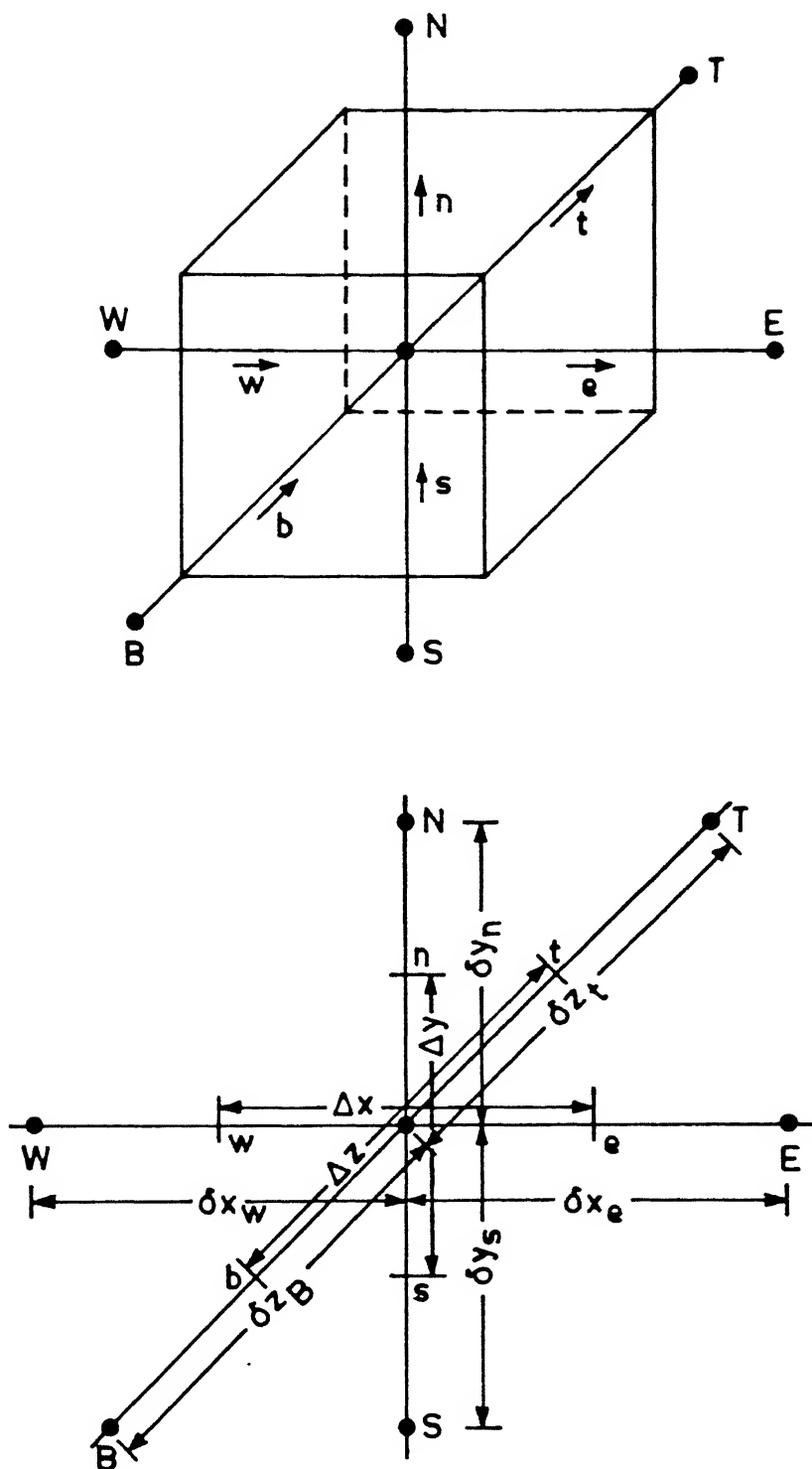
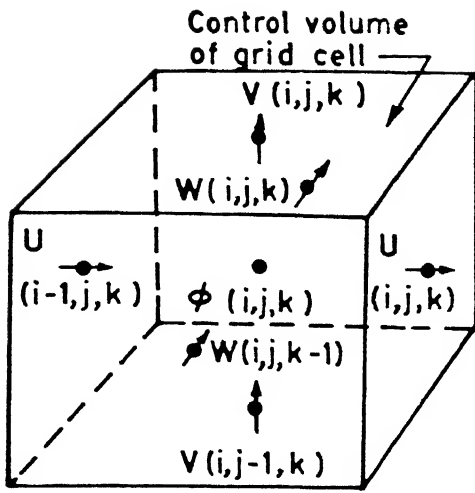
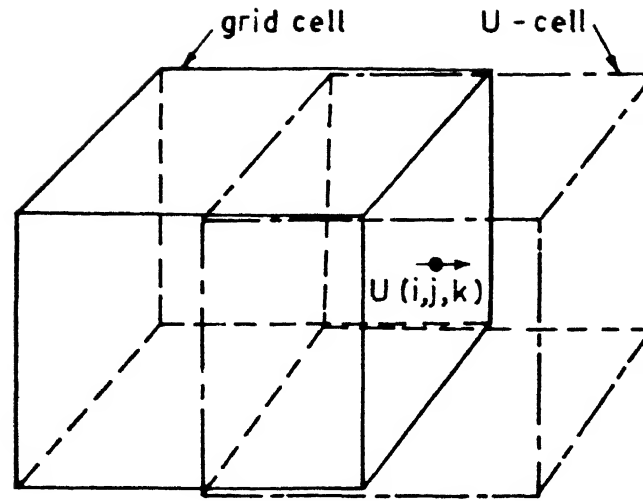


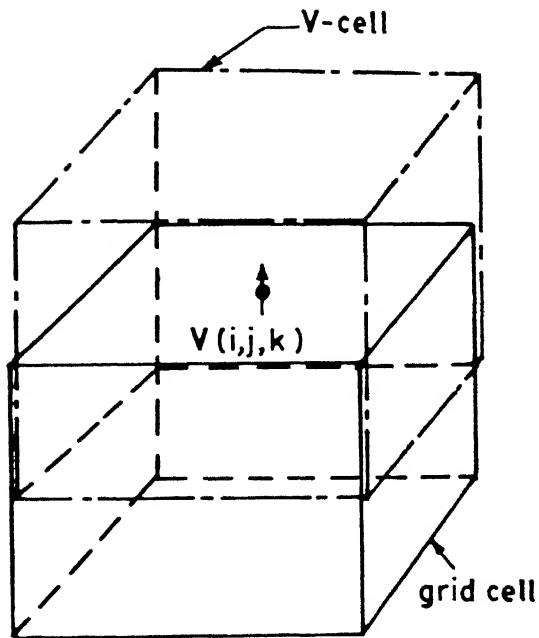
Fig.(3.2) : A typical three dimensional, scalar control volume and various nomenclature used in the cartesian co-ordinate system.



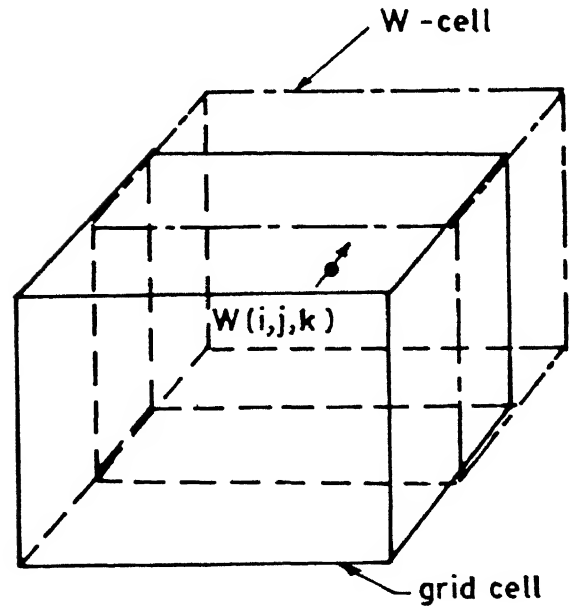
A Grid Cell



A U-Cell



A V-Cell



A W-Cell

Fig.(3.3) : Scalar and staggered control volumes in three dimensional cartesian co-ordinate system.

equations, called the discretization equation [26]. The governing equations (*Eqs.*(3.1) to (3.8)) have both first and second order derivatives. As already mentioned, the first order derivatives are referred to the bulk convection term and the latter as the bulk diffusion term. These terms are then numerically integrated using the concept as applied to a combined convection-diffusion problem incorporating the hybrid differencing scheme as proposed by Patankar [26]. The pressure-velocity interlinkage in *Eqs.*(3.2) to (3.4) have been solved by an implicit finite difference procedure referred to as *SIMPLE* [26] (Semi-Implicit Method for pressure linked equations). A typical discretization equation for the general differential equation (*Eq.*(3.14)) can be written as :

$$A_P \phi_P = A_E \phi_E + A_W \phi_W + A_N \phi_N + A_S \phi_S + A_T \phi_T + A_B \phi_B + S_C \quad (3.15)$$

in which,  $A_P$ , is the centre point coefficient ( see *Fig.*(3.1)) while  $A_E, A_W, A_N, A_S, A_T$  and  $A_B$  are the neighbour point ( three dimensional ) coefficients, representing the combined effect of fluid convection and diffusion. Further,  $S_C$ , represents the constant component of the linearized source term (viz.,  $S = S_c + S_p \phi_p$ ) while the slope has been embodied in the expression of  $A_P$ , the centre point coefficient. The centre point coefficient  $A_P$  is represented as :

$$A_P = A_E + A_W + A_N + A_S + A_T + A_B - S_p \cdot vol \quad (3.16)$$

Thus, in a system of  $n$  internal control volumes,  $n$  number of similar algebraic equations ( viz., *Eq.*(3.15)) are obtained. Further, since the discretization equations are obtained from the same governing equation (*Eq.*(3.14)), the former therefore embodies the same conservation principle as the latter one. This is an important feature of the control volume based formulation as against the routine Taylor series numerical solution procedure.

Prior to the solution of the discretization equations the boundary conditions are also transformed into equivalent numerical form. Boundary conditions are only applied to control volumes located at the domain boundaries. Discretization equations are derived by the same procedure as mentioned. In essence, the incorporation of a boundary condition involves the



modification of  $A_p$  and / or the source terms of the discretization equations of the boundary control volumes (see later).

The resultant set of discretization equations for both boundary and internal nodes were solved using the Tri-Diagonal Matrix Algorithm (*TDMA*) adopting a line by line solution procedure. In this, a particular grid line, say in  $z$ -direction, is chosen and assuming the dependent variable ( $\phi$ ) to be guessed in the  $x$  and  $y$  directions, the problem is reduced to a pseudo-one-dimensional situation and subsequently solved by *TDMA*. This was applied to all the grid lines in one direction and the entire process was repeated for the other two space directions to obtain a tentative solution of the dependent variable,  $\phi$ . This typically constituted one iteration. The total number of iterations required was decided by the convergence criteria adopted, which in the present study was defined according to :

$$\sum \sum \sum [A_p \phi_p - (\sum A_{nb} \phi_{nb} + S_c)] < 10^{-03} \quad (3.17)$$

in which,

$$A_{nb} \phi_{nb} = A_E \phi_E + A_W \phi_W + A_N \phi_N + A_S \phi_S + A_T \phi_T + A_B \phi_B \quad (3.18)$$

The triple sum in *Eq.*(3.17) represents the summation over the entire volume ( i.e., the calculation domain ).

Under relaxation of the dependent variable was employed to achieve / enhance convergence. If  $\phi_p^*$  is the value from the previous iteration of the dependent variable  $\phi_p$  ( $\phi_p$  implies  $\phi$  evaluated at a point  $P$ ) and  $\alpha$  is the under relaxation factor then the change in the value of  $\phi_p$  can be slowed down from iteration to iteration by the following mathematical treatment [26] :

$$\phi_p = \phi_p^* + \alpha \left( \frac{\sum a_{nb} \phi_{nb} + b}{A_p} - \phi_p^* \right) \quad (3.19)$$

Under relaxation factors for the problem chosen were determined by trial and error. Typically,

under relaxation factor of 0.5 was applied to  $u$ ,  $v$  and  $w$  and while a value of 0.7 was used for the turbulence parameters,  $k$  and  $\epsilon$ .

### 3.5.2 The computer program

The concept of casting all governing differential equations to a general differential equation has been outlined in *Section-3.3*. Consequently, a general purpose computer program was developed to solve *Eq.(3.14)*. The computational procedure embodying the numerical solution outlined in the preceding section for the three dimensional model developed is shown in *Fig.(3.4)*. The sequential steps of the computational procedure developed are as follows:

- i. The detailed information regarding the main grid, dimensions of the vessel or the section of the vessel under consideration, the fluid properties, turbulence model constants and the control parameters like convergence criteria and the maximum number of iterations are put in.
- ii. The grid arrangement for the scalar grid and the staggered grid is set up and the initialization of all variables ( $u$ ,  $v$ ,  $w$ ,  $k$ ,  $\rho$ ,  $\mu$  and  $\epsilon$  etc.) is done.
- iii. The  $u$ -momentum,  $v$ -momentum,  $w$ -momentum equations (*Eqs.(3.2) through (3.4)*) are solved sequentially by solving the discretized equations for each of the control volumes by line by line solution technique. This is followed by solving the continuity equation (*Eq.(3.1)*) embodying the *SIMPLE* algorithm [26]. The values of  $u$ ,  $v$  and  $w$  for the calculation domain are corrected for the respective iteration. This is followed by solving the turbulence model equations (*Eqs.(3.5) and (3.6)*) and the values of  $k$  and  $\epsilon$  updated throughout the domain.
- iv. The fluid properties i.e. viscosity ( $\mu_e$ ) are calculated (*Eq.(3.8)*) and updated for the calculation domain.
- v. Steps 3 and 4 are repeated till convergence criteria for all the flow, turbulence and the continuity equation is achieved.
- vi. Before the termination of the program the field distribution of flow and turbulence

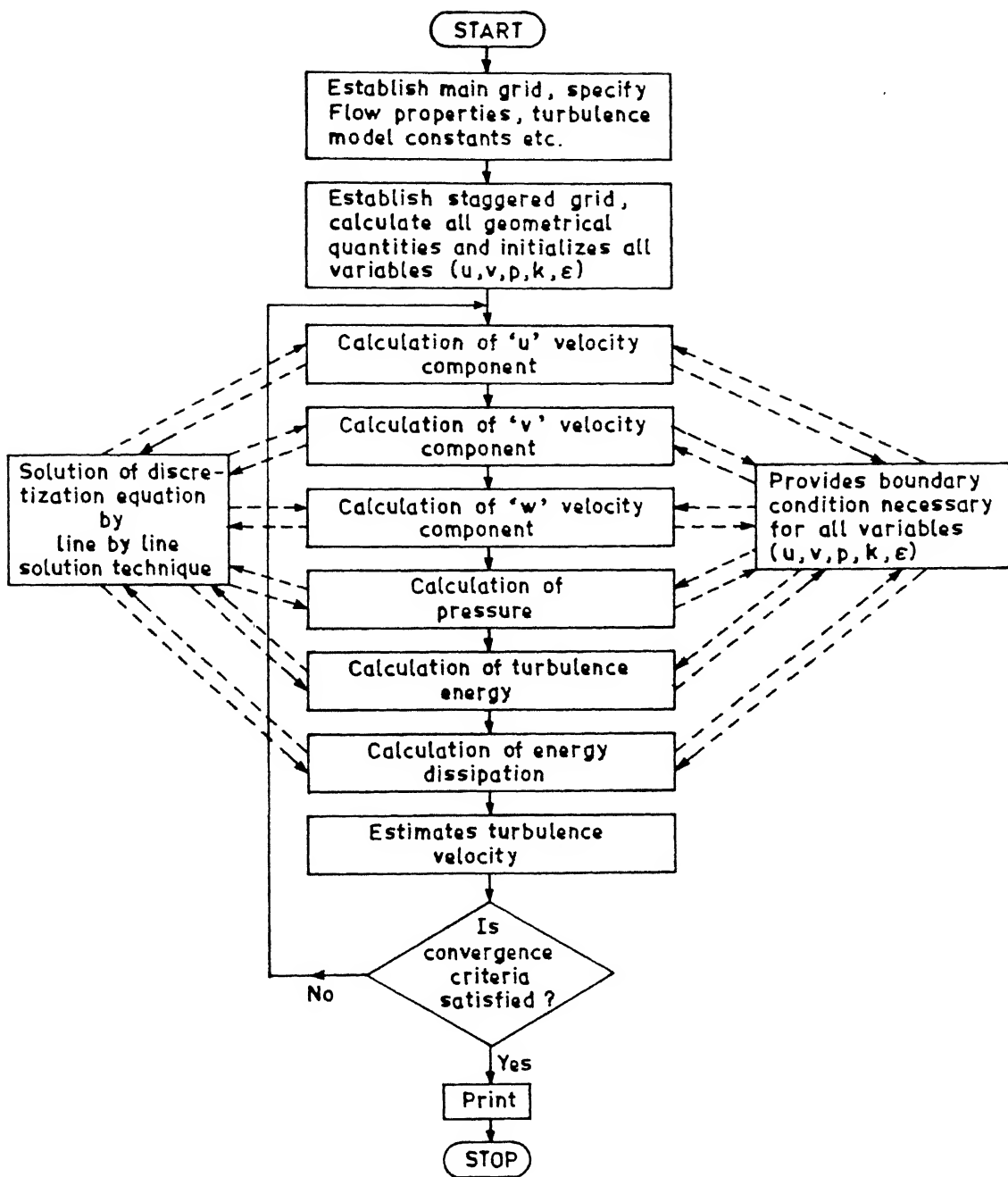


Fig.(3.4) : Flow chart for the three dimensional, turbulent flow calculation procedure.

parameters are printed.

### 3.6 Results and Discussion

The adequacy and appropriateness of the steady state, three dimensional, two phase turbulent flow model was assessed by carrying out some standard three dimensional flow simulation tests. This included flows in enclosed cavity with moving walls (*Figs(3.5.a) and (3.5.b)*), entrance length v. Reynolds number calculation in ducts of square cross-section and so on. These calculations were first carried out under laminar flow condition ( by setting  $\mu = \mu_e$  and modifying  $S_u$  ,  $S_v$  and  $S_w$  appropriately in the flow equations). Subsequently, some of these tests were repeated under turbulent flow conditions ( using the  $k-\epsilon$  model). These are summarised below in detail.

#### 3.6.1 Laminar flow in an enclosed cubic cavity

Steady, laminar , single phase flow in a three dimensional cavity can be conveniently represented by the Navier-Stokes equations presented in *Section- 3.2*. Thus, considering  $\mu_e = \mu$ ,  $\alpha_l = 1.0$  and  $S_u = S_v = S_w = 0$  in the calculation procedure, the computer program was run for a cubic cavity ( $l = 0.5$ ) filled with water ( $\rho_l = 1000 \text{ kg/m}^3$  and  $\mu = 0.001 \text{ kg/m.s}$ ). Two specific problems were solved for this configuration and this included :

##### Problem-1: Flow with one of the cavity walls moving

In this the south wall of the cubic cavity was made to move with a velocity of  $1 \text{ m/s}$  in the positive  $x$  direction (see *Fig.(3.5.a)*). The remaining five solid walls namely the north, east, west, top and bottom walls were considered to be stationary. In order to define the boundary conditions for the given problem exactly, a zero velocity (no slip) condition was applied on the stationary walls. In addition to this, to incorporate the influence of the moving south wall on the fluid flow, the general discretization equation (*Eq.(3.15)*) for the dependent

variable  $u$ , ( the  $x$  component of motion), i.e.,

$$A_p u_p = A_E u_E + A_W u_W + A_N u_N + A_S u_S + A_T u_T + A_B u_B + S_c \quad (3.20)$$

for the boundary control volumes lying in the immediate vicinity of the south wall were modified to :

$$A_p u_p = A_E u_E + A_W u_W + A_N u_N + A_T u_T + A_B u_B + S_c \quad (3.21)$$

where,  $S_c^* = A_s u_s + S_c$  and  $u_s$  is the given velocity of the moving wall( = 1 m/s).

The predicted flow on the central vertical  $XY$  plane (at  $z=0.25$  m)is shown in *Fig.(3.6)*. There as seen, the liquid adjacent to the moving wall accelerates along the direction of motion and turns upwards after hitting the east wall. Continuity requires that the flow along the north wall is in the -ve  $x$  direction and the fluid moves vertically down along the west wall. These form a recirculating loop with the eye of the vortex located at the geometric centre of the cavity. The predicted flow pattern as shown in *Fig.(3.6)* is clearly consistent with that one would expect for such a flow configuration.

#### Problem-2: Flow with two parallel cavity walls moving in the same direction

In this, both north and south walls of the cavity were made to move with a velocity of 0.01 m/s in the positive  $x$  direction (see *Fig.(3.5.b)*). A similar treatment of boundary condition as outlined above was applied to  $u$  control volumes lying in the immediate neighbourhood of both the moving walls. It is important to mention here, that a substantially smaller velocity of moving walls was applied to this problem in contrast to the previous problem, primarily to assess the performance of the model developed for different order of magnitude of input variables.

*Figure (3.7.a)* represents the fluid flow pattern on the central vertical plane at  $z = 0.25$  m . There as seen, the liquid is carried by the moving north and the south walls along with it.

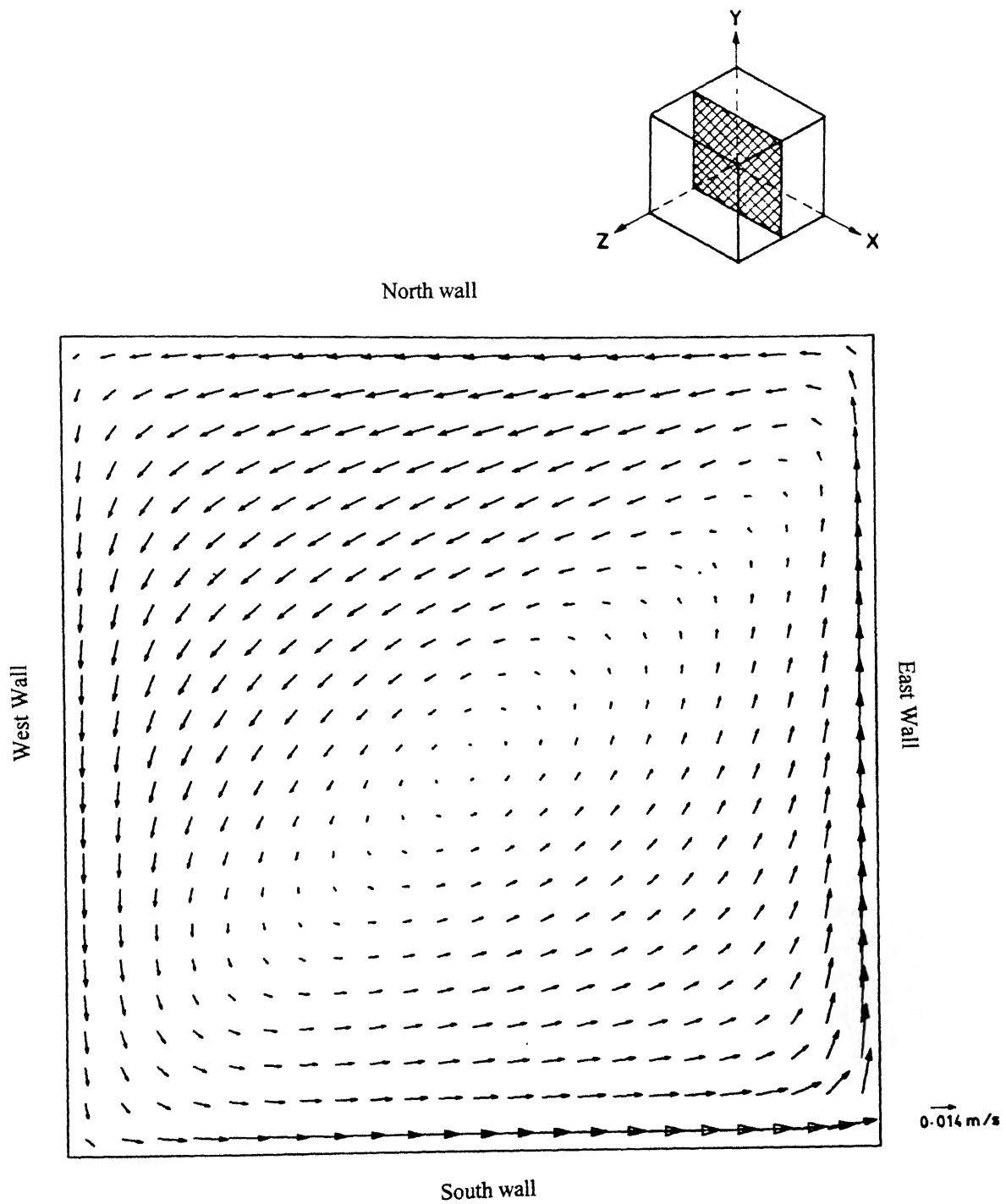


Fig.(3.6) : The predicted flow pattern in the central  $XY$  plane (at  $z=0.25\text{ m}$ ) with one of the cavity walls moving.( *Problem-1*)

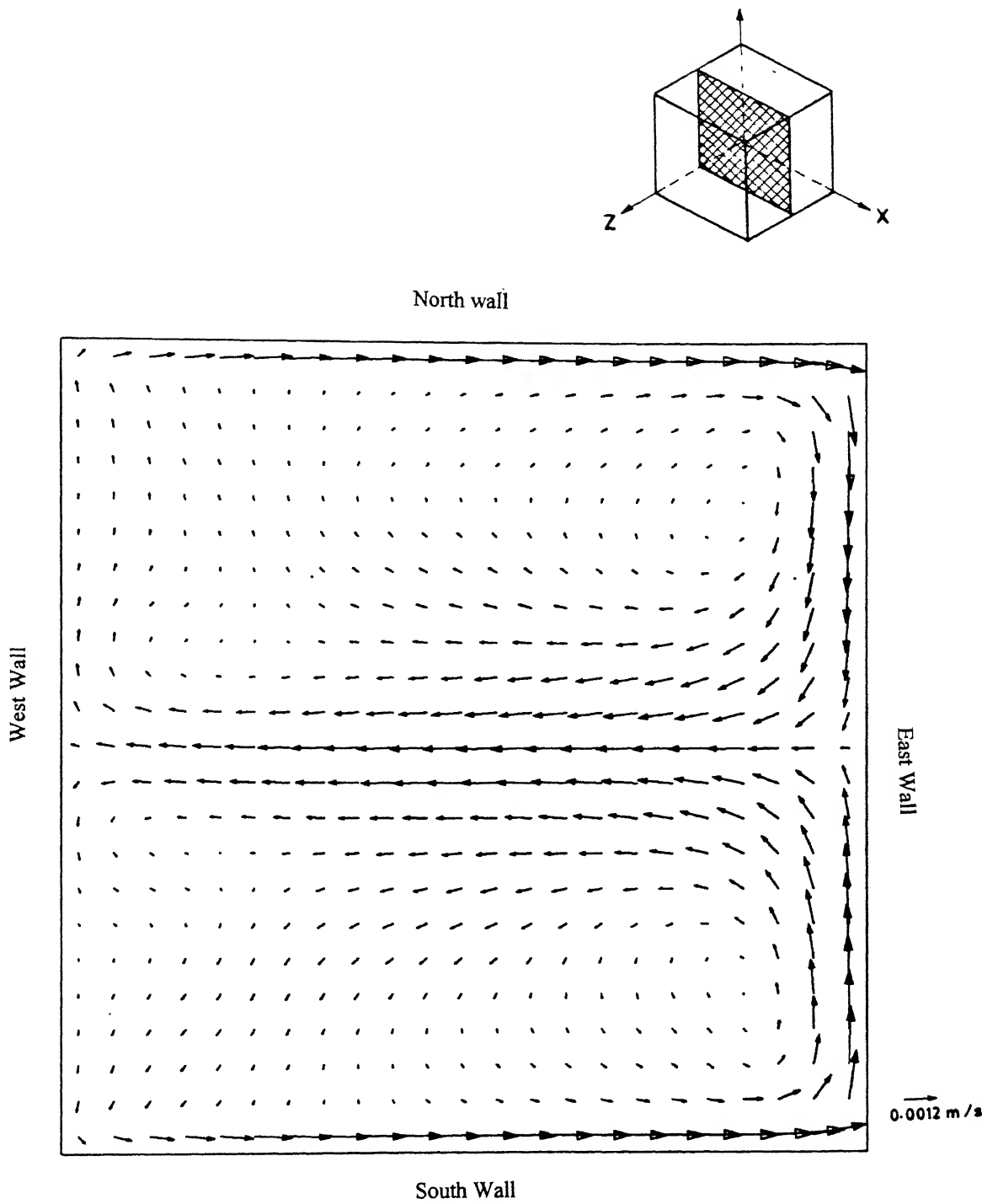


Fig.(3.7.a) : The predicted flow pattern in the central  $XY$  plane (at  $z=0.25\text{ m}$ ) with two parallel cavity walls moving.( *Problem-2*)

After hitting the wall ahead, the fluid flowing along the south wall turns upward whereas, the fluid flowing along the north wall turns downward. These two fluid streams as expected, meet exactly midway on the east wall (e.g., since both the north and the south walls of the cubic cavity are moving with the same velocity of  $0.01 \text{ m/s}$  in the same direction). After hitting each other the rising and falling fluids converge and turn backward at the centreline of the said plane towards the west wall. These as a consequence form two distinct contra-rotating, vortices one above and the other below the centre line. As seen the two loops appear to be exactly the mirror images of each other. Furthermore, the affect of the front and back walls on the fluid flow is practically non-existent as the central vertical  $XY$  plane is somewhat apart and equidistant from the front and the back walls. This essentially produces the two dimensional, symmetrical flow pattern. The affect of these solid walls on the fluid flow becomes noticeable when flow fields in two vertical, but identical planes close to front and back wall are examined. As seen in *Figs(3.7.a)* and *(3.7.b)* the two recirculating loops no longer remain symmetrical. Thus, in the vicinity of the front and back walls one of the loops gets restricted to a small pocket (corner region) in the main direction of flow. Once again the results for these two identical planes are seen to be the mirror images of each other. Predicted flow patterns shown in *Fig.(3.7.a)* through *Fig.(3.7.c)* are clearly consistent with that one would normally anticipate for such flow systems.

### 3.6.2 Entrance length prediction for laminar flow

When a flow enters a duct ( internal flow bounded by walls ) the viscous effects grow and boundary layer on the duct wall develops. The boundary layers eventually meet along the centreline and from this point onwards, the thickness of the boundary layers remain invariant in the streamwise direction. This is shown in *Fig.(3.8.a)* [33]. As seen, there is an entrance region where a nearly inviscid upstream flow converges and enters the tube. Viscous boundary layers grow downstream, retarding the axial flow  $u(x,r)$  at the wall and thereby, accelerating the centre core flow to maintain the incompressible, continuity requirement. At a finite distance from the entrance, the boundary layers merge and the inviscid core disappears. The tube flow then is entirely viscous, and the axial velocity adjusts slightly further until at  $x = L_e$ ,



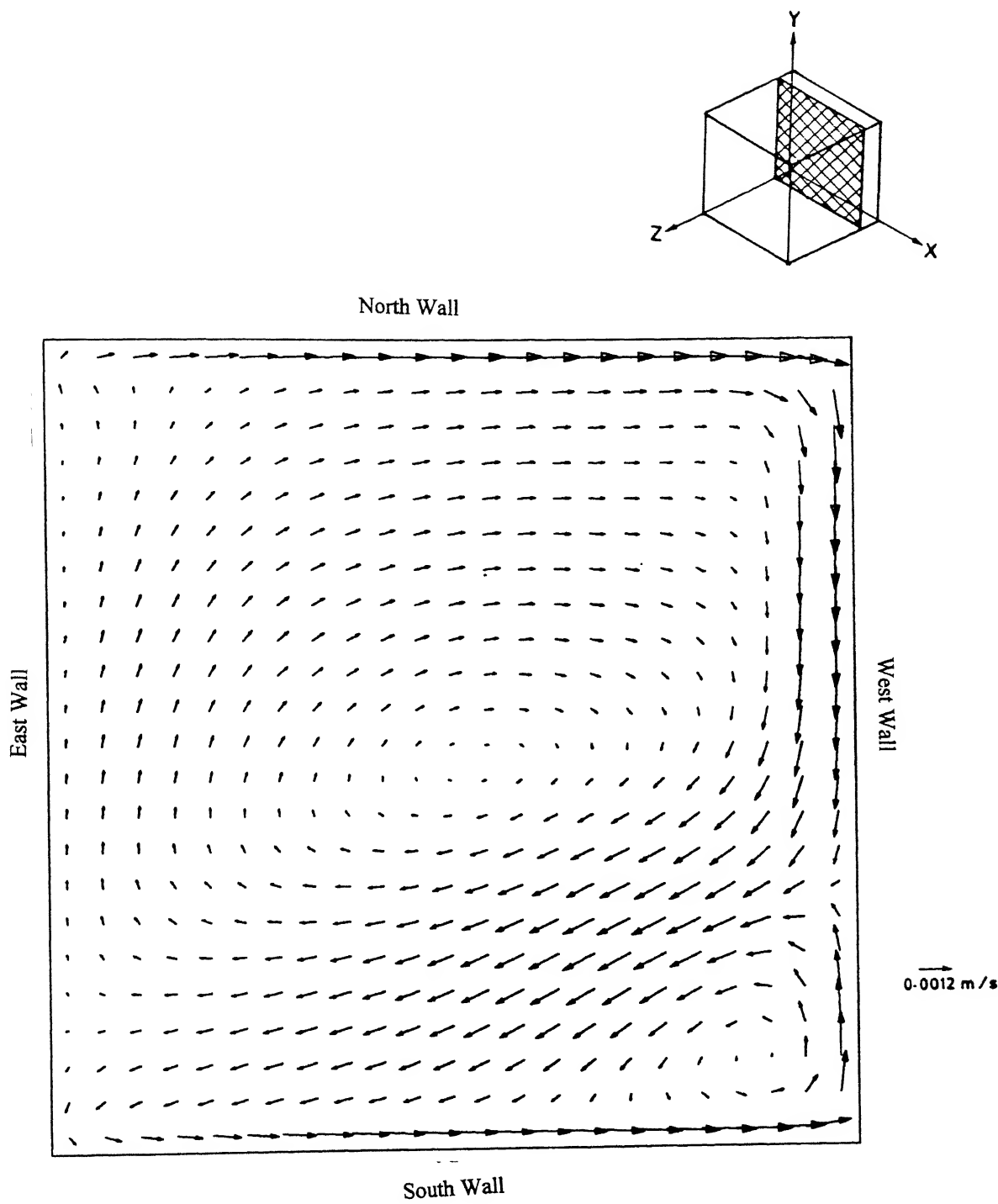
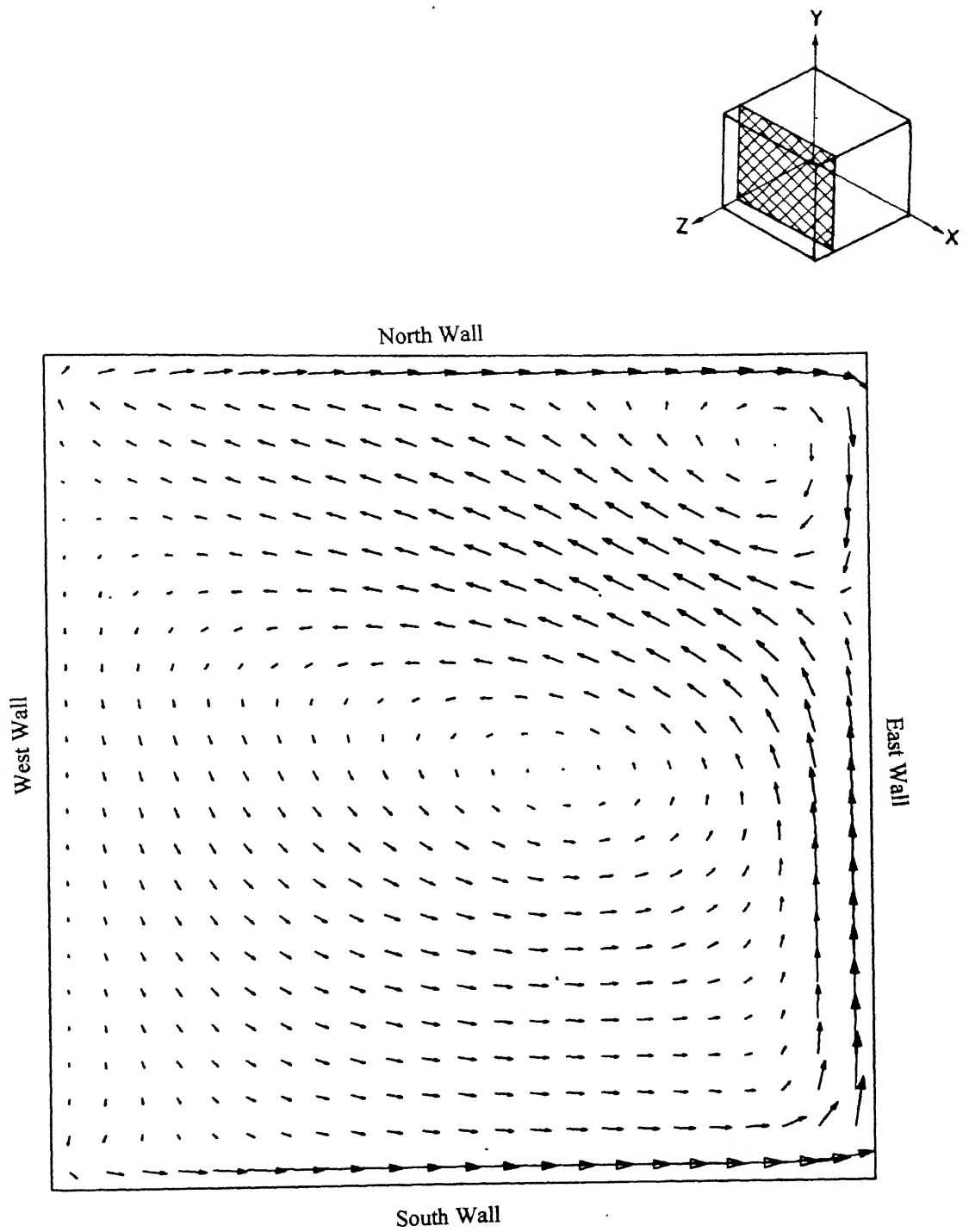


Fig.(3.7.b) : The predicted flow pattern in the  $XY$  plane (at  $z=0.05$  m) with two parallel cavity walls moving. ( *Problem-2* )



*Fig.(3.7.c) : The predicted flow pattern in the  $XY$  plane (at  $z=0.45\text{ m}$ ) with two parallel cavity walls moving. ( *Problem-2* )*

it no longer changes with  $x$  (no acceleration) and is said to be fully developed, i.e.  $u = u(r)$  only. Downstream of  $x = L_e$  the velocity profile as well as the wall shear stress is constant, and the pressure drop varies linearly with  $x$ , for both laminar and turbulent flows (*Fig.(3.8.a)*).

Dimensional analysis [33] shows that the Reynolds number is the only parameter affecting entrance length. Thus,

$$\frac{L_e}{D} = g\left(\frac{\rho V D}{\mu}\right) = g(Re) \quad (3.22)$$

For laminar flow [34], the accepted correlation for entrance length in ducts is :

$$\frac{L_e}{D} = K Re \quad (3.23)$$

Where  $k$  is a constant of proportionality, the value of which, depends on the cross-section of the duct, e.g. for ducts with circular cross section,  $k = 0.06$ . In the present work entrance lengths were calculated for ducts with square cross-section (*Fig.(3.8.b)*) for laminar flow condition.

The dimension of square cross-section ( $D$ ) was varied between  $1 \times 10^{-02}$  to  $3 \times 10^{-02} \text{ m}$  (dimensions in the  $y$  and the  $z$  direction ). Dimension of the duct in the  $x$  direction (the direction of main flow) was defined such that  $x \gg L_e$ . Zero velocity (no slip) boundary conditions were specified for north, south, top and the bottom walls (as already outlined in *Section-3.2.3*). Inflow and outflow boundary treatments were specified at the inlet (west) and outlet (east) planes respectively. *Figure.(3.9)* represents a two dimensional grid arrangement near the entry and the exit planes. Since,  $u$  velocity ( $x$  component of motion) is known at the inlet plane, consequently, a numerical treatment analogous to that presented in *Section-3.6.1* can be applied to accommodate the exact inflow boundary condition into the calculation procedure. For all the grid points  $P$  lying adjacent to the outflow boundary, the coefficient  $A_E$  is set to zero i.e. Peclet number is made sufficiently large ( $P_E \rightarrow \infty, A_E \rightarrow 0$ ) to make the behaviour locally one way in this region. In addition to this, the average exit velocity is

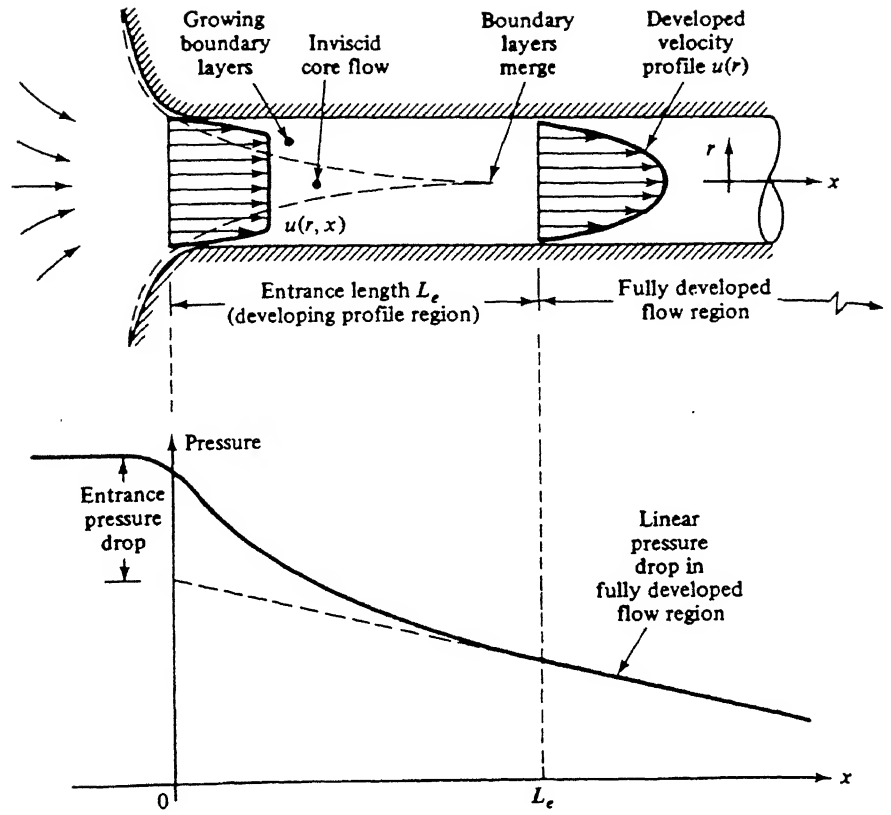
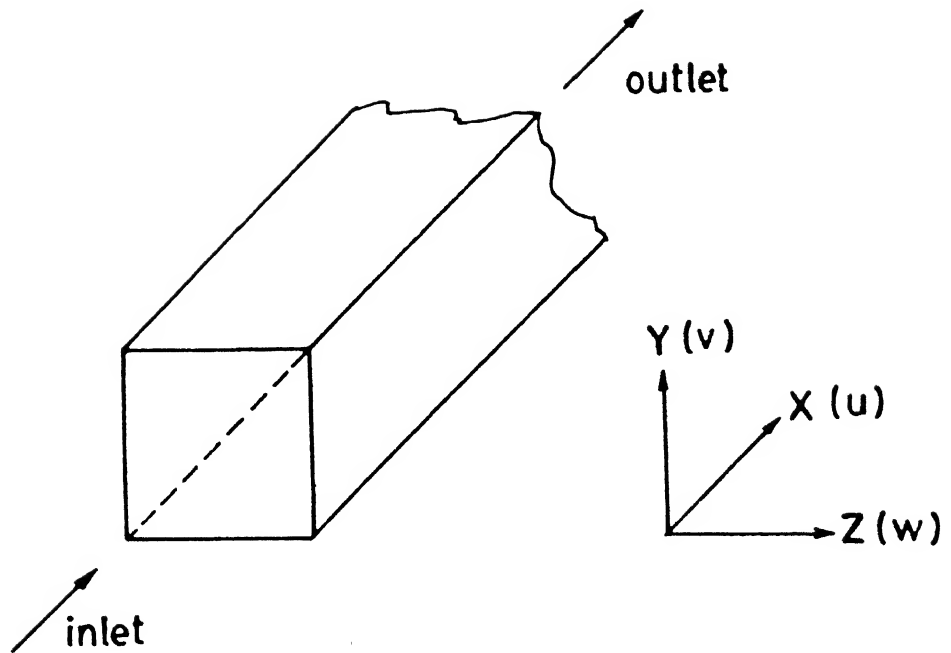
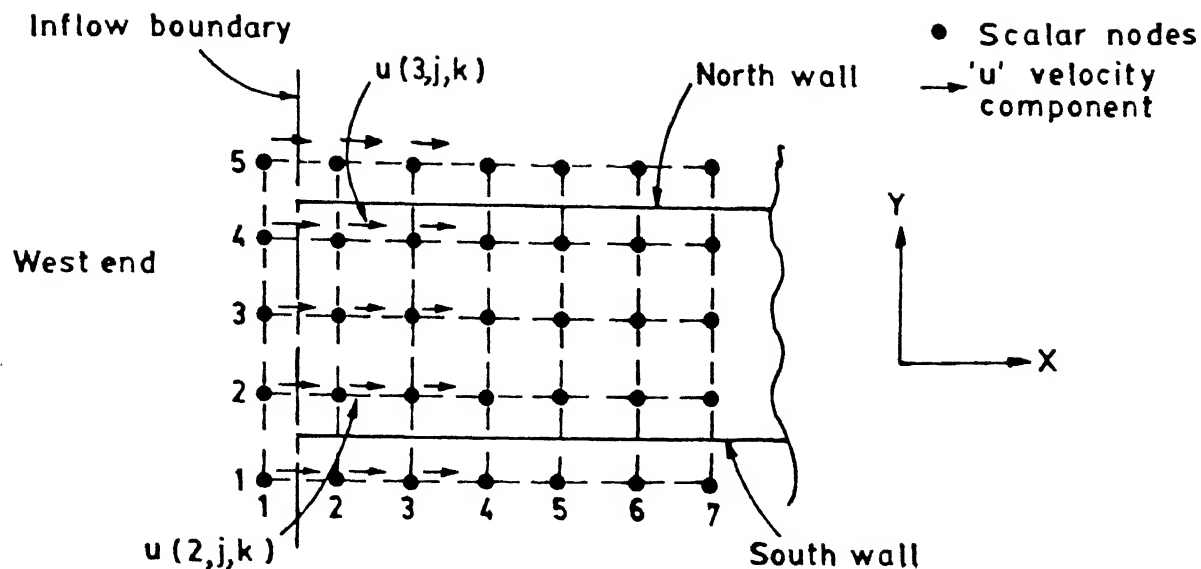


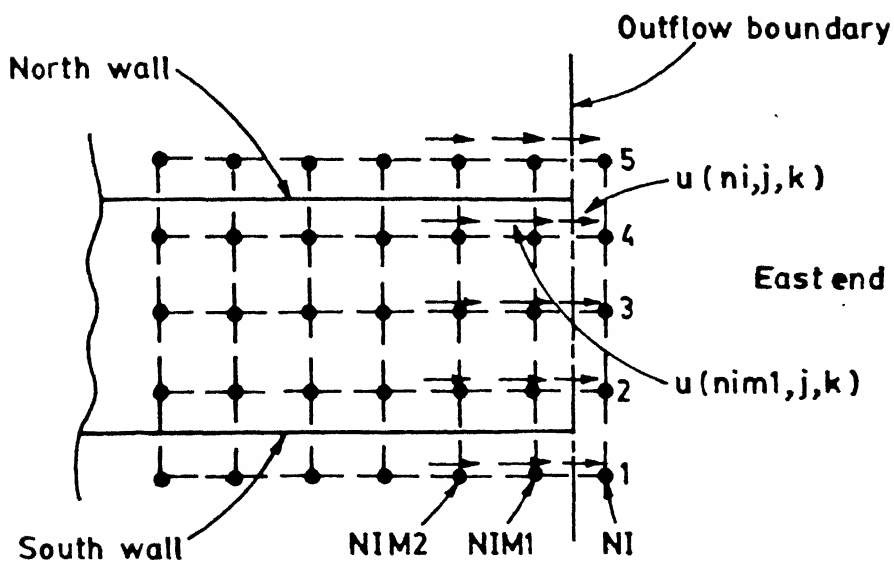
Fig.(3.8.a) : Schematic of the developing velocity profiles and pressure changes in the entrance of a duct flow.



*Fig.(3.8.b)* : Schematic of a duct with a square cross-section and the relevant co-ordinate axis to the problem.



### Inflow boundary treatment



### Outflow boundary treatment

Fig.(3.9) : The procedure adopted for modelling the inflow and outflow boundary condition for the prediction of entrance lengths.

specified at the outflow boundary on the basis of overall continuity which is updated from iteration to iteration by setting  $u(ni,j,k) = u(ni-1,j,k)$ .

Reynolds numbers (e.g.,  $\propto$  inlet velocity ) were varied arbitrarily between 25 to 180 and the flow field within the duct was predicted as a function of inlet Reynolds number. From the predicted results, entrance lengths were estimated graphically by plotting the centreline velocity as a function of  $x$ . Entrance lengths thus estimated were non-dimensionalised (by dividing  $L_e$  by  $D$ ) and plotted against the inlet Reynolds number. This is shown in *Fig.(3.10)*. As shown a straight line was obtained between the two, satisfying the requirement dictated by in *Eq.(3.23)* (e.g.,  $L_e / D \propto Re$  ). This lends further confirmation to the appropriateness of the calculation procedure developed.

### 3.6.3 Turbulent flow in an enclosed cubic cavity

Following the tests under laminar flow situation summarised above, the three dimensional flow model was re-run under the turbulent flow condition for *Problem-1* ( flow with one of the cavity walls moving ). This was carried out by considering the exact form of *Eqs.(3.1)* through (3.4) in conjunction with the  $k-\epsilon$  turbulence model ( *Eqs.(3.5)* through (3.8)) . Standard near wall treatment ( see *Section-3.2.3*) were provided for both flow variables and turbulence parameters. Numerical treatments on boundary conditions, at both moving and stationary walls were identical to those used earlier for *Problem-1* (see *Section-3.6.1*)

It has been observed that the predicted flow in the central  $XY$  plane as well as elsewhere under turbulent flow conditions were qualitatively similar to those obtained under laminar flow conditions. The direction of flow recirculation, position of the vortex were practically identical for both laminar and turbulent flow conditions. To demonstrate the adequacy of the turbulent flow calculation results in *Fig.(3.11)*, horizontal velocity  $u$  was plotted along the vertical central axis of the cubic cavity for a region close to the moving wall, for both laminar flow and turbulent flow predictions. There, as seen, for the region very close to the solid wall, the predicted velocity profiles are nearly identical under both



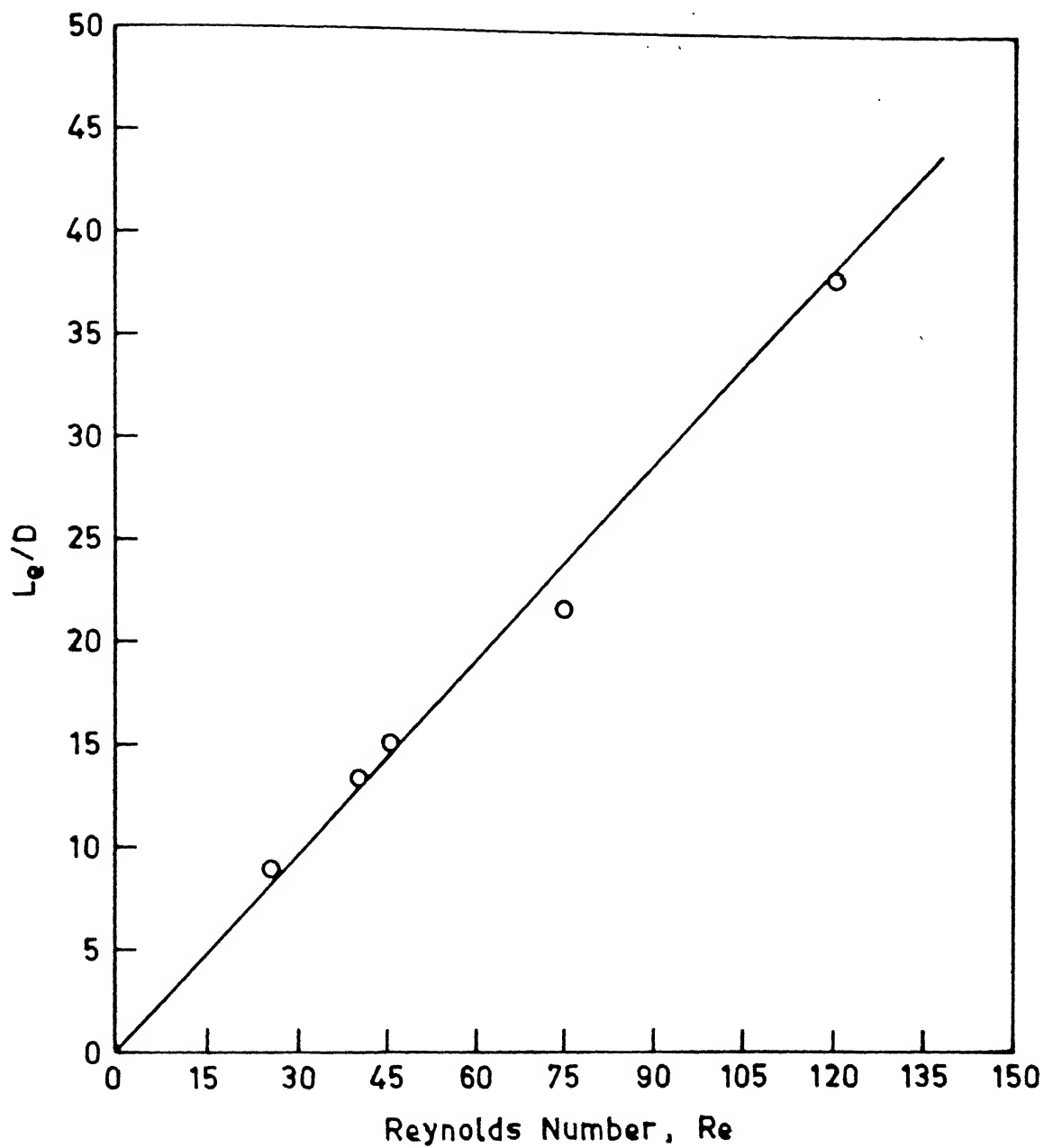


Fig.(3.10) : Predicted entrance lengths ( $L_e/D$ ) as a function of the inlet Reynolds number.



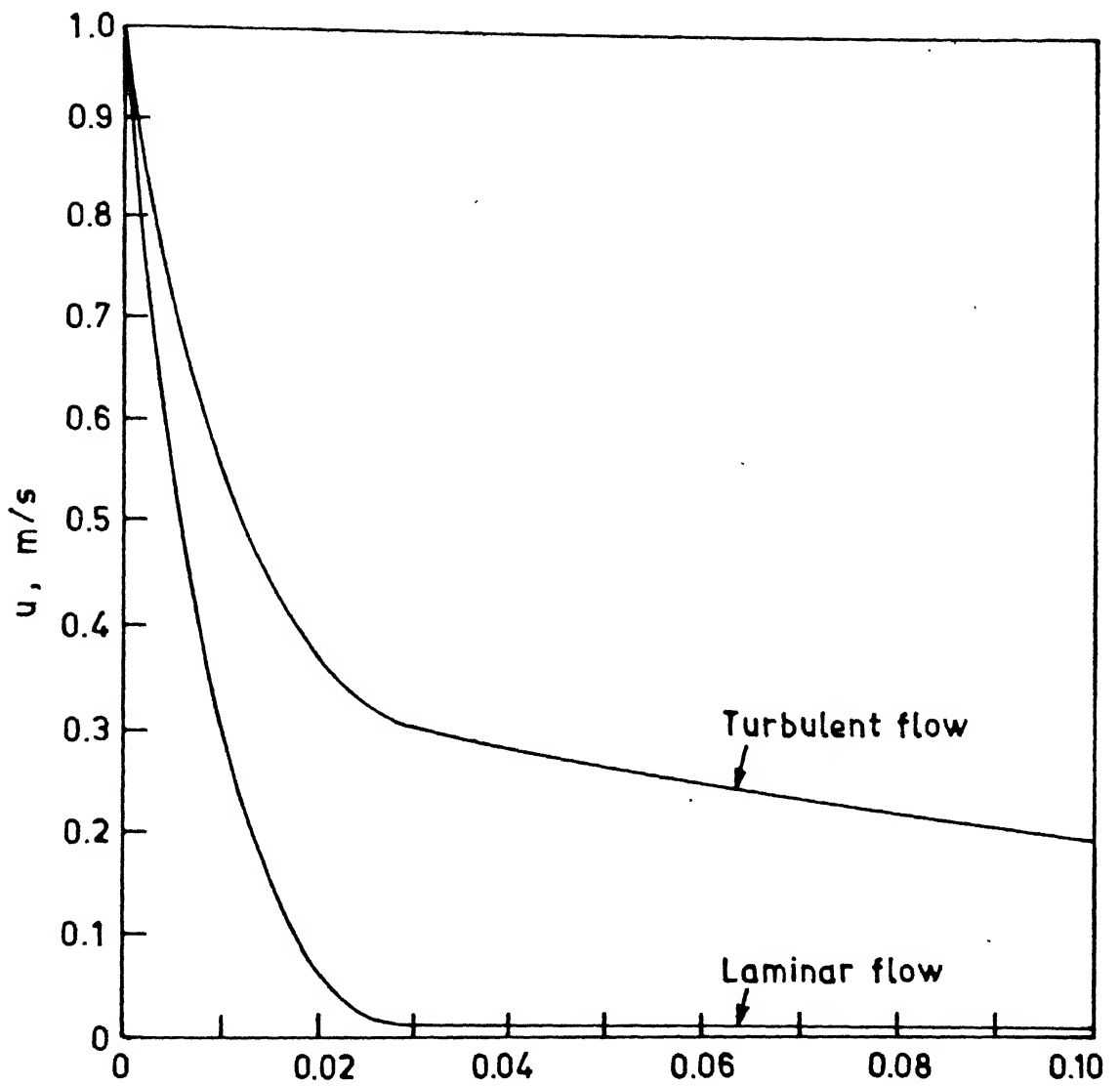


Fig.(3.11) : Predicted variation of horizontal velocity,  $u$  along the vertical central axis ( $x=z=0.25\text{ m}$ ) of cubic cavity, for a region close to the moving wall for laminar and turbulent flows. ( *Problem-1* )

laminar and turbulent flow condition. This is because the shear stresses (at the wall) are expected to be identical for both the cases. This follows, since the shear stress is purely viscous and furthermore, that the viscous stresses are identical for both the situation, consequently, the velocity profiles have identical slopes there. However, in the region next to it, the momentum transfer normal to the moving wall is higher for the turbulent flow because of the presence of additional stresses i.e. Reynolds stresses. This makes the turbulent flow profile less steeper than the corresponding laminar flow situation. The velocity profiles in a nearly similar situation i.e. stationary wall with the bulk liquid moving with a velocity of 1 m/s have been studied [35] and the corresponding results for the near wall region is reproduced in *Fig.(3.12)*. Qualitative agreement between the present estimates and literature is at once evident. This lends further credence to the three dimensional turbulent flow calculation procedure developed in this study and consequently, the model can be now extrapolated with confidence to investigate melt flow behaviour in metallurgical tundish systems.

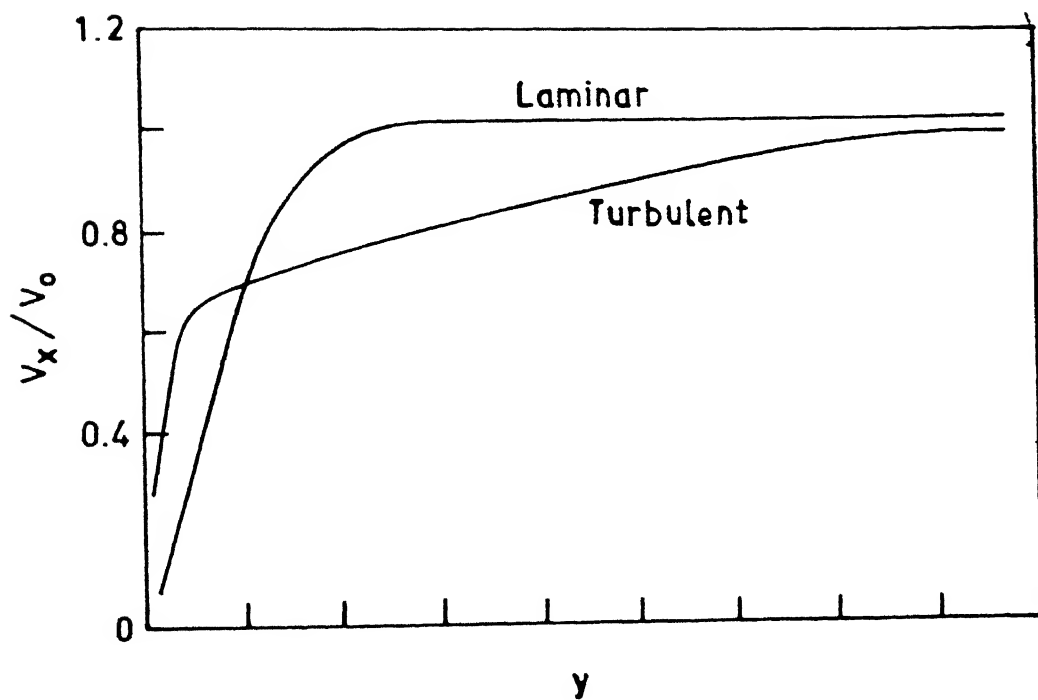


Fig.(3.12) : Velocity profiles in laminar and turbulent flows near a stationary wall [35].(bulk liquid moving with a velocity of 1 m/s)

## CHAPTER - 4

### MODELLING OF FLOW PHENOMENA IN RECTANGULAR SHAPED TUNDISHES

In the previous chapter, the salient features of upgradation of a two dimensional calculation procedure [18] to a steady state, three dimensional, two phase turbulent flow model and its validation with respect to some benchmark solutions were presented. In this chapter the three dimensional turbulent flow model is applied to investigate fluid flow and residence time distribution (*RTD*) in rectangular shaped tundishes with single entry and exit and no flow control devices.

#### 4.1 Introduction

A continuous casting set up essentially consists of three components, the teeming ladle, the tundish and the continuous casting mould. The tundish is the intermediate vessel between the ladle and the mould which functions as a distributor and a buffer vessel and helps maintain a relatively uniform flow as the teeming ladle is being emptied and replaced by a new one. *Figure.(4.1)* shows a schematic of the continuous casting process. Over the years the quality requirements of the final steel product have become very stringent and the tundish offers the last opportunity for the removal and modification of impurities and the adjustment of trim chemical composition by micro-alloying. With the emphasis on the novel casting methods like thin slab and strip casting in a single step, the role of tundish has become even more critical.

The performance of a tundish is very closely related to the nature of steel flow i.e. a well mixed flow would be more suitable for dissolution and alloying where as a plug flow is more

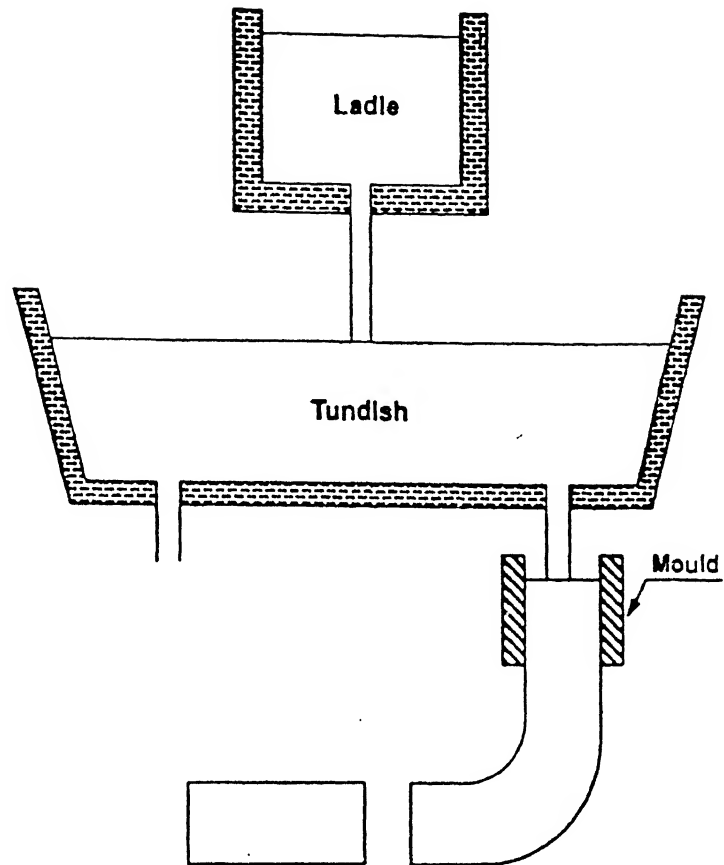


*Fig.(4.1)* : Schematic representation of the continuous casting process.

suited for inclusion separation. Therefore, tundish design is important for the tundish to perform the desired functions effectively. Towards this, mathematical modelling can give a quantitative assessment of flow and turbulence parameters and the associated *RTD* distribution and thus provide useful insight into the overall process. This in turn can help achieving an optimal tundish design.

## 4.2 Characteristics of Metallurgical Tundish System

When fluid flows through the tundish it is important to establish the time spent in the system by individual fluid elements. The *average time* or the *nominal holding time*, of the fluid in the system is easily calculated from the definition

$$t_r = \frac{\text{Volume of fluid in vessel}}{\text{Volumetric rate of fluid flow}} \quad (4.1)$$

However, some fluid individual elements may spend a longer, and others a shorter period of time in the system. The minimum amount of time a fluid spends inside the vessel is called the *breakthrough time*. This departure of actual residence times from the mean i.e., the distribution of residence times is an important characteristic of the tundish system and influences the latter's performance as a reactor. The residence time distribution of a fluid flowing through the tundish can be determined by means of tracer studies. This involves the addition of the tracer to the stream entering the vessel, and then measurement of its concentration at the exit with respect to time.

Several methods have been developed for introducing the tracer material into the vessel, but the two most important [25,36] are :

- i. continuous addition of tracer to the input stream, starting at a particular time (step input), and
- ii. addition of the tracer over a short time interval, the duration of which is negligible in

comparison with the mean residence time of fluid in the vessel (pulse input).

Of the above two methods, pulse input of tracer is more popular as in many tests the use of step input of tracer may lead to extensive contamination of product or alter the fluid flow behaviour itself. It has also been shown [36] that the information derived from pulse addition of tracer is ideal for discriminating the hydrodynamics of different tundish systems.

The results obtained from pulse addition of tracer are plotted in the form of dimensionless concentration vs. dimensionless time and are called *C*-curves.

$$C = \frac{c}{Q/\bar{V}} \quad (4.2)$$

where,

$Q$  = quantity of the tracer injected,

$V$  = volume of the fluid in the vessel.

The denominator of *Eq.*(4.2) represents the average concentration that the tracer would reach if it were perfectly mixed within the vessel. The area under the *C*-curve is unity as all tracer entering the system should eventually leave it (  $\int C d\theta = 1$  ). From the *C*-curve parameters like the minimum breakthrough time (  $t_{min}$  ), the time at which the peak concentration is reached (  $t_{peak}$  ), and the average residence time (  $t_{avg}$  ) can be obtained . These can be converted into their equivalent dimensionless forms (  $\theta_{min} = t_{min} / t_r$  ,  $\theta_{peak} = t_{peak} / t_r$  ,  $\theta_{avg} = t_{avg} / t_r$  ) where  $t_r$  is the theoretical residence time as defined by *Eq.*(4.1). To interpret the results from the *C*-curve quantitatively the vessel volume can be assumed to be made up of three parts namely, a well mixed volume ( $V_m$ ), a dispersed plug volume ( $V_{dp}$ ) and a dead volume ( $V_d$ ) [36]. The fractional volumes can be calculated as [36] :

$$V_d = (1 - \theta_{avg}) \quad (4.3)$$

$$V_{dp} = \frac{(\theta_{min} + \theta_{peak})}{2} \quad (4.4)$$

$$V_m = 1 - V_d - V_{dp} \quad (4.5)$$

The relative amounts of these volumes determine the efficiency of a given tundish and can also be used as appropriate criteria for improving the tundish design or for comparative analysis. The preceding formulation assumes that only negligible volume of liquid spends a time greater than twice the theoretical residence time in the tundish.

#### 4.3 Mathematical Modelling of Tundish Hydrodynamics

As mentioned already, a metallurgical tundish may be regarded as a trough into which molten metal is being poured from a teeming ladle at one location and discharged from the tundish through one or more outlets. The flow is known to be highly turbulent in the vicinity of the pouring stream while elsewhere in the tundish, flow is in the transitional regime [36]. Further, the nature of the fluid flow is essentially three dimensional and elliptic. Except for the initial transient and the final drain out stages, the flow induced in a tundish ( when bath height, exit velocity etc. remain constant ) can be described mathematically by the steady state, three dimensional calculation procedure outlined in *Chapter-3*. Once flow variables and turbulence parameters are predicted, these can be coupled with an appropriate convection-diffusion equation to predict the RTD (residence time distribution) pattern in the tundish. (see later)

In the present study, fluid flow behaviour in a model tundish used by Singh and Koria [17] with single inlet and outlet and no flow control devices has been analysed. The characteristic design features of the model tundish [17] have been summarised in *Table-4.1*. To mathematically model the tundish the sloping side walls were neglected and the tundish as a first approximation was assumed to be perfectly rectangular. The schematic of the tundish



modelled [17] in the present study has been shown in Fig.(4.2).

Table-4.1: Characteristic parameters of the single strand model tundish [17].

Parameter	Model Tundish
Fluid	Water, ( $\mu=0.001 \text{ kg m}^{-1}\text{s}^{-1}$ , $\rho=1000 \text{ kg/m}^3$ )
Base length, $m$	1.0
Width (at base), $m$	0.30
Height, $m$	0.37
Liquid depth, $m$	0.26
Shape	rectangular with sloping walls ( $15^\circ$ )
No. of strands	one
Ladle shroud diameter, $m$	0.021
Volumetric flow rate, $m^3/s$	$1.55 \times 10^{-4}$
Inlet Reynolds number	$9.0 \times 10^3$

#### 4.3.1 Modelling assumptions

The following assumptions and idealisations were made in the present work to investigate the fluid flow behaviour in tundish.

- The flow is assumed to be turbulent and macroscopically steady i.e., the effect of transience during filling and emptying of tundish was neglected.
- The melt surface is assumed to be flat and phenomena like wave formation, presence of slag layer at the free surface and vortexing during drainage etc. are neglected.
- Entrainment of air or gas through the metal inlet is neglected (the ladle stream is essentially shrouded).

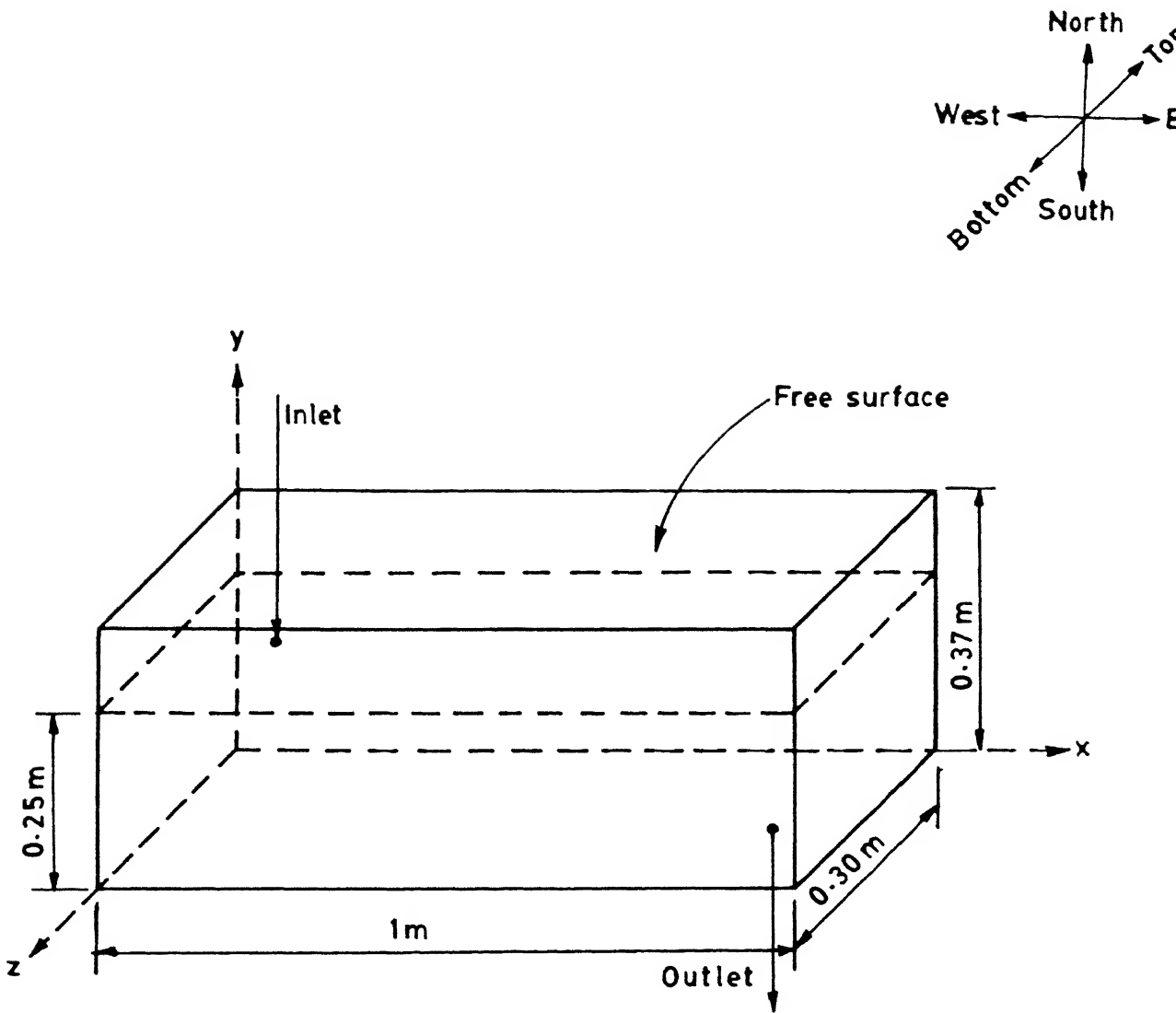


Fig.(4.2) : Schematic of the single strand model tundish [17] simulated in the present study.

- iv. The flow is essentially Newtonian and incompressible and
- v. The system is isothermal and thus the effect of temperature differential on the melt flow is neglected.

#### 4.3.2 Governing equations and boundary conditions

As already mentioned, the nature of fluid flow in tundishes is three dimensional and can be represented by the continuity equation and the three components of the Navier-Stokes equations already outlined in *Chapter-3* (Refer *Eqs.(3.1) to (3.4)*). The effective viscosity appearing in these equations can be obtained from the  $k-\epsilon$  model of turbulence (Refer *Eqs.(3.5) to (3.8)*). The applicable set of boundary conditions to the tundish system are :

- i. At the free surface ( in the north direction ) zero shear is assumed to be transmitted for the velocity components. Zero gradient of  $k$  and  $\epsilon$  were specified at the free surface. In conjunction with these, vertical component of flow is set to zero. Mathematically,

$$\text{At } y = 0.26 \text{ m}, 0 \leq x \leq 1.0 \text{ m and } 0 \leq z \leq 0.30 \text{ m},$$

$$v = 0, \partial u / \partial y = \partial w / \partial y = 0, \partial k / \partial y = \partial \epsilon / \partial y = 0$$

- ii. No slip condition for the velocity components was specified at the boundary walls. (see *Fig. (4.2)*) The values of  $k$  and  $\epsilon$  were set at zero at the wall.

$$\text{At } y = 0, 0 \leq x \leq 1.0 \text{ m and } 0 \leq z \leq 0.30 \text{ m},$$

$$u = v = w = 0, k = \epsilon = 0.$$

$$\text{At } x = 0 \text{ and } x = 1 \text{ m}, 0 \leq y \leq 0.26 \text{ m and } 0 \leq z \leq 0.30 \text{ m},$$

$$u = v = w = 0, k = \epsilon = 0.$$

$$\text{At } z = 0 \text{ and } z = 0.3 \text{ m}, 0 \leq y \leq 0.26 \text{ m and } 0 \leq x \leq 1.0 \text{ m},$$

$$u = v = w = 0, k = \epsilon = 0.$$

In addition to this, at the exit, outflow boundary condition was specified by considering relevant Peclet number to be infinity (e.g., zero diffusion). Regions close to the wall have been modelled using the standard wall function procedure [21,32] (for details see *Chapter-3*) In addition to these, at the inlet the normal velocity was specified from the total volume flow rate ( $v=0.41 \text{ m/s}$ ). The inlet values of  $k$  and  $\epsilon$  were estimated from the following relations [37].

$$k_i = 0.01u_i^2 \quad (4.6)$$

$$\epsilon = \frac{k_i^{1.5}}{(d_i)/2} \quad (4.7)$$

where  $u_i$  is the normal inlet velocity and  $d_i$  is the diameter of the inlet nozzle. At the outlet nozzle, the normal velocity was calculated from the overall mass balance [38].

Computations were performed using uniform grid covering the whole tundish. The grid set of  $52 \times 12 \times 7$  were chosen for the  $x$  (longitudinal),  $y$  (vertical) and the  $z$  (transverse) directions respectively. Under-relaxation factors of 0.5 for velocities and 0.7 for scalar quantities were adopted ( see *Chapter - 3* for details on the under-relaxation procedure employed ). A typical execution time required about 150 *min* of *CPU* time on a *HP-9000* machine.

### 4.3.3 Governing equation of tracer dispersion

As pointed out previously, the residence time distribution (*RTD*) characteristic of a tundish can be studied effectively by tracer dispersion studies. Thus, following a pulse addition the appropriate conservation equation of the added tracer can be described in terms of the following convection - diffusion equation in cartesian co-ordinate system:

$$\frac{\partial}{\partial t}(C_i) + \frac{\partial}{\partial x}(uC_i) + \frac{\partial}{\partial y}(vC_i) + \frac{\partial}{\partial z}(wC_i) = \frac{\partial}{\partial x}(D_i \frac{\partial C_i}{\partial x}) + \frac{\partial}{\partial y}(D_i \frac{\partial C_i}{\partial y}) + \frac{\partial}{\partial z}(D_i \frac{\partial C_i}{\partial z}) \quad (4.8)$$

diffusivity and  $D_T$  is the eddy diffusivity. The latter, can be directly equated to the turbulence kinematic viscosity assuming turbulent Schmidt number to be approximately unity i.e.  $\mu_T / (\rho D_T) = 1$  (valid for a wide range of engineering problems). A zero flux boundary condition is imposed on all the solid surfaces and the free surface. At the exit, for the control volume passing through it, a sink term was incorporated into Eq.(4.8) as:

$$\frac{\partial C_i}{\partial t} + \text{div}(u C_i) = \text{div}(D_e \text{grad } C_i) - K C_i \quad (4.9)$$

where  $K = (\text{cross-sectional area of the outlet face of control volume}) \times (\text{the normal velocity through the outlet face})$ . The negative source (e.g., sink) term,  $-K C_i$  was dumped in  $A_p$  (i.e.,  $A_p = \sum A_{nb} - S_p$ ) for numerical stability. In addition to this, an initial condition, i.e.,

$$\text{at } t = 0, C_i = C_i^o \text{ at } I = 8, J = 10, K = 4$$

was applied to Eq.(4.8). The specified  $I, J$  and  $K$  coordinates are respectively the location of the tracer input, where,  $C_i^o = 1000 \text{ kg} / \text{m}^3$  (tracer having the same density as the bulk liquid) was used in the numerical solution scheme. It is instructive to note here that one way coupling between Eq.(4.8) and the flow and turbulence model equations allows flow computation to precede the calculation of the tracer dispersion. Once converged flow field is obtained, this was applied to predict the  $C_i(x, y, z, t)$  field. A convergence criteria of  $10^{-6}$  was applied on Eqs.(4.8) and (4.9). In addition for every time step a minimum number of iterations ( $= 7$ ) was carried out. From the predicted concentration at the outlet as a function of time,  $t$ , the  $C$ -curve can be conveniently constructed as explained in Section-4.2.

## 4.4 Results and Discussion

### 4.4.1 Fluid flow behaviour

The predicted velocity field in the rectangular shaped tundish has been shown as a series of 2D plots (e.g., vertical  $XY$  planes and horizontal  $XZ$  planes) in Figs(4.3) and (4.4).

As seen from these figures, the general nature of the flow is of three dimensional nature with pronounced spatial variations.

*Figure (4.3.a)* represents the flow on the central vertical  $XY$  plane passing through the inlet and the outlet. There as seen, the incoming jet of water flows downward, entrains liquid from the surrounding and thus decelerates considerably as it proceeds towards the base of the vessel. The flow in and around the inlet region is highly turbulent (predicted  $\mu_e$  is of the order of  $0.12 \text{ kg/m.s}$ ). The fluid after hitting the base, moves outwards towards the vessel side walls. Closer to the left wall, this outwardly flowing fluid rises to the free surface and finally, turns inward towards the jet entry region. This inturn forms a small but distinct recirculating loop (see the left portion of *Fig.(4.3.a)*). To the right of the inlet stream, the fluid in the upper region of the vessel is seen to be converging towards the jet entry, while in the vicinity of the tundish base, the flow is away from the jet impinging region. It is also clear from *Fig.(4.3.a)* that the velocities drop significantly with increasing distance from the inlet region. Fluid velocities again become appreciable near the outlet.

The fluid after hitting the vertical walls (those along the  $z$  direction) also moves upwards towards the free surface as seen from *Fig.(4.3.b)*. There the velocity field has been plotted on a vertical  $XY$  plane in the immediate vicinity of the wall. As seen, close to the inlet region, the flow is directed vertically upward (a consequence of the continuity requirement) while in the vicinity of the exit, the flow is directed vertically downwards. As one might anticipate, the inlet and the outlet in the tundish strongly affect the flow pattern in their immediate vicinity.

Similarly, when results are plotted on horizontal planes (see *Fig.(4.4.)*), it is readily seen that the inlet jet after hitting the base of the tundish spreads in all directions, but predominantly towards the front and rear walls (walls along the  $z$  direction). Furthermore, the jet spreads very little towards the exit nozzle (*Fig.(4.4.a)*), as it is much more easier for the liquid to move towards the side walls (e.g., the momentum of the liquid is much higher in this direction). In the central region of the tundish the flow is noticeably weak. Finally, in the proximity of the exit nozzle the flow becomes strong again because of the drainout action. In

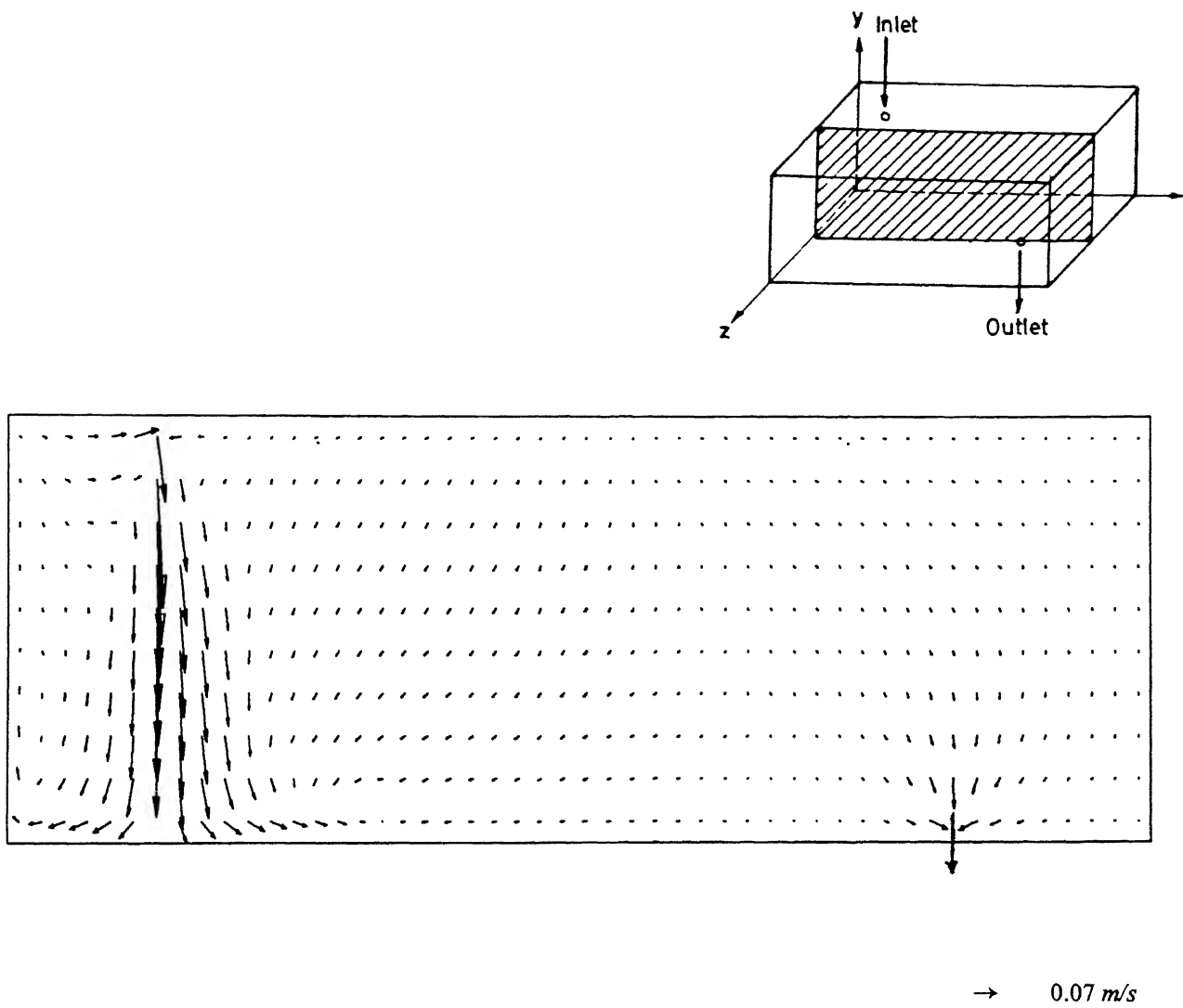


Fig.(4.3.a) : The predicted flow pattern in the central vertical  $XY$  plane (at  $z = 0.15$  m).

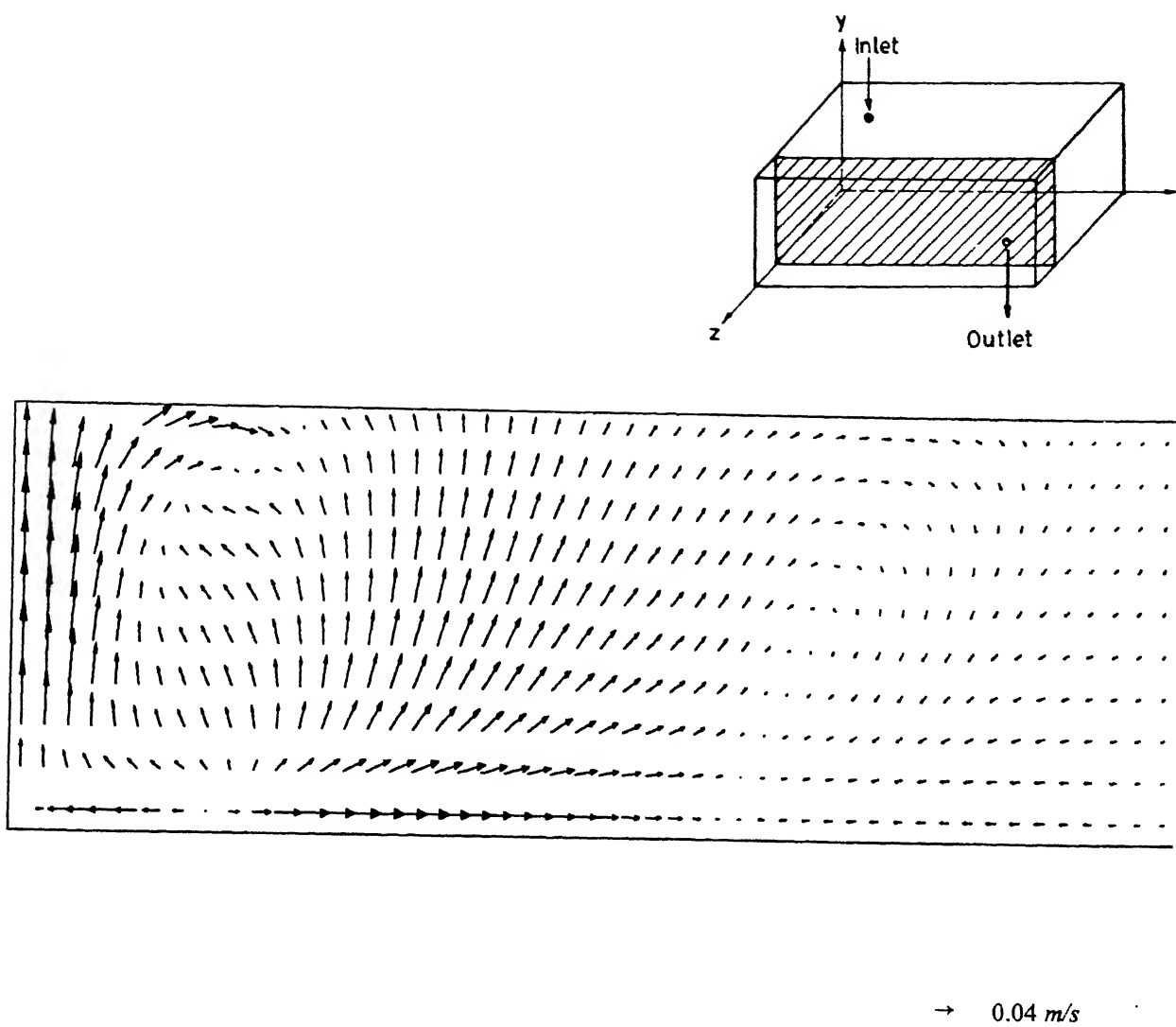
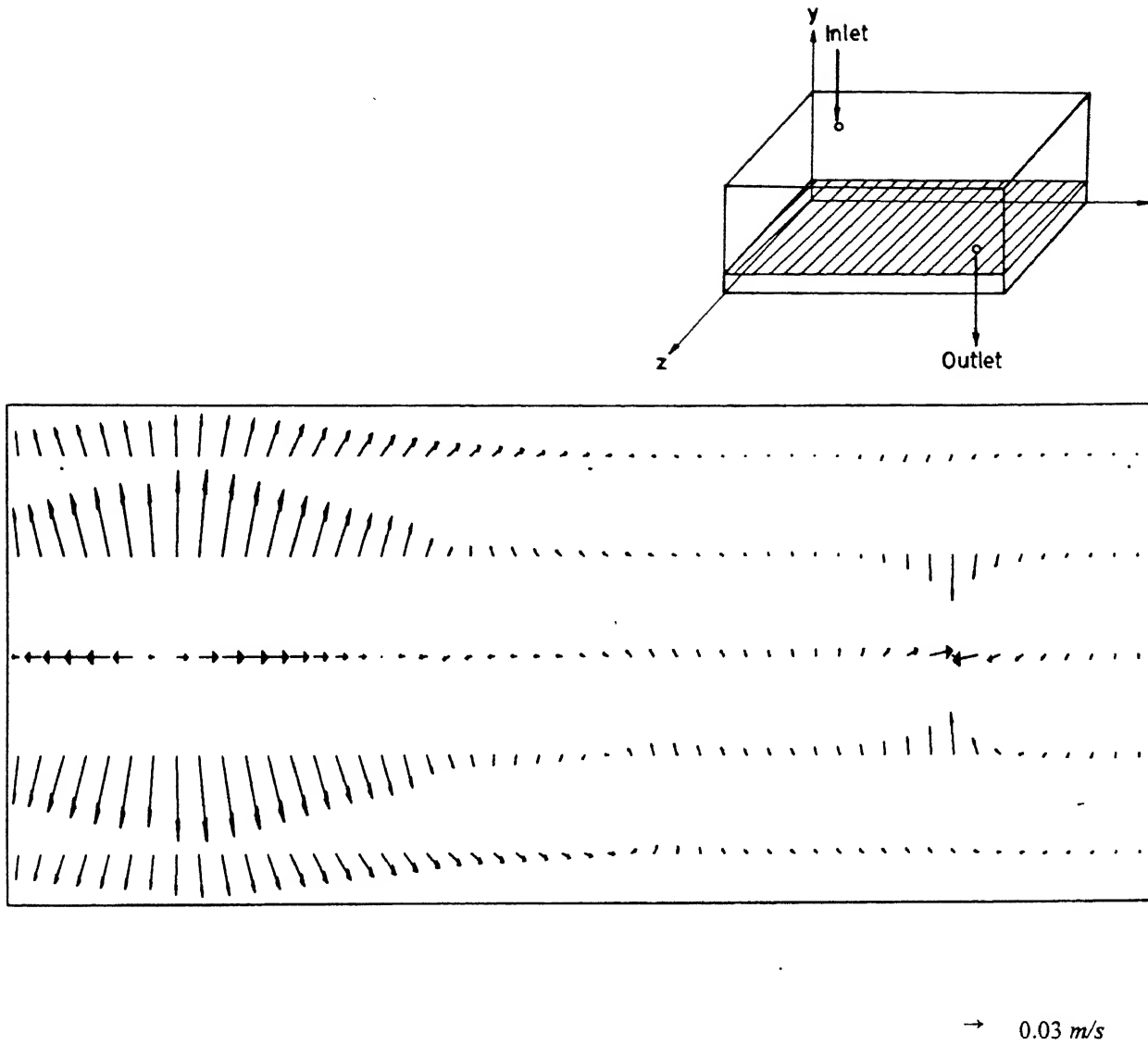


Fig.(4.3.b) : The predicted flow pattern in a vertical  $XY$  plane close to the wall ( at  $z = 0.03 \text{ m}$  ) .





*Fig.(4.4.a)* : The predicted flow pattern in a horizontal  $XZ$  plane close to the base of the tundish (at  $y = 0.012 \text{ m}$ ).

addition to these, weak recirculation of the liquid is seen to the right of the exit point (e.g., between the exit nozzle and the wall to its right).

In *Fig.(4.4.b)*, fluid flow pattern has been plotted on the horizontal  $XZ$  plane passing through the middle of the tundish ( at  $y=0.11$  m). There the liquid can be seen to be converging very strongly towards the entry nozzle particularly from the front and the rear of the inlet. The flow vectors in the central region of the plane are directed towards the inlet region whereas, fluid flow closer to the walls is directed towards the outlet . A weak recirculating loop is also seen to be forming about the outlet. Finally, in *Fig.(4.4.c)*, fluid flow pattern is shown on the horizontal  $XZ$  plane (at  $y = 0.24$  m) close to the free surface of the liquid. There also the liquid is seen converging towards the entry jet region from left part of the vessel. Immediately, above the outlet region, the flow is practically absent in this plane (free surface is farthest from the exit).

From the preceding discussion, the following general observations can be made about the nature of the fluid flow in rectangular shaped tundishes with single entry and exit nozzles and no flow control devices. The entering jet spreads outwardly following impingement and this as a consequence, entrains the surrounding liquid. Subsequently, the liquid flows towards the walls of the tundish and then, towards the free surface and finally converges to the entering jet of water. This characteristic of flow is identical for all directions in the vicinity of the inlet nozzle only. The flow pattern however, gets considerably modified in the vicinity of the exit, where the flow direction is seen to be governed predominantly by the drainout action. These features of flow in metallurgical tundish systems which is the result of the combined action of an impinging jet and a outgoing stream are now rather well established. Present flow predictions are qualitatively in line with similar computational studies reported earlier for the tundish system. To substantiate this, computational results of Sahai from ref.39 is shown in *Fig.(4.5)*.

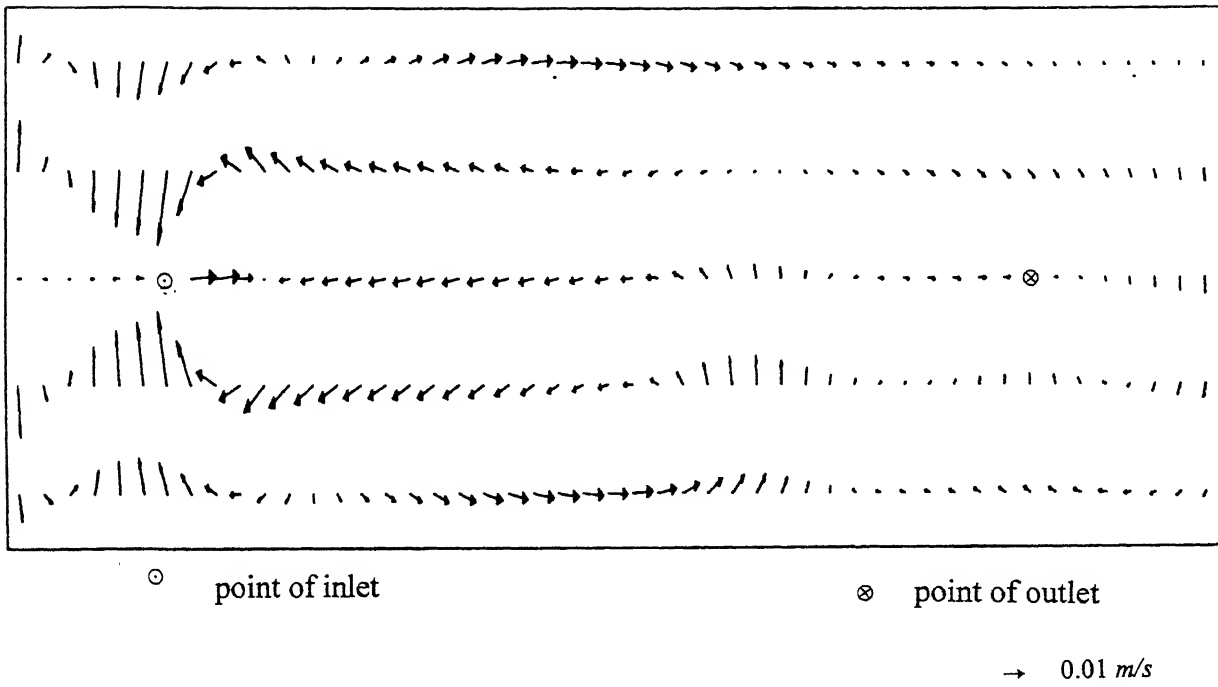
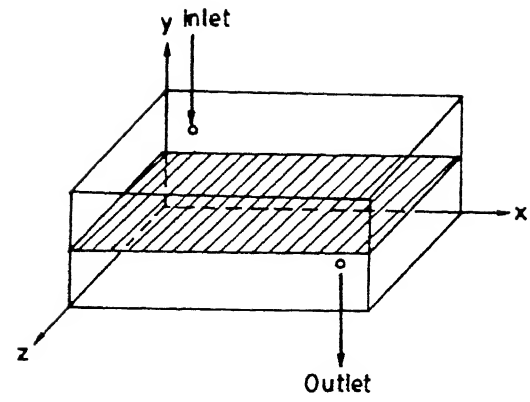
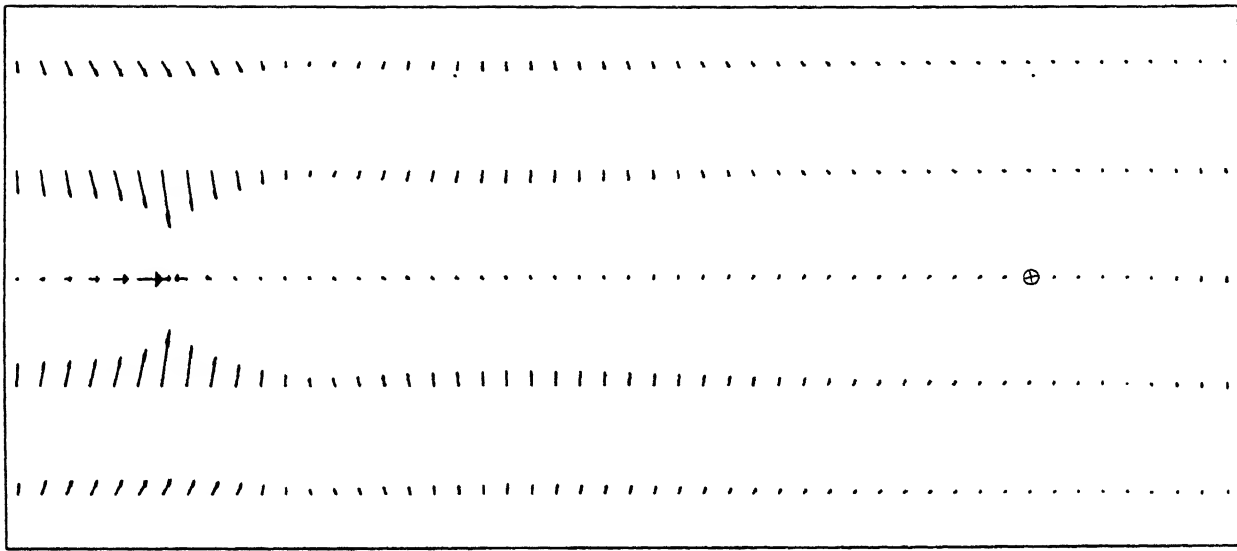
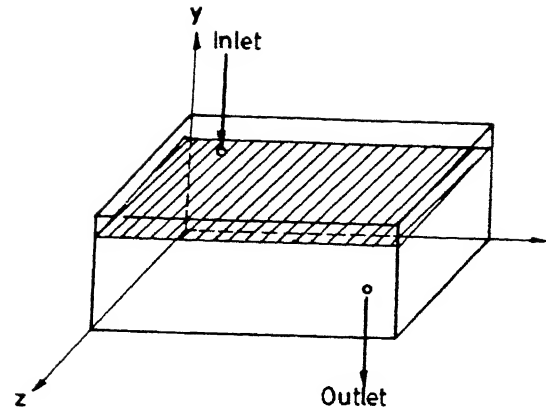


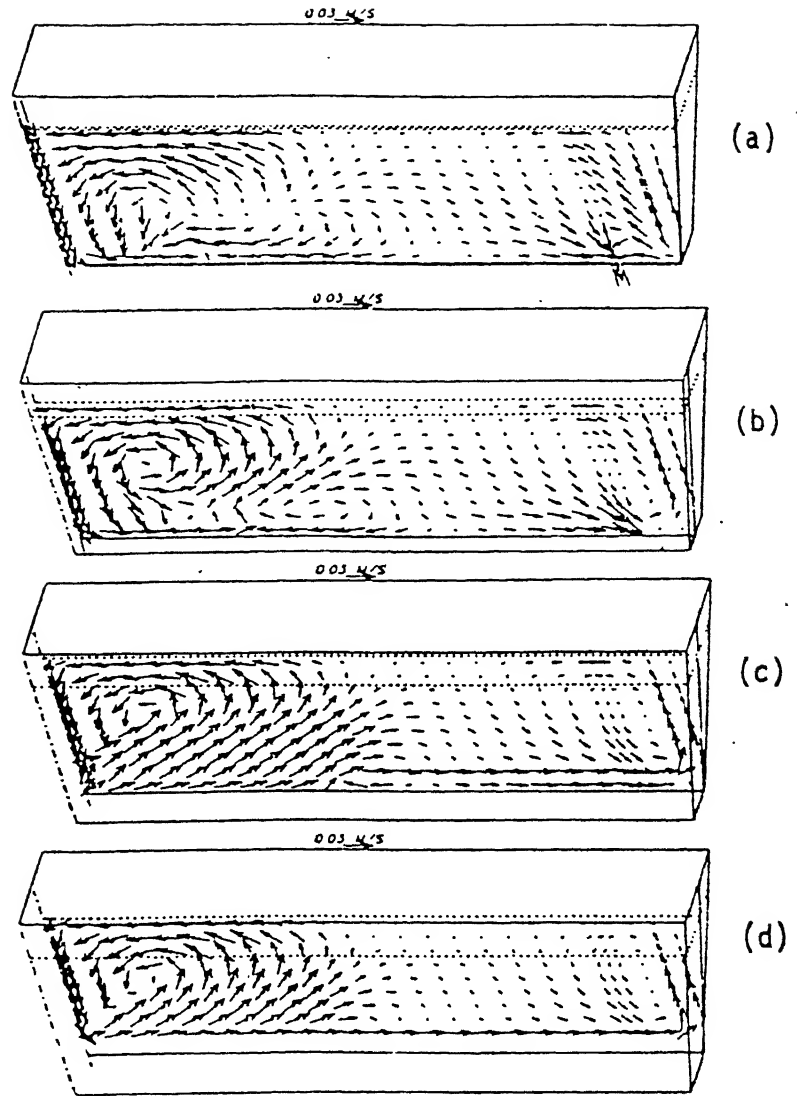
Fig.(4.4.b) : The predicted flow pattern in a horizontal  $XZ$  plane (at  $y = 0.11$  m).



⊗ point of outlet

→ 0.02 m/s

Fig.(4.4.c) : The predicted flow pattern in a horizontal  $xz$  plane close to the free surface. (at  $y = 0.24 \text{ m}$ ).



(a) near the plane of symmetry and (d) closer to the inclined wall.

Fig.(4.5) : Predicted flow field in longitudinal, vertical planes with no flow control devices in a tundish with inclined wall [39].

#### 4.4.2 Residence time distribution characteristics

As pointed out already, the residence time distribution of the fluid in the model tundish was investigated by pulse addition of a tracer at the fluid inlet location i.e. at  $t = 0$ , the inlet control volume was made full of tracer of the same density as that of bulk liquid phase (e.g., water). The concentration of the tracer was then computationally monitored as a function of time at the control volume passing through the exit nozzle and one control volume vertically above it. The concentration of tracer at these locations was subsequently non-dimensionalised by dividing it by the average concentration that the tracer would assume in the vessel, if it were perfectly mixed in the absence of any drainout ( $C_o = (m_{tracer}/V_{water}) = 0.4 \text{ kg/m}^3$ ). Similarly, the time was non-dimensionalised using the nominal holding time (see Eq.(4.1)) of the fluid in the vessel ( $t_r$ ). The result thus obtained ( $C/C_o$  vs.  $t/t_r$ ) was then plotted to get the C-curves. In Fig.(4.6), the C-curves obtained computationally for the two control volumes (1 mm and 3 mm above the exit nozzle) are shown. There as seen, the tracer is initially of negligible concentration at the exit stream, but it quickly increases to a maximum, before showing a gradual fade out. This characteristic of the RTD curve is similar to those obtained earlier by various investigators for the tundish systems [17,36,39]. The breakthrough time was calculated as the time when the concentration in the vicinity of the exit reached 0.1 % of the average concentration of the tracer (i.e.,  $C = 4 \times 10^{-4} \text{ kg/m}^3$ ).

Numerically predicted *breakthrough time* and the *time at which peak concentration* is achieved at the outlet together with those obtained by Singh and Koria [17] have been summarised in Table-4.2. As seen there, considerable differences appear between observed and predicted peak concentration time.

The possible reasons for the discrepancy between the observed and predicted peak concentration time can be attributed to:

- i. sensitivity of the results to the step height  $\Delta t$  and the numerical grid chosen.
- ii. inadequacy of the  $k-\epsilon$  model of turbulence to accurately simulate such systems and

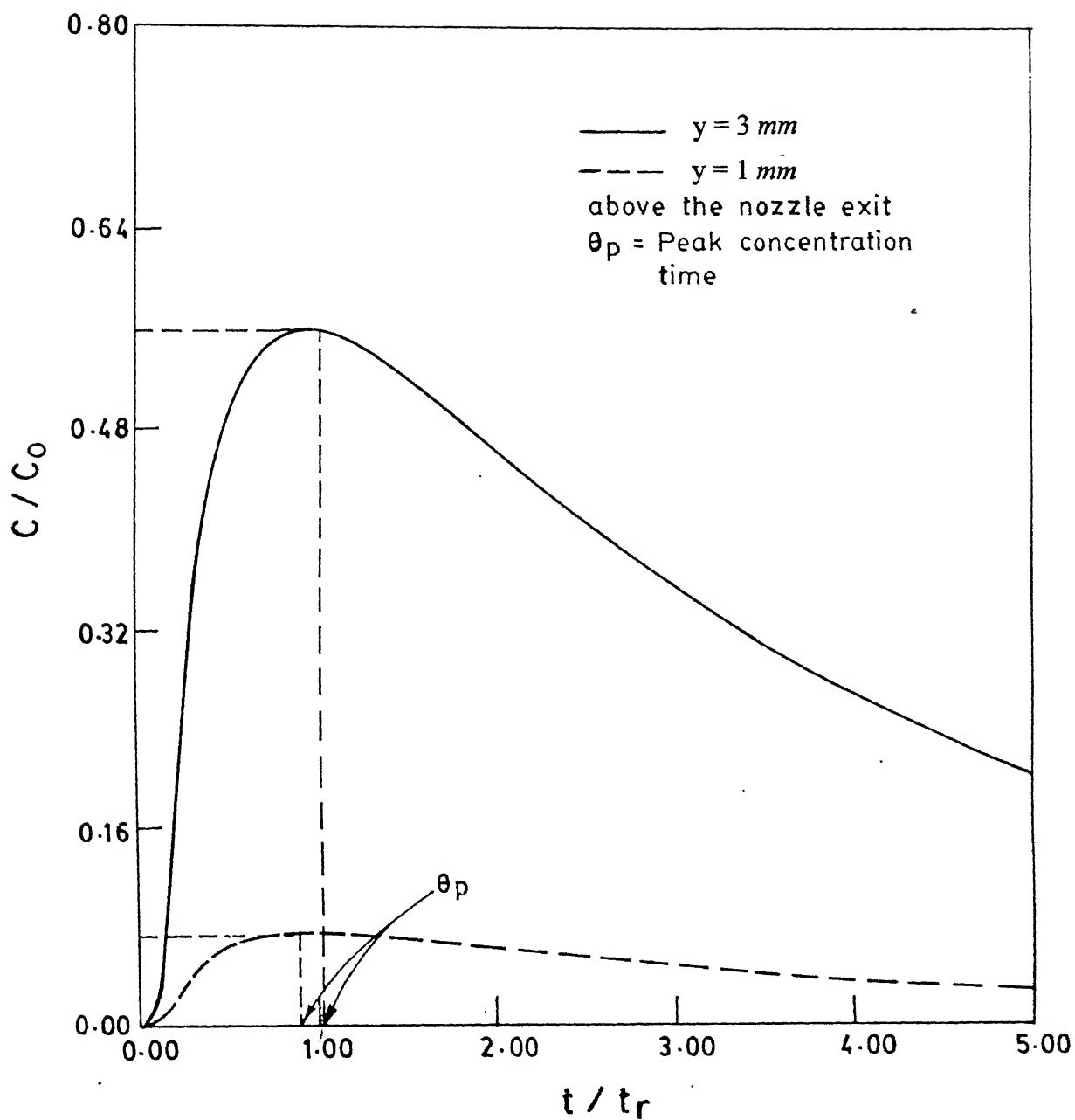


Fig.(4.6) : Predicted RTD curves for monitoring location at 1 mm and 3 mm above the nozzle exit.

finally,

- iii. the assumption of a perfectly rectangular shaped tundish (e.g., ignoring the wall taper).

**Table-4.2.:** Comparative results of *RTD* characteristics obtained via physical modelling [17] and mathematical modelling.

<i>RTD</i> Characteristics	Mathematical Modelling		Physical Modelling [17]
	1mm@	3mm@	
<i>Breakthrough time</i>	25	20	30 s
<i>Peak concentration time</i>	445	465	260 s

@ vertical distance of monitoring location above the exit nozzle.

The time dependent tracer dispersion equation ( *Eq.(4.8)*) has been solved by the fully implicit marching integration procedure [26], which is known to be relatively more accurate for larger time steps. Hence, the numerical calculations were carried out considering two time steps (5 and 10 s) to ascertain the influence of step height on the predicted results. As seen in *Fig.(4.7.a)*, increasing the time step two fold, from 5 to 10 s, does not bring in any change in the solution. Consequently, results shown in *Table-4.2* can be assumed to be independent of  $\Delta t$  chosen. Similarly, two different grid systems 25 x 8 x 7 and 52 x 12 x 7 were used. Only marginal changes in predicted flows and concentration fields were observed.

The fluid flow in a steelmaking tundish is known to be turbulent only in the inlet region [36]. Further, the intensity of flow variables and turbulence parameters in tundishes are essentially determined by the kinetic energy of the incoming jet and the vessel geometry. The flow is in the transitional regime at locations away from the inlet stream. To assess the role of a turbulence model in the calculation procedure, the bulk effective viscosity model proposed by Pun and Spalding [40] was applied in the numerical calculation procedure in leu of the  $k-\epsilon$  model of turbulence. Pun and Spalding proposed the following empirical correlation, through dimensional reasoning for computing turbulent flows in sudden expansion geometry.



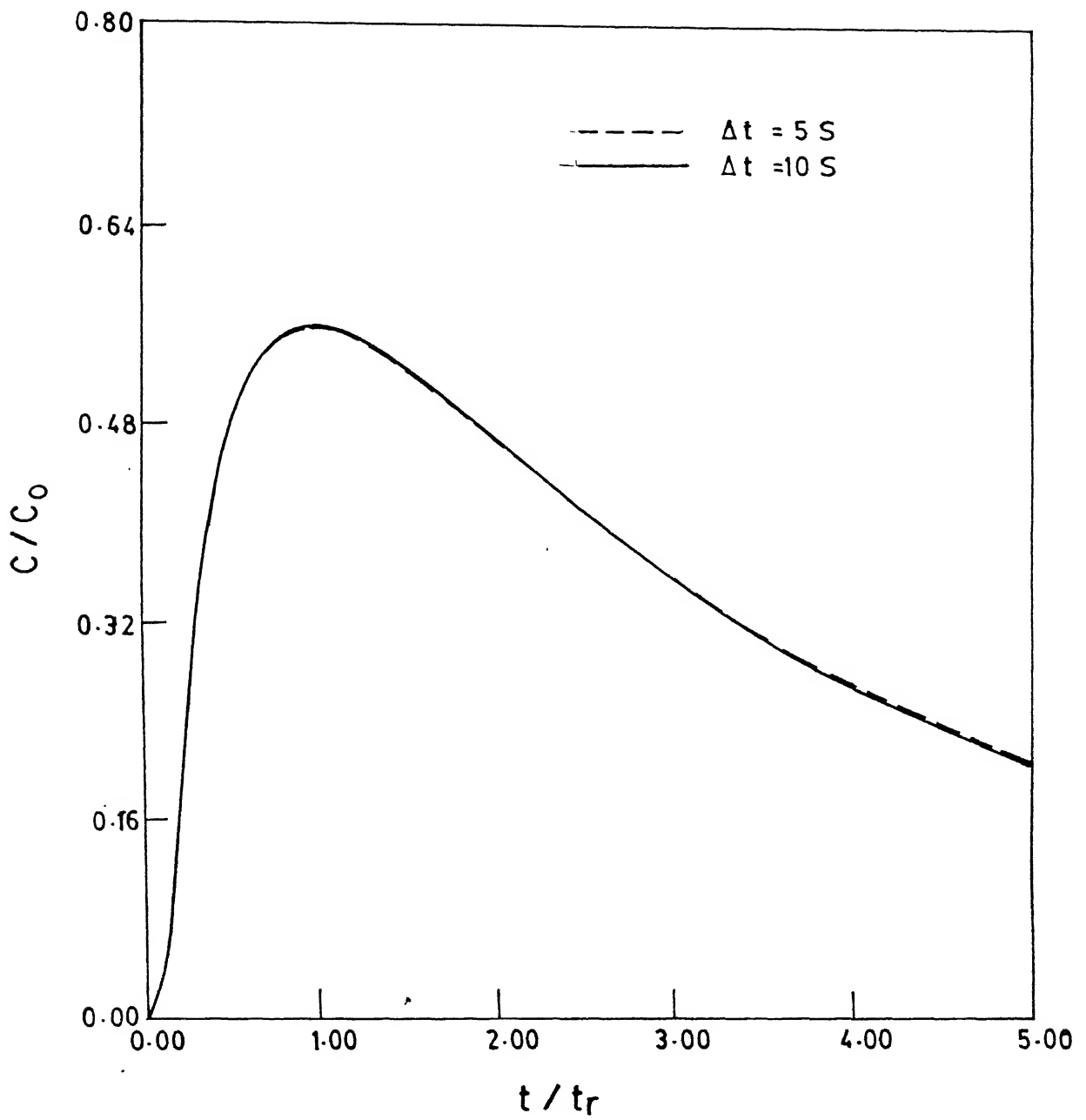


Fig.(4.7.a) : Sensitivity of the *RTD* curves to the step height,  $\Delta t$  assumed in the numerical procedure.

$$\mu_e = K D^{0.67} H^{-0.33} \rho^{0.67} (\mu u)^{0.33} \quad (4.10)$$

In Eq.(4.8),  $\mu_e$ , the dependent variable is related to the medium density  $\rho$ , the reactor length  $H$ , the reactor diameter  $D$  and the kinetic energy rate of incoming fluid,  $(\mu u^2)$ .  $K$  is an empirically fitted constant and assumes a value 0.012 for sudden expansion geometry. The  $\mu_e$  calculated via the above correlation ( assuming,  $D$  = width along the  $z$  direction and  $H$  = depth of the liquid) for the present study was found to be approximately  $0.04 \text{ kg m}^{-1}\text{s}^{-1}$ . In contrast, the  $k$ - $\epsilon$  model of turbulence predicted  $\mu_e$  in the range of 0.05 to  $0.2 \text{ kg m}^{-1}\text{s}^{-1}$ . Thus, calculations were repeated using the bulk effective viscosity model [40] whereby,  $\mu_e$  was arbitrarily specified in the range of 0.05 to  $0.1 \text{ kg m}^{-1}\text{s}^{-1}$  within the tundish. The affect of effective viscosity on the residence time distribution is shown in Fig.(4.7.b). There as seen numerical value of  $\mu_e$  shifts the *RTD* curve and consequently, the residence time of fluid in the tundish appreciably. However, *RTD* characteristics like *breakthrough time* and *peak concentration time* remain virtually unaffected. Hence, the choice of the turbulence model does not appreciably affect the predictions regarding *breakthrough time* and *the peak concentration time*. Evidently, the total residence time which is a measure of the area under the curve does change significantly with different choice of turbulence model.

Finally, as mentioned already the wall taper of  $15^\circ$  has been neglected in the present numerical simulation. This has lead to an underestimation of the tundish volume by over 18 %. Hence, the breakthrough time predicted in the present study is lower from that predicted by the physical modelling route [17]. Similarly, the poor agreement between the predicted and observed peak concentration time appears to be related to the fact that tapering of sidewalls alters the flow significantly, and makes it predominantly directed along the base of the tundish [17,39] which has not been computationally observed in the present study. Quantitative comparison thus is meaningful only when the exact vessel geometry is incorporated into the numerical solution scheme. This is however left for a future work.

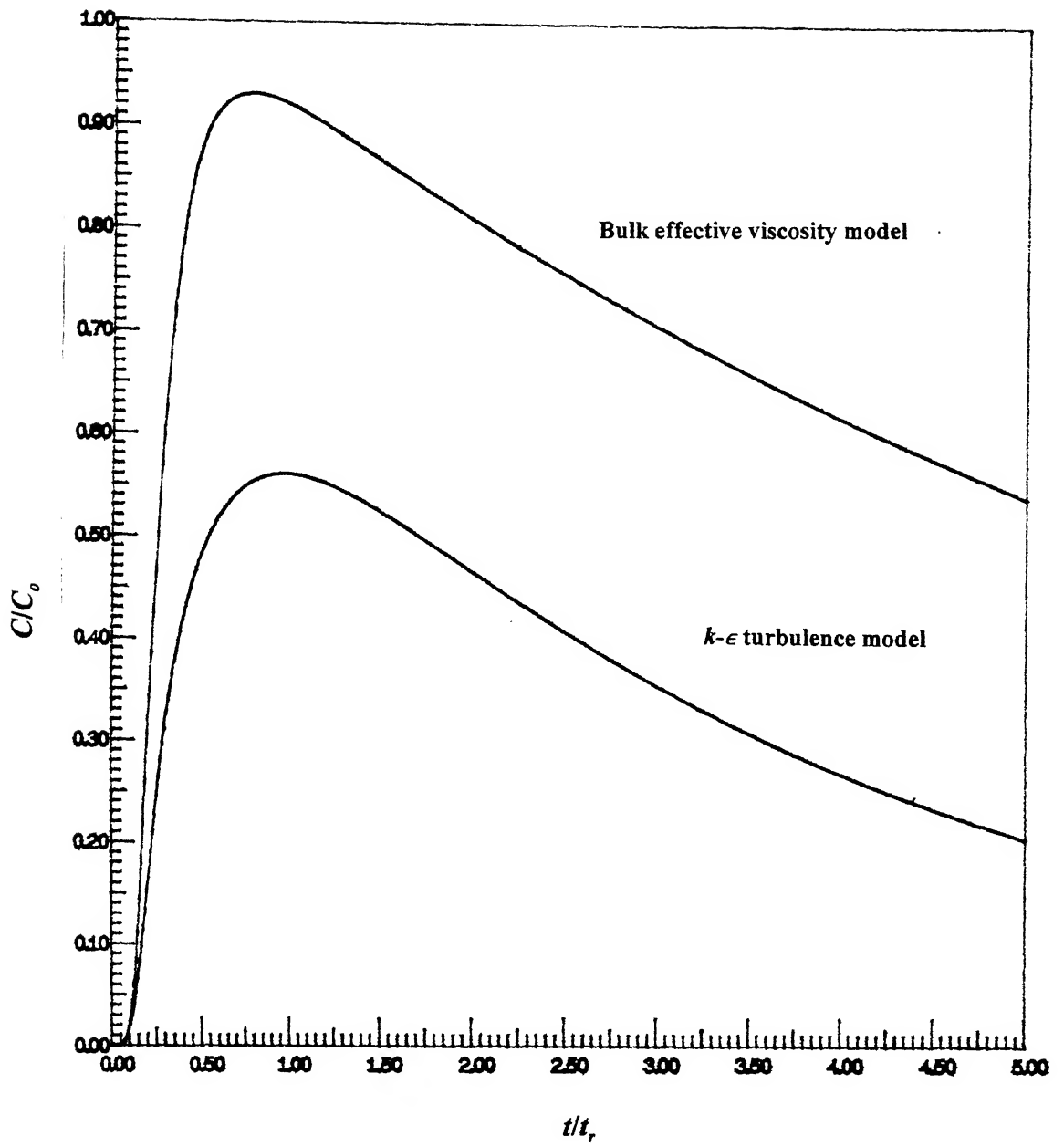


Fig.(4.7.b) : The affect of numerical value of effective viscosity on the prediction of RTD characteristics in the tundish system.

## CHAPTER - 5

### CONCLUDING REMARKS

The following three major conclusions can be derived from the present study:

- i. A hydrodynamic model has been developed, by using a two phase, two dimensional turbulent flow model in conjunction with an appropriate heat transfer correlation to estimate the melting rates of solids in gas stirred metallurgical reactors. It was demonstrated that the mathematical model simulates experimental observations realistically. The predictive capabilities of the model were also evaluated with references to various process and numerical parameters. It has been shown explicitly that for accurate prediction of rate processes in such two phase systems, realistic inputs of bubble diameter, drag coefficient values etc. are required.
- ii. In the absence of computational facility, a simple, yet effective macroscopic equation has been suggested for estimating melting rates of solids in the plume region of gas stirred baths. It has been demonstrated that the macroscopic model produces estimates that are comparable to the detailed differential model results.
- iii. Finally, the two dimensional, two phase calculation procedure was modified and a steady state, two phase, three dimensional, turbulent flow model has been developed, based on the control volume formulation, embodying the *SIMPLE* algorithm. The three dimensional calculation procedure developed has been tested against standard test solutions and qualitative agreement shown. The model was shown to simulate qualitatively melt flow behaviour and residence time distribution in rectangular shaped tundish systems.

## CHAPTER - 6

### RECOMMENDATIONS FOR FUTURE WORK

The scope of the present work can be further expanded considering the following:

- i. In the present study, fluid flow has been evaluated in rectangular shaped tundishes with no flow control devices. The three dimensional turbulent flow model can be conveniently modified to study transport phenomena in tundishes with inclined walls and flow control devices (e.g., dams, weirs, slotted baffles etc.)
- ii. Argon and/or nitrogen injection which is increasingly being applied in tundish operations is a relatively new area that can be investigated with the aid of the present model. No comprehensive two phase simulation (either experimental or theoretical) of metallurgical tundish system has been reported in the literature to-date.
- iii. The two phase, three dimensional, turbulent flow model which has been developed in the present work can be suitably modified, to carry out equivalent computations in polar co-ordinate system. The code can then be used to simulate a variety of metallurgical processes such as, asymmetric gas injection in vessels, side blown converters, *R.H.*-degassers and so on.
- iv. The influence of temperature variations on fluid flow (free convection affects) has been neglected in the present study. Integration of heat transfer aspects to the present model will enable it to predict the affect of temperature losses or auxiliary heating on fluid flow. Similarly, appropriate form of Maxwell equations can be incorporated in the body force terms of the Navier-Stokes equation in the present model, to study the affect of magnetic field on fluid flow in metallurgical tundishes.

## REFERENCES

1. A.W.D. Hills : Heat and Mass Transfer in Process Metallurgy, The Institute of Mining and Metallurgy, London, 1967.
2. J.Szekely : Metall. Trans. B, Vol **19 B** (1988), p 525.
3. S.D.Lympany and J.W.Evans : Metall. Trans B, Vol **14 B** (1983), p 63.
4. R.J.Moreau and J.W.Evans : J. Electrochem. Soc., Vol **131**(10), (1984), p 2252.
5. W.E.Wahnsiedler: Proc. TMS-AIME Extractive Metallurgy Symp. on Mathematical Modelling of Materials Processing Operations, The Metallurgical Society, Warrendale, PA, 1987, p 643.
6. B.G.Thomas, L.J.Mika and E.M.Najjar : Metall. Trans B, Vol **21 B** (1990), p 387.
7. P.J.Flint, Q.L.He, R.B.Mahapatra and J.Herbertson : Proc. 10th PTD conf., Toronto, Canada, ISS-AIME, (1992), p 279.
8. Q.Jiao, L.Wu and N.J.Themelis : Proc. TMS-AIME Extractive Metallurgy Symp. on Mathematical Modelling of Materials Processing Operations, The Metallurgical Society, Warrendale, PA, 1987, p 835.
9. Y.B.Hahn and H.Y.Sohn : Proc. TMS-AIME Extractive Metallurgy Symp. on Mathematical Modelling of Materials Processing Operations, The Metallurgical Society, Warrendale, PA, 1987, p 799.
10. J.Szekely, J.H.Grevet, N.El-Kaddah: Int. J. Heat and mass transfer, **27** (1984), p 1116.
11. D.Mazumdar, N.Kumar and V.Verma: Ironmaking and Steelmaking, **19**, No.2, (1992), p152.
12. D.Mazumdar, P.Bansal and T.Narayan: Applied Mathematical Modelling, **16** (1992), p 255.
13. S.Whitaker: J.A.I., Ch.E., **18** (1972), p 361.
14. S.Taniguchi, M Ohmi, S Ishiura and S Yamaguchi : Trans. Iron Steel Inst. Jpn., **23**

(1983), p 565.

15. S Taniguchi, M Ohmi and S Ishiura : Trans. Iron Steel Inst. Jpn., **23** (1983), p 572.
16. D.Mazumdar, R.I.L.Guthrie and Y.Sahai: Appl. Math. Model., **17** (1993), p 255.
17. S.Singh and S.C.Koria : Ironmaking and Steelmaking, **20** No3(1993), p 221.
18. D.Mazumdar and R.I.L.Guthrie: ISIJ International, **34** (1994), p 384.
19. C Bhanu and D.Mazumdar: ISIJ International (in press).
20. M.Iguchi, H.Tomida, K.Nakajima and Z.Morita: ISIJ International, **33** (1993), 728.
21. B.E.Launder and D.B.Spalding: Comput. Methods Appl. Mechan. Eng., **3** (1974), 269.
22. R.Clift, J.R.Grace and M.E.Weber: Bubbles, drops and particles, Academic press, London (1978).
23. A.O.Hinze: Turbulence, McGraw-Hill Inc., NewYork (1975).
24. Y.Sheng and G.A.Irons: Metall. Trans., **23 B** (1992), 779.
25. J.Szekely: Fluid phenomena in Metal Processing, Academic Press, (1971).
26. S.V.Patankar: Numerical Heat Transfer and Fluid Flow, Hemisphere publishing corporation, NewYork, (1980).
27. M.A.S.C.Castello-Bronco and K.Schwerdfeger: Metall. Trans., **25 B** (1994), 359.
28. D.Mazumdar, R.I.L.Guthrie and Y.Sahai : Appl. Math. Model., **17** (1993), 255.
29. I.F.Masterson: 5th Int. Iron and steel congerss, Washington D.C., **6** (1986), 377.
30. T.Stapurewicz and N.J.Themelis : Unpublished research, Henry Crumb school of Mines, Columbia University, NewYork, 1986.
31. V.Sudhakar and D.Mazumdar : Metall. Trans., **27 B** (1996), 704.
32. W.Rodi : Turbulence Models and Their Application in Hydraulics - A State of the Art Review, University of Karlsruhe, Germany, (1980).
33. F.M.White : Fluid Mechanics, McGraw-Hill KogaKusha, Tokyo, (1979).
34. F.M.White : Viscous fluid flow, McGraw-Hill, NewYork, (1974).
35. V.Gupta and S.K.Gupta : Fluid Mechanics and its Application, Wiley Eastern Limited, New Delhi (1984).
36. J.Szekely and O.J.Ilegbusi : The physical and Mathematical Modelling of Tundish Operations, Springer-Verlag, NewYork (1988).
37. K.Y.K.Lai, M.Salcudean, S.Tanaka and R.I.L.Guthrie : Metall. Trans. B, Vol **17B**

(1986), p 449.

38. R.I.L.Guthrie : Engineering in Process Metallurgy, Clarendon Press, Oxford (1989).
39. Y.Sahai : Proc. TMS-AIME Extractive Metallurgy Symp. on Mathematical Modelling of Materials Processing Operations, The Metallurgical Society, Warrendale, PA, 1987, p 431.
40. W.M.Pun and D.B.Spalding : Proc. 17th Int. Astronautical Cong, **3** (1967), p 3.



